Ultrasound Tracking and Data Telemetry using CMUTs

MSc Thesis

Sai Sandeep Lolla

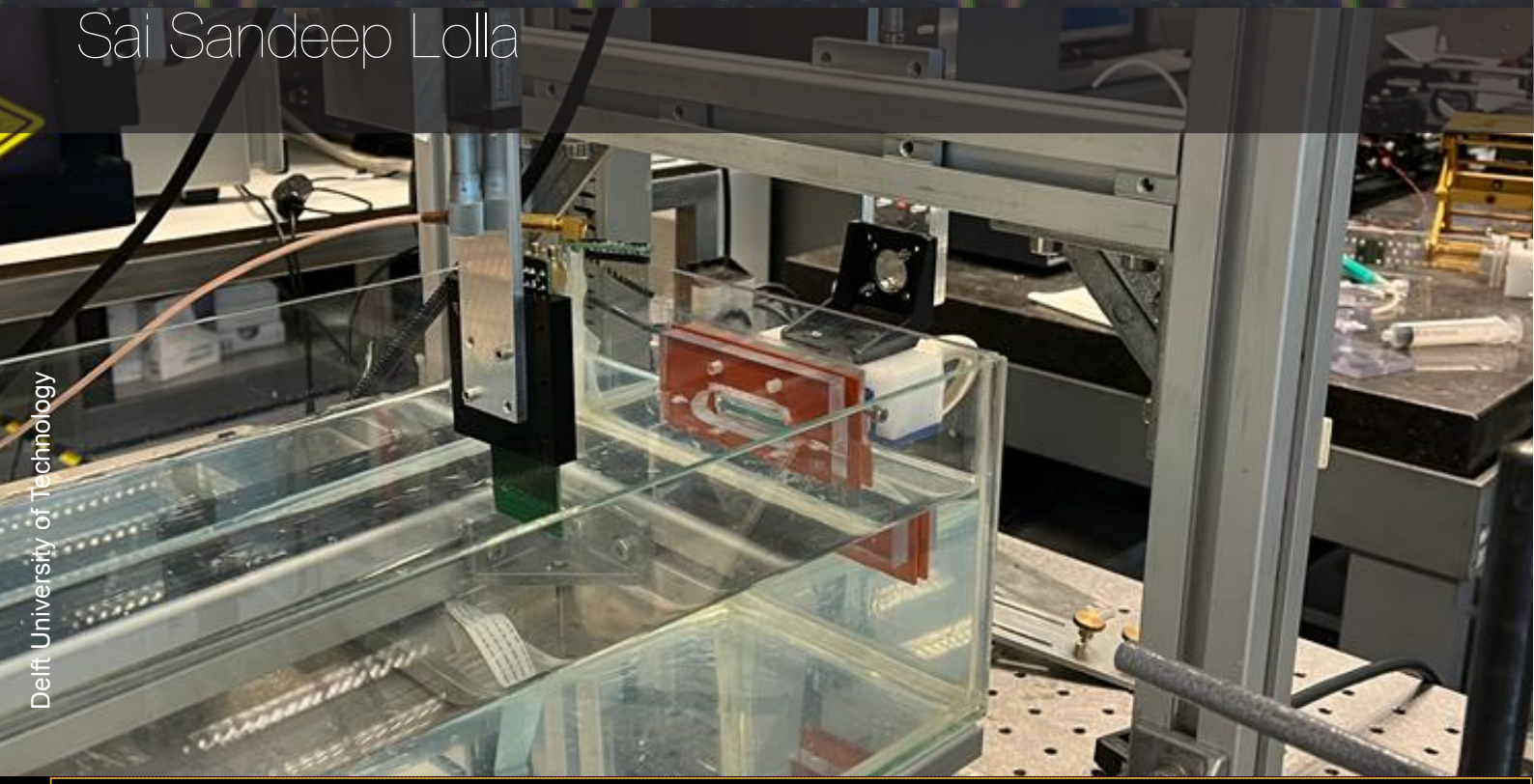

Delft University of Technology

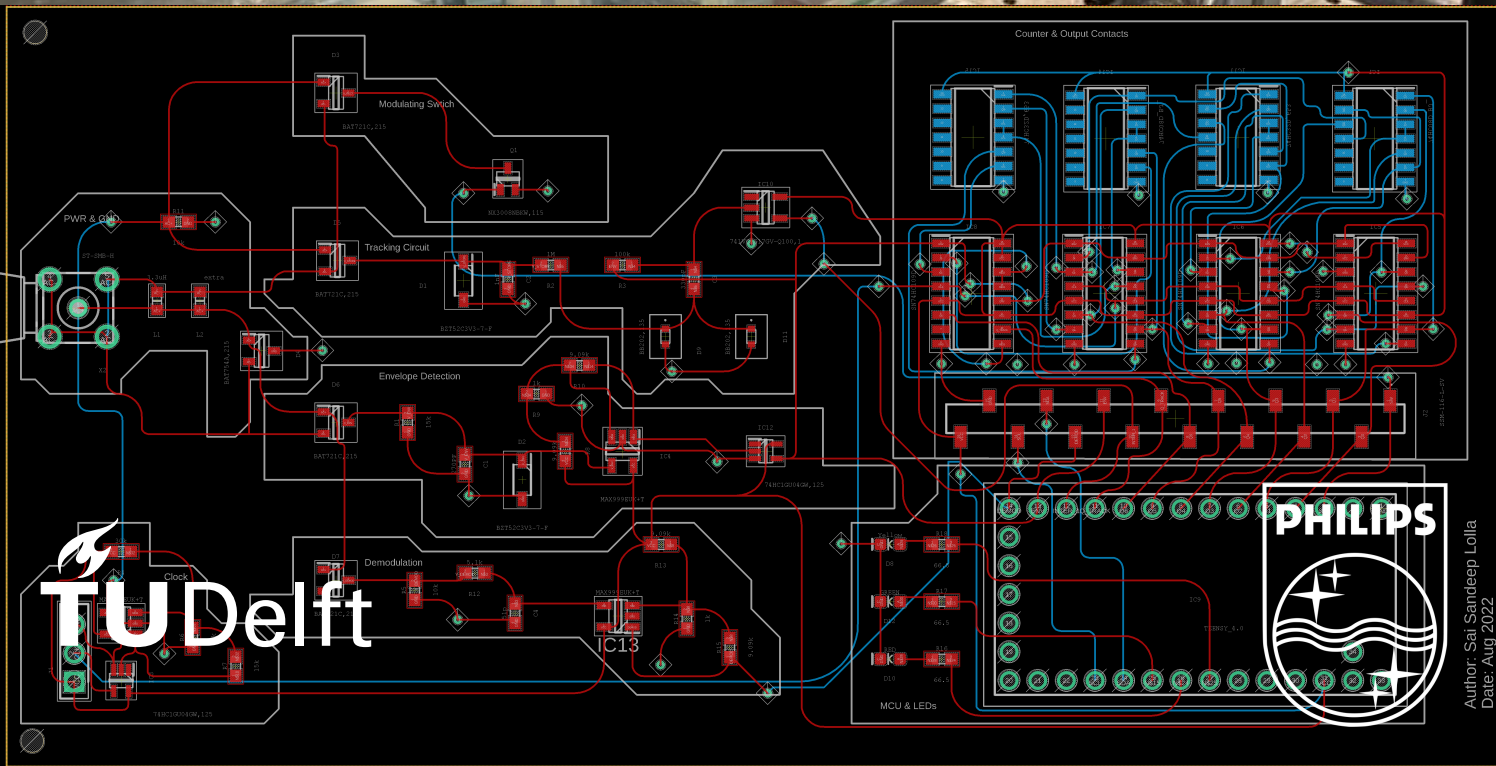

Ultrasound Tracking and Data Telemetry using CMUTs

by

Sai Sandeep Lolla

in partial fulfillment of the requirements for the degree of

Master of Science
in Electrical Engineering

at the Delft University of Technology,
to be defended publicly on Tuesday November 22, 2022 at 14:00 hrs (CET).

Supervisors::	Prof. dr. ir. Ronald Dekker,	TU Delft and Philips
	Ir. Marta Saccher,	TU Delft
Institution:	Delft University of Technology	
Student number:	5270413	
Place:	Faculty of Electrical Engineering, Mathematics and Computer Science, Delft	
Project Duration:	December, 2021 - November, 2022	
Thesis Committee:	Prof. dr. ir. Ronald Dekker,	TU Delft and Philips
	Dr. ir. Michiel Pertijs	TU Delft
	Ir. Marta Saccher,	TU Delft

TU Delft PHILIPS

Abstract

Implantable Medical Devices (IMDs) offer a wide range of applications including but not limited to blood pressure monitoring, bladder pressure sensing, glucose level monitoring, neurostimulation etc. For such applications, it is often desired that an IMD is as small as possible while meeting the required objective. Consequently, using a battery as a power source for this miniaturized IMD is inhibited as it occupies huge space. A good alternative for the battery as the power source is the Wireless Power Transfer (WPT) method. Among the WPT techniques, ultrasound (US) has seen increasing popularity in the past decade owing to its unique advantages such as better resolution, lower propagation attenuation, better health benefits etc. Ultrasound WPT methods involve an ultrasound transducer that converts ultrasonic energy into electrical energy to power the IMD. One such transducer is the Capacitive Micromachined Ultrasound Transducer (CMUT). As the name suggests it is a capacitive ultrasound transducer that is micromachined on silicon substrates. Accordingly, this technology offers advantages such as the ability to integrate with CMOS technology, larger bandwidth and the ability to fabricate large arrays of these transducers. Previous research in CMUTs has proven that the CMUTs can be used to efficiently harvest US energy at depths of more than 100 mm. Consequently, this paves the foundation for miniaturized US-based implants that can be placed deep inside the human body, using CMUT technology.

Building on this foundation, this thesis work explores the next steps in realizing a CMUT based implant. Two research questions are the main focus of this work: 1. How can we locate such small sized deep implants in order to transfer power efficiently? 2. How can we communicate with this device using ultrasound waves? Addressing the first issue, a Time Reversal beamforming based tracking algorithm is developed that is able to track CMUTs occupying a surface area of about 6.3 mm^2 moving at speeds up to 1.25 mm/s in water. Addressing the second issue, a communication protocol is formulated to establish ultrasound communication. This protocol makes use of the focused US beam achieved during tracking to communicate while offering simultaneous power transfer. A data rate of 2 kb/s is achieved using this protocol when the transmitter (TX) and the receiver (RX) are separated by a distance of 130 mm with a phantom filling up the gap.

US based IMDs can be built to occupy only a few mm^2 of area, especially when using micromachined transducers such as CMUTs. This work, the tracking algorithm and the communication protocol further provide proof of concept for reliable localization of CMUTs and low power data communication, hence providing good prospects for CMUT applications in the field of Implantable Medical Devices.

Keywords: Ultrasound, CMUT, time reversal, data communication.

Acknowledgments

I have many people to thank for helping me for the past year and three months.

Ronald, Thank you for being always cheerful and understanding. Thank you for giving me the opportunity to do my internship at Philips.

Marta, thank you for always helping me out and checking up on me every day. You have been a big help during my internship.

Eugene, thank you for helping me out with my setup. Thank you for being cheerful and funny from time to time. Johan, thank you for providing smooth onboarding for my internship. You made all the official work very smooth and comfortable for me, Thank you.

Silvana, Sara, Annemijn, Cecile, Maria and Laurent thank you for giving me great company during my time at Philips. I always enjoyed hanging out with you people.

Shin, thank you for supervising me at the start of my thesis. It was always fun having you around. Jia Jun, thank you for being a good senior and a friend. I have learnt a lot from you and always had fun hanging out with you. Jian, it was always fun hanging out with you during lunch. Hope you keep spreading the joy around.

Raja, thank you for always responding quickly and helping me out with the verasonics. All Philips researchers, thank you for being so welcoming while helping and providing guidance.

Lastly, I would like to thank my parents and my brother. Thank you for always supporting me by checking up on me daily and always worrying about me. I could not have done it without your support.

Sai Sandeep Lolla
Delft, November 2022

Contents

List of Figures

List of Tables

1

Introduction

An implantable bio-medical device can be powered in three ways using Batteries, Energy Harvesters and Wireless Transfer methods. Batteries are reliable and portable, which usually makes them the first choice for a power source. However, batteries have a few limitations. They need to be surgically replaced after their lifetime and occupy up to 80% of the implant volume [1]. There is always a possibility of toxic leakage inside the human body. Implants have already scaled down to sizes of dimensions in mm. Batteries fail to supply energy when they are used in such small dimensions [2]. Energy harvesters harvest energy from the environment or the human body. Hence harvesters of various kinds are available such as Bio-chemical, Bio-mechanical, Thermometric, etc. On the other hand, energy harvesters offer low power levels, are unreliable and often need complex power management circuits [3]. Wireless power transfer methods show good prospects since they are externally powered using reliable sources and are safe for the human body. This motivates scientists to perform research in Wireless Power Transfer (WPT) methods.

Among the WPT methods, three power transfer mechanisms have proven to be viable: Ultrasonic, Electromagnetic and Optical power transmission. Electromagnetic power transfer has many forms, namely: Inductive coupling, Capacitive coupling and Radio-Frequency (RF) energy transfer. Inductive coupling transfers power using magnetic fields by establishing mutual inductance between two coils. Capacitive coupling establishes an electrostatic field between two conductors, one inside the human body and the other on the outside of the human body, hence forming a capacitor. Placing another similar pair of conductors (another capacitor) will complete the electrical circuit and the implant can be powered [3]. RF transmission involves transmitting RF waves in the direction of the implant. An antenna inside the human body harvests the energy from these waves to power the implant. Optical power transfer involves a Photo-Voltaic (PV) cell receiving power from optical waves that pass through tissues to reach the implant [3].

Table 1.1 shows a summary of wireless power transfer methods. An example of all kinds of WPT methods discussed above in shown in this table. It can be seen that inductive and capacitive coupling offer very high power transfer efficiency when the receiver (RX) and transmitter (TX) distance is less (few mm) and the RX is large (few hundred mm^2). Inductive and Capacitive WPT requires: large coils/ conductors, very low misalignment and limited distance between the coils/ conductors for better flux linkage/power transfer efficiency. It also requires low operating frequency (few hundred MHz) to lower both the dissipation of power and the rise in temperature in the tissue [1], [14]. RF power transmission can be seen to offer very low power transfer efficiency when the RX antenna are a few mm^2 in size. As the implantation depth increases the RF attenuation increases thereby decreasing the efficiency further [15]. These small sized antenna offer small radiation resistance that therefore harvest lower power from the RF waves. RF waves with frequency less than 10 GHz (wavelength > 30 cm) also suffer from antenna misalignment as the implant size reduces to few mm. Optical power transfer method can be seen to seen to have low penetration depth (few mm) and large (RX) area (few tens of mm^2). Optical WPT also suffers from low PV cell efficiency and risk of rise in skin temperature [1], [3].

Ultrasound (US) power transfer utilizes ultrasound transducers to convert incident acoustic waves in electrical signals, hence harvest energy from ultrasound waves. As shown in Table 1.1, US power transfer offers good power transfer efficiencies when powering small implants (few mm^2) that are lo-

Table 1.1: Summary of Wireless Power Transfer methods.

S.no	Power at RX	Efficiency (%)	Frequency (f) (MHz)/ Wavelength (λ)(nm)	RX-TX distance (mm)	Size of RX coil/ antenna/ transducer (mm^2)	Application	Power Strategy
1	∼	81	13.65 (f)	10	78.54	Model based simulation of inductive power transfer [4]	Inductive Coupling
2	∼	0.1	900 (f)	1.5	1.8	Glucose sensing for artificial pancreas [5]	Inductive Coupling
3	55.5 µW	0.002	1180 (f)	6.6	0.1	Neuro-stimulator [6]	Inductive Coupling
4	90 mW	35	∼	2	300	WPT [7]	Capacitive Coupling
5	75 mW	10	120 (f)	2	800	WPT [8]	Capacitive Coupling
6	195 µW	0.04	1600 (f)	50	0.785	Wireless cardiac pacemaker [9]	Mid range RF
7	∼	0.03	1200 (f)	58	46	Antenna design for WPT[10]	Mid range RF
8	4.2 mW	16.6	750 (λ)	3	90	Wireless battery charging [11]	Optical WPT
9	37.7 µW	∼	1.78 (f)	50	0.56	Neuro-recording [12]	Ultrasound
10	805 µW	48.8	5.85 (f)	176	< 2.5	US WPT [13]	Naturally focused US

cated deep inside the body (few cm). In comparison with EM power transfer US power transfer offers some unique advantages:

1. US waves have wave propagation speed that is several orders of magnitude lower than that of EM waves. Consequently, ultrasound waves travel with lower wavelengths when both the waves are operated at same frequencies. This directly implies that the implants needed for power transfer can be designed to be much smaller. [16].
2. Considering a similar sized implant, the range of operating frequency for electromagnetic power transfer (in the range of GHz) is much higher than that of ultrasound power transfer (< 20 MHz). RF power transfer therefore results in higher dynamic power loss. RF waves with frequency greater than 1 GHz suffer from at least 10 dB/cm attenuation in the biological tissues and US waves suffer from less attenuation between 0.5 and 1 dB/cm/MHz. [17], [18].
3. Inductive coupling requires very precise alignment and a small distance between the harvesting coils; one inside and one outside the body. It was seen that for deeper and smaller implants; ultrasound power transfer is more efficient than inductive coupling [4].
4. Smaller wavelengths enable ultrasound waves to focus into mm-sized spots. Focusing of wavefronts reduces the beamwidth. This in turn reduces the power required to compensate for power loss due to transmission media and increases the transfer efficiency of the established link.
5. Ultrasound offers an exposure limit of 720 mW/cm^2 [19]. On the other hand electromagnetic field exposure limit is less than 10 mW/cm^2 for frequencies greater than 100 MHz i.e. RF operating range. The electromagnetic exposure limit for frequencies between 10 kHz to 10 MHz (inductive operating range) is relatively higher, even more than 100 mW/cm^2 [2], [20]. However, RF and inductive coupling, due to their varying electric and magnetic fields; can lead to body currents. These body currents in turn cause localized heating [1]. Ultrasound power transfer, therefore, provides better health conditions for the users.
6. Ultrasound waves are mechanical waves that are usually operated in frequencies ranging between a few hundred kHz to 20 MHz. Hence US waves are immune to electromagnetic interference.

Based on the above mentioned advantages it is clear that ultrasound power transfer is more suitable than electromagnetic power transfer for biomedical implants in humans. This is especially true when the implant is small and placed deep inside the human body.

Go to ToC

1.1. Motivation & Objective

US as a mode for power transfer clearly has good prospects. Interacting with a biomedical implant involves powering of the device along with communication. Being an emerging technology it poses many challenges in order to realize its full potential. Since implants are shrinking to sizes of sub mm^2, establishing a viable US link to power and communicating with the implant becomes difficult in case we are not aware of the location of the implant. This viable link focuses US waves on the implant. Previous research has shown that the power received by the implants can reduce by 70 % when there is 0.5° shift in the focused ultrasound beam i.e. about a 1 mm shift from the implant's location in the lateral direction of the beam's axis [21]. Furthermore, in case we are able to establish a link to transfer power, what would be a good way to communicate with the device? Can we use US to communicate since a viable US link is now established?

Interacting with an implant using US can be viewed in three steps:

1. Perform typical B-Mode imaging [22] to estimate the implant's location and transmit focused/plane US waves towards the implant to provide initial power-up.
2. Track the powered up implant to focus the US waves exactly on the implant's transducer.
3. Utilize the established focus US link to power up and communicate with the implant.

Previous work at Philips Research, Eindhoven focused on establishing effective power transfer and formulating a protocol to track the implant (Step 1) [13], [21], [23]. An experimental setup was built to test ultrasonic power transfer using Capacitive Micromachined Ultrasound Transducers (CMUTs), and an initial telemetry circuit was designed to communicate the current power being harvested by the CMUTs to an external receiver. The objective of this thesis is to proceed further and perform Steps 2 & 3 of the interaction with CMUTs. Accordingly, a tracking algorithm based on the protocol developed in [23] and a communication protocol implementing forward and back telemetry, are formulated in this work.

1.2. Background

Beginning with introduction to CMUT technology, this section discusses previous research performed in [13]. This includes Ultrasound Energy Harvesting and Impedance Spectrum Analysis of CMUTs. Finally, Verasonics Vantage System is discussed which is used to generate and visualize US waves.

1.2.1. CMUT Technology

Capacitive Micromachined Ultrasound Transducer, as the name suggests, converts acoustic energy to electrical energy and vice-versa [24]. Two electrodes, one movable and one fixed (as shown in Fig. 1.1a) with a dielectric between them, show capacitive behaviour when connected across a circuit. The movable electrode is sensitive to acoustic waves. Hence the vibrations in the movable electrode causes change in capacitance which is read out to measure the acoustic pressure.

Usually, CMUTs are operated in collapse mode for power transfer applications. They are operated under a DC bias voltage to close the gap between the top (movable) and bottom (fixed) electrode. In transmitting mode, an electrical AC signal is super-imposed on this bias voltage, which gets converted into ultrasound waves. In receiving mode, the incident ultrasound waves appear as an electrical AC signal over the DC bias voltage. The above mentioned DC bias voltage is increased beyond pull-in (collapse) voltage (voltage high enough to bring the two electrodes in closed contact) and then decreased to desired value while maintaining the close contact [25]. The collapse mode, due to a very low distance between the electrodes, operates in high electric field (see Fig. 1.1a). This provides a better pressure sensitivity and hence greater transfer efficiency [26].

The DC bias is not always required to be given externally if certain changes are made to the dielectric layer. Al_2O_3, a high-*K* material has the ability to trap charges [27]. This material can be included in the dielectric stack to eliminate the need of external bias. To achieve this, the dielectric stack is charged by applying high DC voltage, high enough to tunnel charge carriers, but lower than breakdown voltage of the dielectric. This high voltage transforms the CMUTs into an electret, ultimately acting as an internal DC bias [28]. This principle was previously explored at Philips Research, Eindhoven. The dielectric layer was altered to incorporate a stack of $SiO_2/Al_2O_3/SiO_2$ on top of the bottom electrode with a pull-in voltage of 40V. A 200V DC voltage was applied for 3 hours to trap the charges. The top layer stayed in contact with the bottom stack of high-*K* layers (collapse mode) after removal of the bias voltage [13]

(see fig 1.1b). A 2-D array (Fig 1.2) of this CMUT device is used in this work. The array consists of CMUT drums with a diameter of 135 µm. The array is arranged with 6 CMUT drums in a single column (top to bottom) and all the columns are placed next to each other (left to right). All the CMUT drums are electrically connected in parallel, to increase the amplitude of the output signal from the incident acoustic waves. Furthermore each connector connects 6 elements (columns) on the array i.e. a total of 336 drums. In this work, a single connector is being used, hence 336 CMUT drums are in operation which spans an area of about 6.3 mm^2 [23].

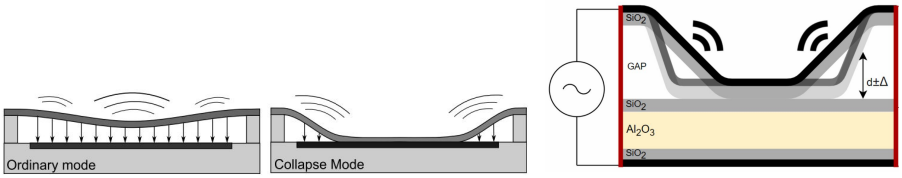

(a) CMUT operated ordinarily and in collapse mode [29]. **(b)** CMUT device used in this work [21].

Figure 1.1: CMUT device

Figure 1.2: PCB with a 2-D array of CMUTs and 4 SMB connectors connecting to 336 CMUT drums [21].

1.2.2. Ultrasound Energy Harvesting

Efficiency is a very important factor determining the performance of a power transfer link. For optimum energy harvesting, it is therefore necessary to understand the characteristics of the CMUT. Figure 1.3 shows the electrical equivalent circuit diagram of a CMUT. As mentioned in section 1.2.1, there is one movable and one fixed electrode. The movable electrode is represented as a mass attached to a spring. It's electrical equivalent consists of a series connection of a resistor (damper - b), capacitor (spring - k) and an inductor (mass - m). The change in the capacitance caused by the moving electrode's displacement is represented by a variable capacitor (C_e). The transformer (n:1) represents the conversion between electrical and acoustic energy. The $Z_{electrical}$ is the impedance representing the rest of the circuit connected to the CMUT [13].

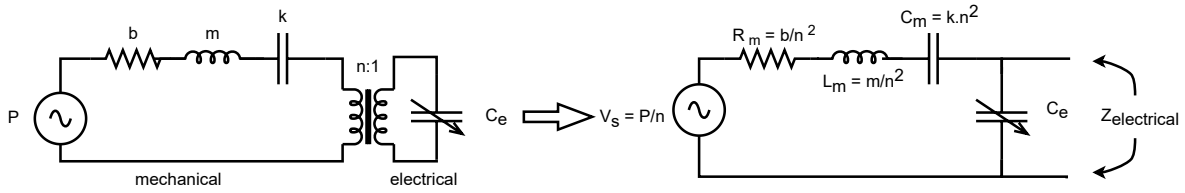

Figure 1.3: Equivalent electrical circuit diagram of a CMUT [13].

To maximize the amount of energy harvested by the CMUT, the maximum power transfer theorem must be applied to this circuit. Accordingly, the load and source impedances must be matched i.e. they must be complex conjugates. This can also be interpreted as matching the real components of source & load impedances and making the reactive components, equal and opposite to compensate each other. By doing this, all of the incident energy is transferred to the load instead of being stored

in the reactive elements. This is done as follows: 1) operating the CMUT at it's resonance frequency, by which C_m and L_m compensate each other, 2) using a matching inductor (L_l) to compensate for C_e. Furthermore, the load resistor (R_l) must also match R_m for maximum power transfer (Fig. 1.4) . The following equations sums up the necessary additions that needs to be made [13] (also shown in Figure 1.4)

$$L_l = \frac{1}{2 \cdot \pi \cdot f_{US}^2 \cdot C_e}; \quad R_l = R_m \tag{1.1}$$

where f_{US} = ultrasound burst frequency.

For optimal energy harvesting using a collapse-mode CMUT, it is therefore necessary to operate the device at or near the resonance frequency along with a suitable compensating inductor and resistor. In order to find the compensating inductor and resistor, the CMUT's electrical equivalent components' value must be known. These values can be found by using Impedance Spectrum Analysis.

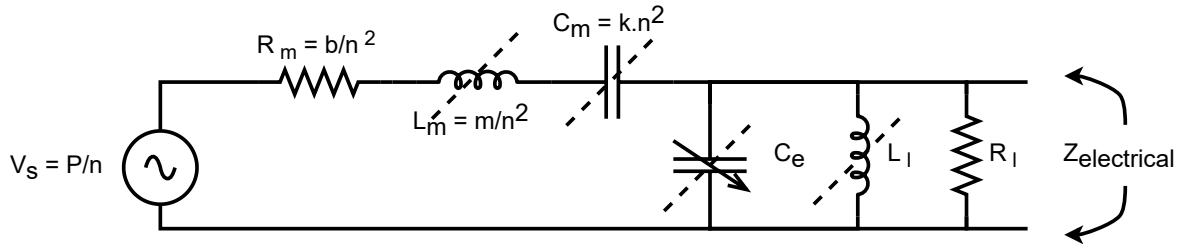

Figure 1.4: Compensated CMUT for maximum energy harvesting.

1.2.3. Impedance Spectrum Analysis of CMUTs

In order to obtain the CMUT's impedance spectrum, one of the SMB connector of the CMUT PCB (Fig 1.2) is connected to an impedance analyser (Agilent 4294A Precision Impedance Analyser) with air being the surrounding medium. Hence the frequency spectrum of $Z_{electrical}$ as shown in Figure 1.3 will be measured using the impedance analyser. Figure 1.5 shows the measured frequency response of $Z_{electrical}$ of CMUT type P103, that is used in this work. At resonance, the phase of the impedance is the highest (closest to zero) indicating very less reactive impedance. From the phase spectrum the resonance frequency (f_{res}) is measured to be 2.567 MHz.

From the electrical equivalent circuit (Fig 1.3), an expression for $Z_{electrical}$ can be derived:

$$Z_{electrical}(s) = \frac{s^2 + \frac{R_m}{L_m}s + \frac{1}{L_m C_m}}{(C_e s)(s^2 + \frac{R_m}{L_m}s + \frac{C_m + C_e}{L_m C_m})} \tag{1.2}$$

Using the above equation and the measured impedance spectrum (Fig 1.5), the equivalent circuit component values can be estimated. At very high frequencies, $Z_{electrical}$ simplifies as follows:

$$Z_{electrical}(s) \approx \frac{1}{C_e s}; \quad f \gg f_{res} \tag{1.3}$$

The high frequency impedance spectrum curve in a log-log scale can thus be compared with the curve generated by the above mentioned equation to estimate the value of C_e. Similarly at frequencies much lower than the resonance frequencies, $Z_{electrical}$ simplifies to

$$Z_{electrical}(s) \approx \frac{1}{C_e s(C_m + C_e)}; \quad f \ll f_{res} \tag{1.4}$$

Similar to C_e ,C_m can be estimated from the above equation. Since at resonance:

$$L_m = \frac{1}{\omega_{res}^2 C_m}; \quad \omega_{res} = 2\pi f_{res} \tag{1.5}$$

Consequently, L_m can also be calculated. R_m is estimated by extrapolating the measured curve to zero frequency. This extrapolation along with estimation of other parameters is performed in Python [13] and the following values are estimated as follows:

Go to ToC

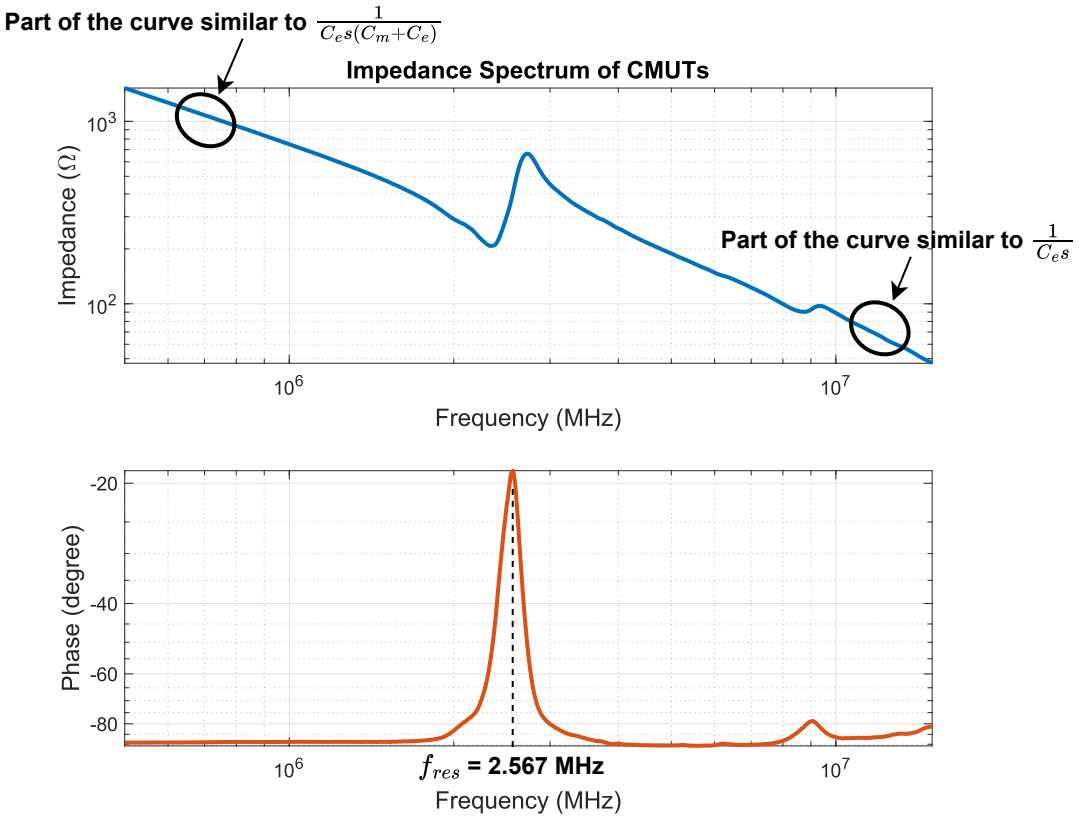

Figure 1.5: Impedance Spectrum of CMUTs (type - P103).

Table 1.2: Extracted CMUT equivalent circuit component values.

f_{res}[MHz]	C_e[pF]	C_m[pF]	L_m[μH]	R_m[Ω]
2.567	143	72.8	52.8	386.99

In this work, a Philips L7-4 ultrasound probe is used to perform various experiments. The burst frequency of 4 MHz is used in this work. The corresponding matching inductor L_l calculated from the above values and 4 MHz of the burst frequency is 1.845 μH [1] (refer Equation 1.1). Similarly, the matching resistor R_l needs to be of 387 Ω. It should be noted that since the impedance spectrum analysis is performed with air as the surrounding medium, the above mentioned R_m and hence R_l would be slightly different during an experiment since the US propagation medium would be a phantom composed of candle gel (95% paraffin oil and 5% organic constituents) instead of air [23].

It should be noted here that the equivalent circuit component values are extracted by comparing different parts of the impedance spectrum curve with those of approximated impedance functions (Eq 1.3 & 1.4). This type of estimation previously showed a match of up to 93 % between the approximated impedance spectrum curve and the original impedance spectrum curve [13]. Therefore the value of 1.845 μH for the matching inductor serves as a good starting point for figuring out the right value of the matching inductor. The right value of the matching inductor and resistor is found out by connecting discrete indicators and resistors across the two terminals of CMUTs, which is further discussed in Section 3.3.

[1] It should be noted that the value of C_e shown in Table 1.2 is of a single column of CMUT drums. A compensating inductor connects to 6 such columns of CMUT drums since it is externally connected using the SMB connector. Therefore L_l is calculated using 6*C_e instead of C_e.

1.2.4. Verasonics Vantage System

Verasonics research ultrasound platform is used to transmit, receive & visualize US waves in this work. Additionally, verasonics also provides the feature to perform image reconstruction as shown in Figure 1.6. The system consists of the vantage unit and a PC as shown in Figure 1.6. The main components of the vantage unit are the Scan Head Interface (SHI), Acquisition Modules, Back Plane module and Transmit Power Controller (TPC) (Fig 1.7). The SHI connects typical US transducers (probes) to the vantage unit. The Acquisition Modules consists the main electronics that include the transmitters, the receive channels, a 14 bit A/D converter, a Time Gain Control (TGC) amplifer and a filter (signal conditioning). The transmitters generate US waves and the waves received by the receive channels are digitized by the A/D converter & the signal conditioner and stored in the local memory of the module. The Back Plane module consists of the Hardware Sequencer, which is discussed later in this subsection. The TPC consists of the transmitter driver that generate the US waves. The PC is connected to the vantage unit using a PCI express (PCIe) cable. The US waves data stored in the local memory of the vantage unit is transferred to the PC's memory via Direct Memory Access (DMA). Hence the verasonics vantage system provides direct access to raw data of US waves.

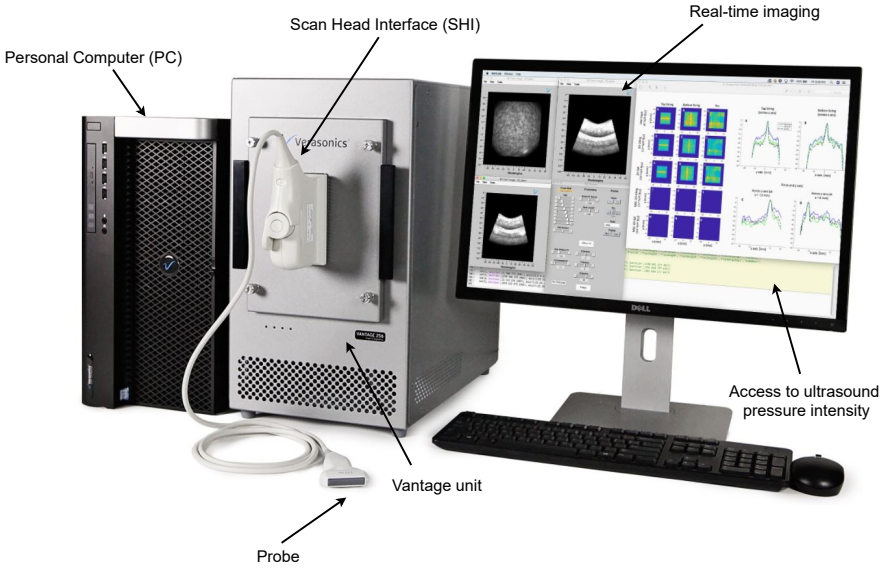

Figure 1.6: Verasonics Vantage System 256^{TM} [30]

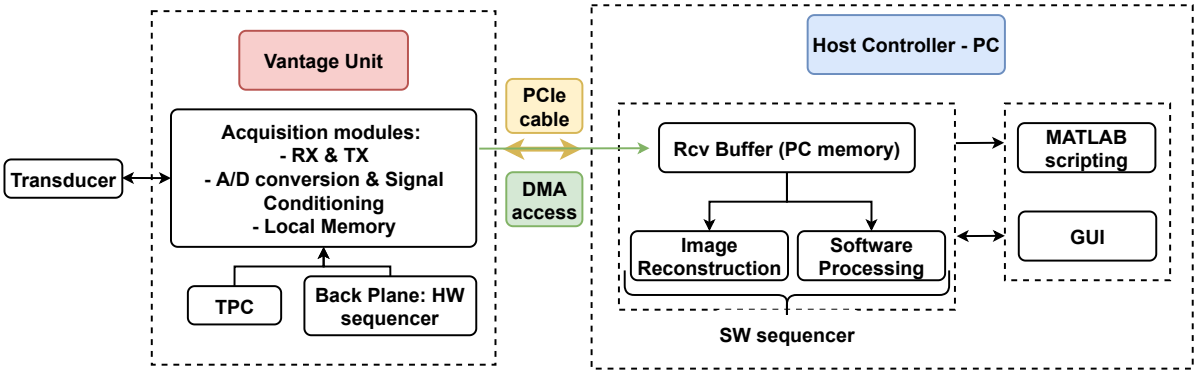

Figure 1.7: Block diagram depicting the internal components of the Vantage unit and the Host controller (PC). Figure is revised from [31].

MATLAB is used to program the verasonics where the US data can be visualised and manipulated. Furthermore, various parameters of the above mentioned components of the vantage system can be tuned on MATLAB during scripting or by using the Graphical User Interface (GUI) that opens when any verasonics script is run (Fig 1.7). The MATLAB scripting used in the verasonics programs the

Go to ToC

Hardware Sequencer and the Software Sequencer of the system using structure data types. The Software Sequencer sets the sequence of image reconstruction and software processing of the US raw data available in the PC's memory. The Hardware Sequencer, based inside the Back Plane, handles the sequence of the transmitting and receiving events.

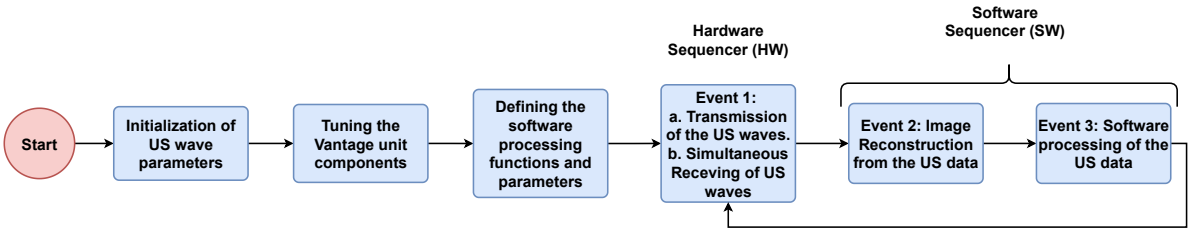

Figure 1.8: A flow diagram depicting the MATLAB scripting used in verasonics.

Figure 1.8 depicts a flowchart of MATLAB programming of a typical verasonics script. The scripts starts with defining the parameters of the US waves and the components used in the Vantage unit. One of the three structures mentioned below can be used to define the type and shape of the US wave that is desired to be transmitted.

1. Parametric structure: This structure allows to set 4 parameters of an US burst that are burst frequency in MHz (A), pulse width of the half cycle (B), number of half cycles (C) and polarity of first burst.
   Syntax: TW(i).parameters = [A,B,C,D];
   Example: TW(1).parameters = [4,0.67,48,1];
   The example defines a sinusoidal (B = 0.67) burst of 4 MHz (A = 4) transmit frequency that contains 24 cycles (C = 48) starting with positive polarity (D = 1).
2. Envelope structure: This structure allows to define the frequency (f_1, f_2, f_3, ... f_N) and pulse width (pw_1, pw_2, pw_3, ... pw_N) of every individual cycle in an US burst with 'N' number of cycles.
   Syntax: TW(i).envNumCycles = N;
   TW(i).envFrequency = [f_1, f_2, f_3, ... f_N];
   TW(i).envPulseWidth = [pw_1, pw_2, pw_3, ... pw_N];
3. Pulsecode structure: This structure allows to define any arbitrary shape for the US burst that is transmitted. Usually the verasonics converts the parametric or the envelope structure into pulsecode structure to generate the US burst. Refer to the Vantage Sequence Programming Manual for more information.

The envelope structure and the parametric structure is used in this work to define the forward telemetry and back telemetry waveforms respectively. While tuning the components, the vantage unit must be instructed to set a particular profile for the Transmit Power Controller (TPC). A TPC profile defines the power limit and requirement of the transmitters. It defines the upper limits of the voltage and the operating duration that can be used to drive the transducer elements. The driving voltage can be set anywhere between 1 - 96 V. Although a limit of 20 V is programmed for diagnostic imaging or any other purpose, as a general practice. The operating duration can be set in modes, called TPC profiles. These profiles define the transmit power limit and hence also the operating duration. The TPC profile are:

1. Normal Transmit mode: This mode is used to transmit short duration US pulses that are typically used in diagnostic imaging. The vantage system allows to transmit a maximum of 24 cycles of 4 MHz burst frequency with a Pulse Repetition Frequency of 1 kHz. This US burst is also used in US power transfer [21] and tracking of implant implemented in this work [23].
2. Extended Transmit mode: This mode is provided by the Vantage system to stimulate tissue using ultrasound. This mode utilizes a dedicated 48 W internal power supply to drive the transmitter channels that can generate burst with burst duration of few ms. This mode is used to implement forward and back telemetry in this work.
3. High Intensity Focused Ultrasound (HIFU) mode: This mode is provided to implement therapeutic applications using verasonics. Using this mode, an external power supply can be connected to

transmit US burst with power levels upto 1200 W. Any desired combination of burst duration and PRF can be programmed with burst frequency between 1 MHz and 5 MHz only.

After the US burst parameters and the Vantage unit component parameters are defined, the software processing function is defined. In this work, this definition includes computing the envelope of the received burst, subtraction of the envelopes, finding peaks in the envelope, computing delays between two bursts and image reconstruction. These definitions find use in the tracking algorithm which is discussed in Section 2.8. Moving further, the script enters into an infinite loop where the Hardware and the Software sequencers perform burst transmission, receiving the burst, image reconstruction and software processing (Fig 1.8). This infinite loop starts with the hardware sequencer transmitting and receiving US waves at the same time. The transmitted waves travel towards the CMUTs, reflect back and reach the probe, which is when the receive channels sense an US wave. The HW sequencer is made to pause after Event 1. The SW sequencer performs the necessary image reconstruction and software processing of the US data. When the SW sequencer completes Event 2 and 3, the HW sequencer is released to perform the next acquisition (transmit and receive).
This marks the end of the Introduction Chapter. Moving further in this report, Chapter 2 discusses the first objective which is tracking a biomedical implant using US waves. Chapter 3 discusses the second objective of this thesis which is US based communication with a biomedical implant. In both these cases CMUTs are used as the US transducer and the CMUT 2-D array is addressed as the biomedical implant.

2

Tracking of Biomedical Implants

2.1. Introduction

Implantable bio-medical devices are also seeing a trend of decreasing dimensions. Current wireless implants developed to stimulate and record the brain and peripheral nerves have dimensions of mm and sub-mm [2]. This miniaturization provides benefits such as more precise access to the target regions, less intense foreign body response and compatibility with minimally invasive surgical procedures for implantation [32], [33]. However, the decrease in the device size and the increase in the depth of implantation proportionally increases the difficulty in maintaining a link between the implanted device and the outside world, either for efficient power transfer or good quality data communication. Knowing the location of the implant helps in many ways such as:

1. developing a targeted wireless link for efficient power transfer and less erroneous data transfer.
2. improving spatial awareness of the device to locate lesions and other structures in wireless capsule endoscopy [34].
3. performing therapeutic operations such as drug delivery for targeted tumors while avoiding healthy tissues [35].
4. maneuvering micro-robots or capsule endoscopes for surgeries and providing more information about the insides of the small intestine for research and education [36], [37].

Therefore it is necessary to keep track of the location of the biomedical implant inside the human body. The localization of implantable devices can be performed using many methods involving Magnetic Fields, Electro-Magnetic (EM) Waves, Ultrasound, X-rays, Computer Vision etc [38]. Magnetic fields, particularly the static and low frequency components do not attenuate inside the human body and the implant inside the human body does not require a line of sight to interact with these fields [39]. Methods similar to power transfer and communication using EM waves can be employed to track a biomedical implant. Owing to the miniaturization of semiconductor devices EM waves based tracking can provide low cost, small and feasible solutions [38]. Both magnetic field based and EM waves based localization strategies offer good accuracy [40]. Such reasons ultimately resulted in significant research in magnetic and electromagnetic localization methods. However, while considering magnetic localization methods, for precise results, the medical devices and the equipment in the surroundings need to be non-ferromagnetic in order to not distort the operating magnetic fields. The use of a permanent magnet or a magnetic coil inside the implant for interacting with the magnetic fields may restrict the size of the device itself [39]. EM waves see significant attenuation of their amplitude while propagating through human tissue, which again increases with the increase in frequency [2], [20]. Therefore electromagnetic localization methods become less reliable for small sized and deep implants.

Ultrasound waves, as mentioned previously in Chapter 1, is clearly more compatible with human tissue when compared with EM waves. Additionally ultrasound power transfer is more reliable for small sized deep implants. Although ultrasound waves need a line of sight between the transmitter and receiver for operation, they can be implemented with small sized transducers and are immune to EM

fields. These reasons assuredly imply good prospects for localization of biomedical implants using ultrasound waves. Therefore in this work, ultrasound based localization strategies of implantable devices are studied and a localization strategy is developed. Based on the literature search, a computationally simple and a fast tracking algorithm is implemented to track a small element of a 2-D CMUT array. The following sections present this literature review followed by some background information, the tracking algorithm developed in this work and the experimental results implementing this algorithm.

2.2. Ultrasound Localization Methods

Ultrasound based localization can be broadly classified into two categories: active tracking and passive tracking [39]. Active tracking involves the use of an ultrasound emitter on the implant. The implant emits ultrasound waves which are received by the external transducers that can be processed to locate the origin of these waves i.e. the implant. In passive tracking, the external transducers emit ultrasound waves that travel towards the implant and gets reflected back (refer Section 2.5). Hence the external transducers receive an echo instead of a direct ultrasound burst. In order to receive an ultrasound echo, the reflected waves must travel back in the plane of the transducers and the implant. Active tracking offers more penetration depth since the waves travel only once in the media. It also does not have the reflection plane constraint. However from a bio-medical implant perspective, active tracking consumes considerably more power to drive an active ultrasound emitter, more than 100 µW [41]. Passive tracking on the other hand utilizes back-scattering. An ultrasound transducer can be embedded inside this implant to harvest part of the incident energy to its corresponding functions and the rest of the energy, that is reflected, can be processed for passive tracking. Despite the apparent advantages of ultrasound in terms of implant size, depth of implantation and compatibility with human tissue, little research has been performed in ultrasound based localization strategies since its alternatives involving magnetic field localization and EM wave localization provided good success. Table 2.1 shows a review of ultrasound based localization strategies found in the literature.

Ultrasound based localization utilizes the physical (wave) properties of the ultrasound waves namely: speed of sound, wavelength or frequency, time of travel in the media [42], [43]. The following sub sections describe how these parameters are utilized in the experiments performed in [44]–[50] to locate the ultrasound emitter/reflector (implant).

2.2.1. Time of Flight(ToF), Time of Arrival(ToA) & Time Difference of Arrival(TDoA)

Consider an ultrasound emitter (implant) situated at $\mathbf{x} = [x\ y]^T$ emitting ultrasound bursts and a few ultrasound transducers acting as external receivers situated around this emitter at $\mathbf{x}_l = [x_l\ y_l]^T,\ l = 1, 2, 3....L, L \geq 3$. These ultrasound bursts would reach the receivers at different Times of Arrival (ToA) denoted by ToA_l. Assuming the source started emitting ultrasound bursts at time $(t_0)_{ToA}$ and the l^{th} transducer received the burst at $(t_l)_{ToA}$, ToA_l can be expressed as $ToA_l = ((t_l)_{ToA} - (t_0)_{ToA})$. Furthermore, the distance equations can be written as follows:

$$d_l = |\mathbf{x} - \mathbf{x}_l| = \sqrt{(x - x_l)^2 + (y - y_l)^2},\ l = 1, 2, 3....L \tag{2.1}$$

Since speed and distance are related as follows:

$$ToA_l = \frac{d_l}{c} => \ c \cdot ToA_l = d_l = |\mathbf{x} - \mathbf{x}_l| => \begin{bmatrix} c \cdot ToA_1 \\ c \cdot ToA_2 \\ c \cdot ToA_3 \\ . \\ . \\ c \cdot ToA_L \end{bmatrix} = \begin{bmatrix} d_1 \\ d_2 \\ d_3 \\ . \\ . \\ d_L \end{bmatrix} \tag{2.2}$$

When measurement errors are also considered during computation:

$$\begin{bmatrix} c \cdot ToA_1 \\ c \cdot ToA_2 \\ c \cdot ToA_3 \\ . \\ . \\ c \cdot ToA_L \end{bmatrix} = \begin{bmatrix} d_1 \\ d_2 \\ d_3 \\ . \\ . \\ d_L \end{bmatrix} + \begin{bmatrix} n_{ToA,1} \\ n_{ToA,2} \\ n_{ToA,3} \\ . \\ . \\ n_{ToA,L} \end{bmatrix} => \begin{bmatrix} c \cdot ((t_1)_{ToA} - (t_0)_{ToA}) \\ c \cdot ((t_2)_{ToA} - (t_0)_{ToA}) \\ c \cdot ((t_3)_{ToA} - (t_0)_{ToA}) \\ . \\ . \\ c \cdot ((t_l)_{ToA} - (t_0)_{ToA}) \end{bmatrix} = \begin{bmatrix} \sqrt{(x - x_1)^2 + (y - y_1)^2} \\ \sqrt{(x - x_2)^2 + (y - y_2)^2} \\ \sqrt{(x - x_3)^2 + (y - y_3)^2} \\ . \\ . \\ \sqrt{(x - x_l)^2 + (y - y_l)^2} \end{bmatrix} + \begin{bmatrix} n_{ToA,1} \\ n_{ToA,2} \\ n_{ToA,3} \\ . \\ . \\ n_{ToA,L} \end{bmatrix} \tag{2.3}$$

Go to ToC

Table 2.1: Overview of ultrasound based localization methods in the literature.

S.no	Application	Highlights	Observations	
			Upsides (+)	Downsides (-)
1	Ultrasonic implant localization [44]	1. Passive back-scattering using 3rd harmonic contrasting. 2. non-linear optimization of ToA/TDoA equations using iterative steepest descent algorithm to reduce overall measurement noise.	Sub-mm accuracy using just three channels/transceivers.	Low SNR and the low amplitude level of the 3rd harmonic back-scattered signal. This makes the feasibility of localization and its accuracy quite dependent on the noise and amplitude level
2	Wireless acoustic emitter [45]	1. Use of a Wireless Resonant Magnetic Microactuator (WRMMA). 2. Use of three hydrophones and TDoA questions.	1. Active localization is achieved using a wireless ultrasound emitter driven from the harvested magnetic energy instead of any embedded power source. 2. This ultrasound acoustic emitter (WRMMA) occupies considerably less space than a conventional power source.	1. Localization of the emitter by solving the TDoA equations without using any linear/non-linear optimization techniques. 2. Achieved localization represents a probability region of the implant location. This region is dependent on the ultrasound emitter operating frequency. Higher emitter frequency implies a better estimate of emitter location. On the other hand, also mean the acoustic waves see higher attenuation while traveling toward the receivers(hydrophones).
3	Localization in heteroge-neous media [46]	1. Deriving the shape of the ultrasound wave-front using Finite Element Analysis (FE). 2. Comparison of three spatial tracking algorithms. 3. Use Linear Least Squares method to solve for the emitter location.	1. Spatial error of less than 1mm achieved using Finite Element based algorithm for over 100 measurements. 2. The FE analysis accounts for different speeds in the traveling medium and hence is useful in a heterogeneous media.	Wavefront parameters require solving exponential and polynomial equations. This requires heavy computations.
4	Real-time imaging of a metallic device [47]	1. Based on the idea of smooth surfaces have a high reflection coefficient. 2. Use of Frangi filtering and Delay-Variance Beamforming instead of the common Delay-Sum Beamforming.	1. Both the location and orientation of the specular reflector (metallic device) are detected. 2. Better contrast and differentiation between tissue and specular reflectors can be achieved.	1. Orientation detection is limited to the probe aperture and distance from the probe. 2. Filter fine-tuning needs to be adjusted for different reflectors and their orientation.
5	Capsule tracking in GI tract [48]	1. Use of ToF equations and triangulation for object localization. 2. Use of a capsule with a transmitter, receiver and microcontroller attached to it.	-	1. Multi-path effect caused by more than one reflection can lead to incorrect detection of the capsule's position. 2. Accuracy of only a few centimeters (error less than 3cm) is reported which needs to be improved.
6	Navigation of robotic capsule [49]	1. Use of a permanent magnet instead of actuators for locomotion of the capsule. 2. Sonographic imaging for tracking the metal capsule.	1. Positioning accuracy of less than 2 mm. 2. Real-time visualization of the capsule movements is available for the physician.	Imaging is not able to differentiate between the capsule and the tissue behind the capsule. A false sense of navigation can be achieved.
7	Powering of biomedical ultrasound implants [50], [51]	1. Focus and steer of ultrasound beam to power multiple implants at different locations. 2. Time reversal of ultrasonic 'ping' produced by the implant or the echo bounced off the implant. 3. Comparison of beamforming methods.4. Careful selection of planar transducer array to maximize the power delivered to the implant.	1. Robust to tissue inhomogeneity, scattering, and change in the geometry of the transducer. 2. Use of alternate modulation of the bursts to distinguish the implant from other strong reflectors. 3. Efficiency as good as a beam focusing simulation is achieved. This implies the time reversal accurately locates the implant as well.	-

Go to ToC

where d_l = distance between the ultrasound emitter and l^{th} receiver, ToA_l = measured ToA for l^{th} receiver, c = speed of sound in media and $n_{ToA,l}$ = measurement errors for ToA.
In the case of passive tracking, the external transducers emit ultrasound bursts. These bursts reflect off of the implant and reach the receivers once again at different Times of Flight denoted by ToF_l. Assuming all the transducers started emitting the bursts at $(t_0)_{ToF}$ and l^{th} transducer received the reflected burst at $(t_l)_{ToF}$, ToF_l can be expressed as $ToF_l = (t_l)_{ToF} - (t_0)_{ToF}$. The distance equations can now be written as follows:

$$ToF_l = 2 \cdot \frac{d_l}{c} => \ c \cdot ToF_l = 2 \cdot d_l = 2 \cdot |\mathbf{x} - \mathbf{x}_l| => \begin{bmatrix} c \cdot ToF_1 \\ c \cdot ToF_2 \\ c \cdot ToF_3 \\ . \\ . \\ c \cdot ToF_L \end{bmatrix} = 2 \cdot \begin{bmatrix} d_1 \\ d_2 \\ d_3 \\ . \\ . \\ d_L \end{bmatrix} \tag{2.4}$$

$$\begin{bmatrix} c \cdot ToF_1 \\ c \cdot ToF_2 \\ c \cdot ToF_3 \\ . \\ . \\ c \cdot ToF_L \end{bmatrix} = 2 \cdot \begin{bmatrix} d_1 \\ d_2 \\ d_3 \\ . \\ . \\ d_L \end{bmatrix} + \begin{bmatrix} n_{ToF,1} \\ n_{ToF,2} \\ n_{ToF,3} \\ . \\ . \\ n_{ToF,L} \end{bmatrix} => \begin{bmatrix} c \cdot ((t_1)_{ToF} - (t_0)_{ToF}) \\ c \cdot ((t_2)_{ToF} - (t_0)_{ToF}) \\ c \cdot ((t_3)_{ToF} - (t_0)_{ToF}) \\ . \\ . \\ c \cdot ((t_l)_{ToF} - (t_0)_{ToF}) \end{bmatrix} = 2 \cdot \begin{bmatrix} \sqrt{(x-x_1)^2 + (y-y_1)^2} \\ \sqrt{(x-x_2)^2 + (y-y_2)^2} \\ \sqrt{(x-x_3)^2 + (y-y_3)^2} \\ . \\ . \\ \sqrt{(x-x_l)^2 + (y-y_l)^2} \end{bmatrix} + \begin{bmatrix} n_{ToF,1} \\ n_{ToF,2} \\ n_{ToF,3} \\ . \\ . \\ n_{ToF,L} \end{bmatrix} \tag{2.5}$$

where ToF_l = measured ToF for l^{th} receiver and $n_{ToF,l}$ = measurement errors for ToF.
In order to measure ToAs, synchronization between emitters and receivers is needed i.e. $(t_o)_{ToA}$ should be known. Similarly, in order to measure accurate ToFs, synchronization between each receiver is required i.e. $(t_o)_{ToF}$ should be known. Since this arrangement cannot always be fulfilled, the difference in the times of arrival (TDoA) between different receivers can be utilized to compute the object's location. Assuming the source started emitting at time: $(t_0)_{TDoA}$ and l^{th} receiver received the reflected burst at $(t_l)_{TDoA}$, $TDoA)l$ with respect to the first receiver can now be calculated as: $TDoA_l = ((t_l)_{TDoA} - (t_0)_{TDoA}) - ((t_1)_{TDoA} - (t_0)_{TDoA}) = ((t_l)_{TDoA} - (t_1)_{TDoA})$. The distance equations can now be written as:

$$d_{l,1} = d_l - d_1 = \sqrt{(x-x_l)^2 + (y-y_l)^2} \ - \ \sqrt{(x-x_1)^2 + (y-y_1)^2}, \ l = 2, 3, 4...L \tag{2.6}$$

$$TDoA_l = \frac{d_{l,1}}{c} => \ c \cdot TDoA_l = d_{l,1} = |\mathbf{x} - \mathbf{x}_l| - |\mathbf{x} - \mathbf{x}_1| => \begin{bmatrix} c \cdot TDoA_2 \\ c \cdot TDoA_3 \\ c \cdot TDoA_4 \\ . \\ . \\ c \cdot TDoA_L \end{bmatrix} = \begin{bmatrix} d_{2,1} \\ d_{3,1} \\ d_{4,1} \\ . \\ . \\ d_{L,1} \end{bmatrix} \tag{2.7}$$

$$\begin{bmatrix} c \cdot TDoA_2 \\ c \cdot TDoA_3 \\ c \cdot TDoA_4 \\ . \\ . \\ c \cdot TDoA_L \end{bmatrix} = \begin{bmatrix} d_{2,1} \\ d_{3,1} \\ d_{4,1} \\ . \\ . \\ d_{L,1} \end{bmatrix} + \begin{bmatrix} n_{TDoA,2} \\ n_{TDoA,3} \\ n_{TDoA,4} \\ . \\ . \\ n_{TDoA,L} \end{bmatrix} \tag{2.8}$$

$$=> \begin{bmatrix} c \cdot ((t_2)_{TDoA} - (t_1)_{TDoA}) \\ c \cdot ((t_3)_{TDoA} - (t_1)_{TDoA}) \\ c \cdot ((t_4)_{TDoA} - (t_1)_{TDoA}) \\ . \\ . \\ . \\ c \cdot (t_l)_{TDo.A} - (t_1)_{TDoA} \end{bmatrix} = \begin{bmatrix} \sqrt{(x-x_2)^2 + (y-y_2)^2} \ - \ \sqrt{(x-x_1)^2 + (y-y_1)^2} \\ \sqrt{(x-x_3)^2 + (y-y_3)^2} \ - \ \sqrt{(x-x_1)^2 + (y-y_1)^2} \\ \sqrt{(x-x_4)^2 + (y-y_4)^2} \ - \ \sqrt{(x-x_1)^2 + (y-y_1)^2} \\ . \\ . \\ \sqrt{(x-x_l)^2 + (y-y_l)^2} \ - \ \sqrt{(x-x_1)^2 + (y-y_1)^2} \end{bmatrix} + \begin{bmatrix} n_{TDoA,2} \\ n_{TDoA,3} \\ n_{TDoA,4} \\ . \\ . \\ n_{TDoA,L} \end{bmatrix} \tag{2.9}$$

Go to ToC

where $TDoA_l$ = measured TDoA for l^{th} receiver and $n_{TDoA,l}$ = measurement errors for TDoA.

Equations 2.3, 2.5 & 2.9 show a nonlinear relationship between the location of the implant ($\mathbf{x} = [x\ y]^T$) and the corresponding measurable time instants t_l. The measurement noise (n) includes inhomogeneity in the medium, offsets in the measuring devices and also in-accuracy in the measuring techniques. These equations can be solved for **x** using linear approaches (Linear Least Squares (LLS), Maximum Likelihood estimators(ML)) or non-linear approaches (Non-Linear Least Square (NLS), Weighted Linear Least Squares (WLLS)) [43].

In [44], three channels of an external ultrasound probe is used to generate ultrasound bursts that travel towards and reflect back from a piezo element (implant). The received signals at these three channels are cross-correlated with a reference channel to measure TDoAs. The distance equations are formulated. A cost function is defined based on measured ToAs, the position of the individual elements of the external probe and the unknown location of the implant. An iterative steepest descent algorithm is used to minimize this cost function in order to increase the accuracy of the implant location i.e. non-linear optimization of the distance equations is performed. In [46], an ultrasound emitter is placed inside a glycerin medium surrounded by a water medium. Three receivers are placed in this water medium. ToFs are measured using cross-correlation between the emitted burst signal and the received burst signal. These ToFs along with the speed of the ultrasound are used to derive an expression for the shape of the wavefront produced by the ultrasound emitter. The propagation path of the ultrasound wavefront is divided into finite elements. The expression for the shape of the wavefront is then derived by connecting all the elements with the same pressure amplitude. By the principle of reciprocity [52], the receivers would also produce the identical wavefront when driven as emitters. Accordingly, the emitter location is estimated as the intersection of the three wavefronts produced by the three receivers.

2.2.2. Beam-forming methods

Delay-Sum Beamforming (DSB)

Consider four ultrasound transducers (receivers) placed in front of two ultrasound emitters: source 1 and source 2 as shown in Fig 2.1. The burst received by the four transducers from source 1 is shown in red (denoted by $f_{1,1}(\mathbf{x},t)$, $f_{1,2}(\mathbf{x},t)$, $f_{1,3}(\mathbf{x},t)$, $f_{1,4}(\mathbf{x},t)$) and burst received from source 2 (denoted by $f_{2,1}(\mathbf{x},t)$, $f_{2,2}(\mathbf{x},t)$, $f_{2,3}(\mathbf{x},t)$, $f_{2,4}(\mathbf{x},t)$) is shown in blue. Each of the four receivers captures these ultrasound burst signals at different instants of time i.e. the received signals have different time delays with respect to each other (Step 1). The delays associated with the ultrasound burst originating from source 1 are denoted by Δ_1, Δ_2, Δ_3, Δ_4. When these delays associated with source 1 are added to the original signals from both source 1 and source 2, it can be seen that the delayed signals from source 1 are now in phase with each other. On the other hand, the delayed signals received from source 2 are further out of phase with each other (Step 2). Moving further, these delayed signals are multiplied with a certain weight (gain) and summed to generate a single signal component. It can be seen that the delayed and summed signal from source 1 has a greater amplitude than that of source 2 (Step 3). This signal is further normalized to generate the signal $f_{BF}(\mathbf{x},t)$, which is defined by the following equations:

$$f_1(\mathbf{x},t) = w1 \cdot f_{1,1}(\mathbf{x}, t+\Delta_1) + w2 \cdot f_{1,2}(\mathbf{x}, t+\Delta_2) + w1 \cdot f_{1,3}(\mathbf{x}, t+\Delta_3) + w1 \cdot f_{1,4}(\mathbf{x}, t+\Delta_4) \quad (2.10)$$

$$f_2(\mathbf{x},t) = w1 \cdot f_{2,1}(\mathbf{x}, t+\Delta_1) + w2 \cdot f_{2,2}(\mathbf{x}, t+\Delta_2) + w1 \cdot f_{2,3}(\mathbf{x}, t+\Delta_3) + w1 \cdot f_{2,4}(\mathbf{x}, t+\Delta_4) \quad (2.11)$$

$$f_{BF}(\mathbf{x},t) = \frac{f_1(\mathbf{x},t) + f_2(\mathbf{x},t)}{M} \quad (2.12)$$

where $w1$, $w2$, $w3$, $w4$ are the weights/gain of the four transducers; Δ_1, Δ_2, Δ_3, Δ_4 are the delays associated with the burst signal received by the four transducers; and M is the sum of the weights used to normalize the delayed and summed signal.

Since this set of delays (Δ_1, Δ_2, Δ_3, Δ_4) is generated from the burst corresponding to source 1, the receiver's sensitivity is maximized to the burst propagating in this direction [53]. By adjusting this set of delays, the receiver's sensitivity can be increased in a particular direction. This principle is used in ultrasound imaging [54]. By continuously adjusting the delay set, the receiver's sensitivity is changed to sense ultrasound bursts in a particular direction each time. By sensing in a particular direction every time, a Region of Interest (RoI) can be scanned. In the presence of an ultrasound emitter or a specular reflector [55], the processed delayed and summed signal shows a high amplitude, as shown in Fig 2.1 (Step 4). Upon scanning the RoI, every focused point is represented by the amplitude of this delayed

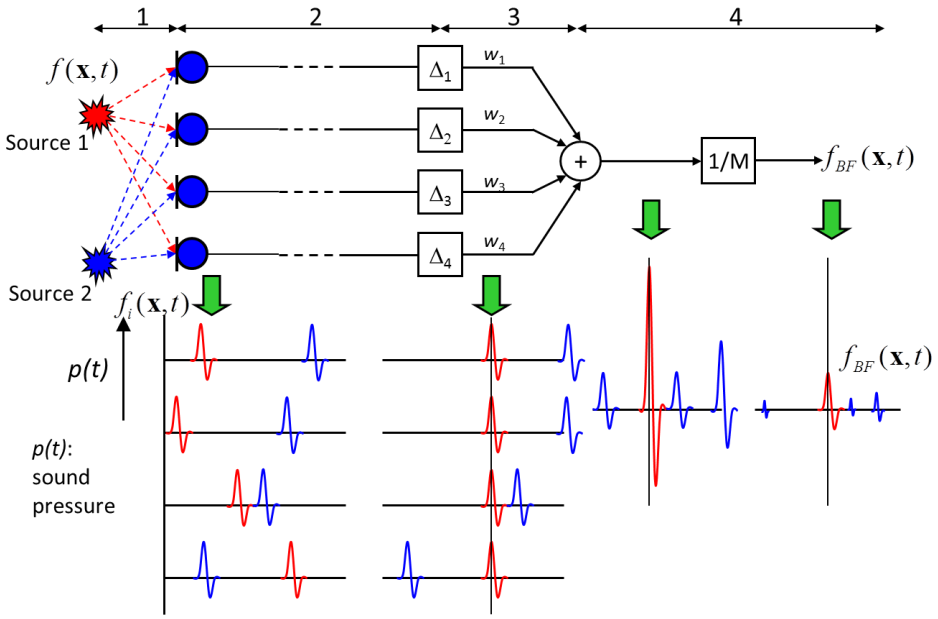

Figure 2.1: Delay and Sum beamforming [56]. Step 1 - signal reception, Step 2 - delay estimation, Step 3 - Summation of the delayed signals, Step 4 - Normalizing of the summed signal.

and summed signal. Hence a contrast image is generated which shows these reflectors/emitters with a bright light. This is called B-mode image [22].

Delay-Variance Beamforming (DVB)

Since conventional ultrasound imaging has limits when it comes to distinguishing small implants from larger specular reflectors, further image processing is required in order to track implants using ultrasound imaging. One of the ways to improve this further processing can be achieved by implementing Delay Variance Beamforming [53]. As shown in figure 2.1, the weights (w_1, w_2, w_3, w_4) are fixed in Delay-Sum Beamforming. These weights can be adjusted for every burst signal such that the variance of the output signal $f_{BF}(\mathbf{x},t)$ is minimized [53]. The variance (σ^2_{BF}) is given by:

$$\sigma^2_{BF}(w_1,w_2,w_3,w_4) = \frac{\sum_{n=1}^{2}\sum_{k=1}^{4}(f_{BF}(t)-f_{n,k}(t))^2}{8} \tag{2.13}$$

By solving Equation 2.13 for w_1, w_2, w_3, w_4 such that σ^2_{BF} is minimum, it is possible to find the set of weights which does not distort the sensitivity in the desired direction while suppressing the impact from the signals originating from other directions [53].

In [47], the position and orientation of a metallic needle are detected from B-mode images that are further processed. The metallic needle is surrounded by a foam phantom and a conventional ultrasound probe is used for image acquisition. This desired further processing is achieved by using Delay-Variance Beamforming and tuning the parameters of a Frangi multiscale vesselness filter. Combining these two methods drastically increased the contrast in the B-mode image such that the needle is distinguishable from its surroundings. Consequently, the position and the orientation of a metallic needle are ascertained along with real-time tracking of the needle movement. Although the position and the orientation are detected accurately, the tuning of the filter is position and angle dependent. Every time there is a change in the orientation or the position of the needle, new parameters are needed to be tuned visually. The orientation detection is again dependent on the size of the aperture and the distance between the metallic needle and the probe [47].

Time/Phase Reversal

Imagine a phased array of ultrasound transducers (Fig 2.2). Focusing of ultrasound waves using this array is performed by providing time delays to each element of the array. These individual time delays bear a relationship with each other as shown below [57]:

Go to ToC

$$\Delta t_n = n \cdot \frac{d}{c} \cdot sin(\theta) + t_0; \quad \Delta t_n = \frac{F}{c} \cdot (1 - \sqrt{[1 + (\frac{nd}{F})^2 - 2 \cdot \frac{nd}{F} \cdot sin(\theta)]}) + t_0 \tag{2.14}$$

Here, Δt_n is the delay for n^{th} element, c is the speed of ultrasound waves, F is the focus depth, d is the distance between two consecutive elements, θ is the steering angle and t_0 is the offset delay to make sure Δt_n is positive. The first equation shows a linear relationship and the second equation shows a 2nd order (elliptical) relationship between individual time delays i.e. between Δt_n & n.

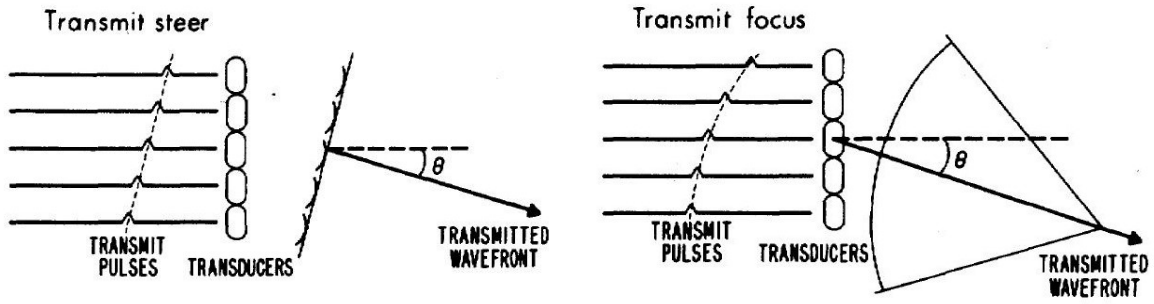

Figure 2.2: Beam steering and focusing using a phased array of ultrasound emitters [57].

Figure 2.2 demonstrates how delays applied to individual elements can steer the ultrasound beam and focus it at the desired point. It can be seen that when the delays are linearly varied, a plane wave is generated in the desired direction. When the delays are varied in an elliptical fashion the ultrasound beam gets focused on a single point. This is due to the constructive interference of the individual wave-fronts i.e. the maxima of each wave-front get added together to produce a much larger intensity at this point.

By the principle of reciprocity [52], when a phased array of ultrasound transducers receive ultrasound waves from a point source or in the form of a plane wave, each element of the array, senses this beam at different instants in time, identical to the elliptical or linear fashion of delays respectively (as mentioned previously). Thus as long as the delays associated with the received ultrasound waves are known, the location of the source can be estimated. If the measured delays bear a linear relationship, then the target is relatively big and located in the direction of θ. If the delays bear an elliptical relationship, then the waves come from a very small source located at distance F (focus depth) in the direction of θ (focus steer).

Time/phase reversal utilizes this principle of reciprocity to locate the bio-medical implant. Time reversal involves simply inverting the measured time delays and applying them to the individual transducers. Phase reversal, very similar to time reversal, involves measuring the delay difference between one transducer element and a reference element on this phased array. This delay is again inverted and applied to the elements with a delay of zero to the reference element. After applying the above mentioned inverted delays to each element, the phased array now focuses the ultrasound waves on the object from which the waves were originally generated, hence locating the object [51]. Figure 2.3 illustrates how Time Reversal Beamforming can be implemented in three steps. Initial powering of the implant provides the power required to produce an ultrasound 'ping' which is received by the phased array. After receiving this 'ping' the delays are reversed and applied to the individual elements of the phased array to focus the ultrasound beam on the implant. This principle primarily depends only on the accuracy of measured delays. Hence it can be utilized to develop robust and simple tracking methods.

In [50], an experimental setup is used to power a 0.8 mm piezo cube (implant) using a custom made 2-D phased ultrasound array. Both the array and the implant are submerged in the canola oil which mimics the acoustic properties of the tissue. Using Time and Phase Reversal beamforming, the custom ultrasound array is able to focus on the sub-mm^3 piezo element, thus harvesting the power equal to that achieved during the simulation of the setup. Time/Phase Reversal Beamforming is also compared with Delay-Sum beamforming in this work and it is concluded that the former method shows around 20% more efficiency in powering the piezo element, in other words more accurately locating and focusing ultrasound beam on the small sized implant

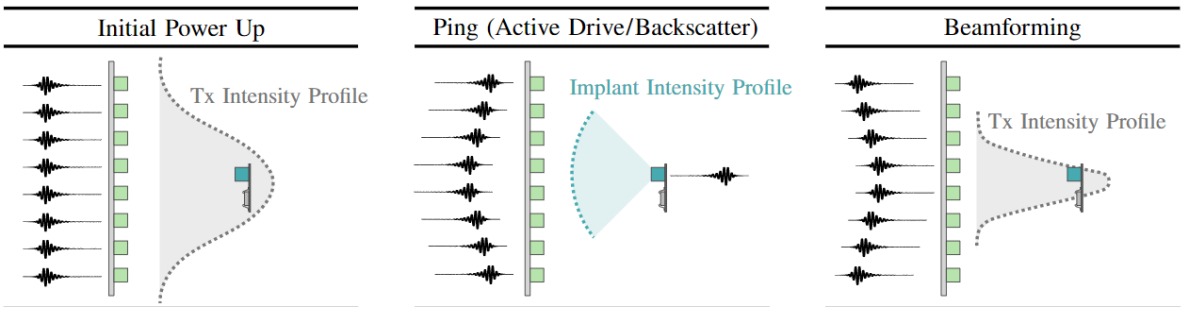

Figure 2.3: Illustration of Time Reversal Beamforming [50].

2.3. Inference from the review

As stated earlier, passive tracking is beneficial from a biomedical perspective. In this regard, the passive tracking methods discussed above utilize the principle of triangulation with the use of 3 or more receivers. The above mentioned time/phase reversal can be slightly modified to implement a passive tracking method that does not require this spatial positioning of receivers. This involves the use of a phased array (probe) to generate ultrasound waves which first travel from the phased array to the implant and gets reflected back to the array. The delays associated with the reflected waves from the object are measured at the array's end to ascertain the implant's location. Furthermore, the time/phase reversal method offers:

1. Robust tracking: as the method primarily depends only on the measurement accuracy of the delay. An accurate wave-front delay measuring system can robustly track the implant.
2. Computational simplicity: After measuring the delays, no linear equation solving is required in contrast to the other passive tracking methods. Inverting the delays requires very small computation power. Hence a simpler algorithm and a less complicated hardware can be built for tracking.
3. Inherent immunity from tissue in-homogeneity and scattering [51]: The tissue spread across the whole human body is not homogeneous in its composition. This implies ultrasound wave speed changes during its time of flight along with uneven scattering of ultrasound bursts. Since both of these effects are already accounted in the measured delays, time/phase reversal method is not influenced by these factors.

With such benefits associated with time/phase reversal technique, it is chosen as the tracking principle for this work. Further improvement to this principle is also performed, which is discussed in the later Sections (Section 2.8) of the report. The tracking algorithm that is developed in this work is an extension of the research work previously performed in Philips Research, Eindhoven - [21], [23], [58]. The highlights of the previous work are the experimental setup, up-link telemetry protocol and a heat map. These topics are discussed further in the report along with the tracking algorithm and the experimental results obtained.

2.4. Experimental Setup

The key components of the setup are: L7-4 Philips ultrasound probe, CMUTs mounted on a PCB, tissue phantom and up-link telemetry circuit (Fig. 2.4). The probe consists of 128 channels of PZT elements capable of producing ultrasound waves from 4 MHz to 7 MHz. This probe is placed on a linear translatory stage which is controlled by Newport ESP300 universal motion controller. The probe is moved towards or away from the CMUTs using this stage. The 2-D array of pre-charged collapsed mode CMUTs as mentioned in section 1.2.1 is used as a receiver for the ultrasound waves generated from the probe. The CMUTs are mounted on a PCB with connectors to measure the output voltage signal recorded by the CMUTs. This PCB is positioned on a rotational stage controlled by an ESP300 motion controller. This allows to orient the CMUT array either with an angle or parallel to the face of the probe. The CMUT array and the probe must face each other parallelly in order to harvest the highest amount of transmitted ultrasound power [21]. Both the linear and rotary stages have micro-manipulators that displace the CMUT PCB or the probe in the order of tens of micrometers to help with the alignment. The phantom is made of candle gel (95% paraffin oil and 5% organic constituents), which mimics the

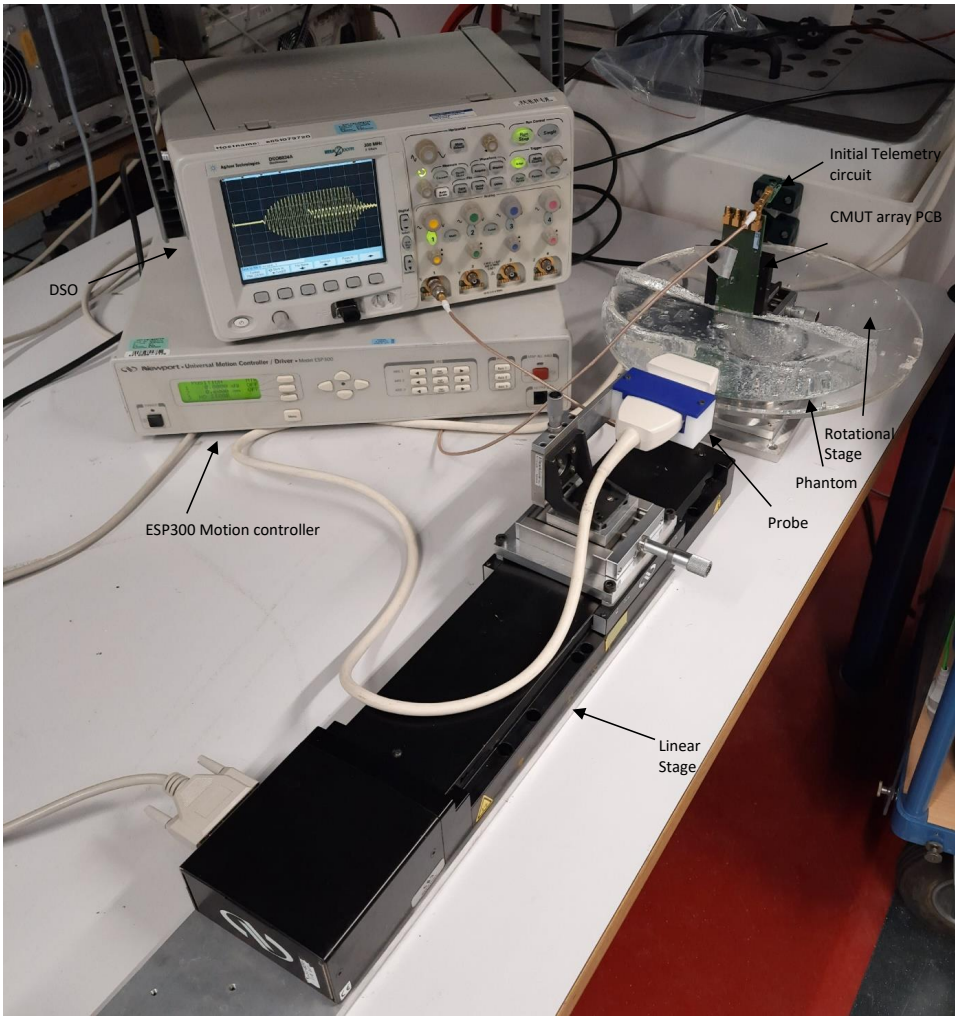

Figure 2.4: Experimental setup

characteristics (sound speed and attenuation[21]) of human tissue. Ultrasound waves are generated by the ultrasound probe. They travel through the phantom and reach the CMUT array.

2.5. Reflection Coefficient and Back-scattering

Acoustic waves get reflected and partially transmitted when they encounter a change in medium. The fraction of energy reflected and transmitted through, are given as follows [19]:

$$R = \frac{p_R}{p_I} = \frac{Z_2 - Z_1}{Z_1 + Z_2} \quad T = \frac{p_T}{p_I} = \frac{2 \cdot Z_2}{Z_1 + Z_2} \tag{2.15}$$

where the acoustic waves are traveling from medium 1 to medium 2. p_R, p_T & p_I are the reflected, transmitted and incident pressures. Z_1 and Z_2 are the acoustic impedances of mediums 1 and 2.

Initial telemetry involves communicating a desired parameter of the implant to the outside world. Ultrasound bursts are sent toward the implant. The reflection coefficient changes proportional to this desired parameter. These variations in the reflection coefficient of the receiver change the amount of reflected energy and that can be measured back at the source. This change is then detected and decoded to obtain the desired parameter. This is the principle of backscattering and is shown in Fig. 2.5. In this work, this change in the reflection coefficient is caused by modulating a load connected to the CMUT. When the switch is open, the CMUT is connected to an optimal load, and it harvests most of the incoming ultrasound energy with a small amount of it being reflected back. When the switch is closed, the CMUT is no longer connected to an optimal load, hence most of the incident energy is

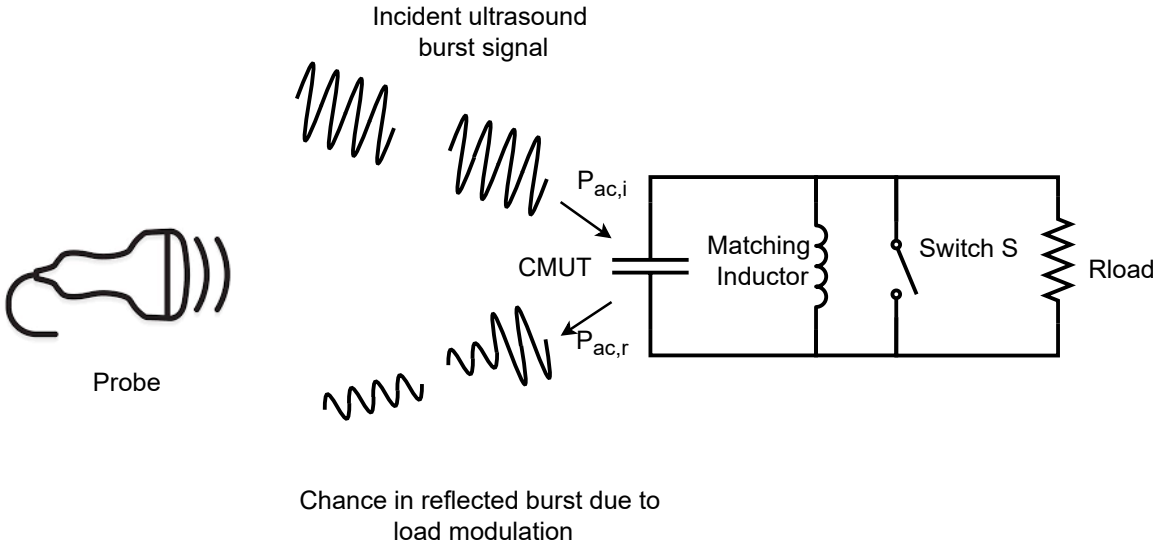

Figure 2.5: Principle of Back-scattering.

reflected back and less is harvested.

2.6. Load Impedance Modulation & Initial Telemetry

The encoding of the desired parameter is done by controlling the switch S (see Fig. 2.6). This is called load impedance modulation. This figure shows the schematic representation of the initial telemetry circuit. For the initial telemetry, the voltage of a storage capacitor is selected as the desired parameter to communicate. A circuit was previously developed at Philips Research, Eindhoven [23] which transmits the level of the storage capacitor voltage every 2 msec.

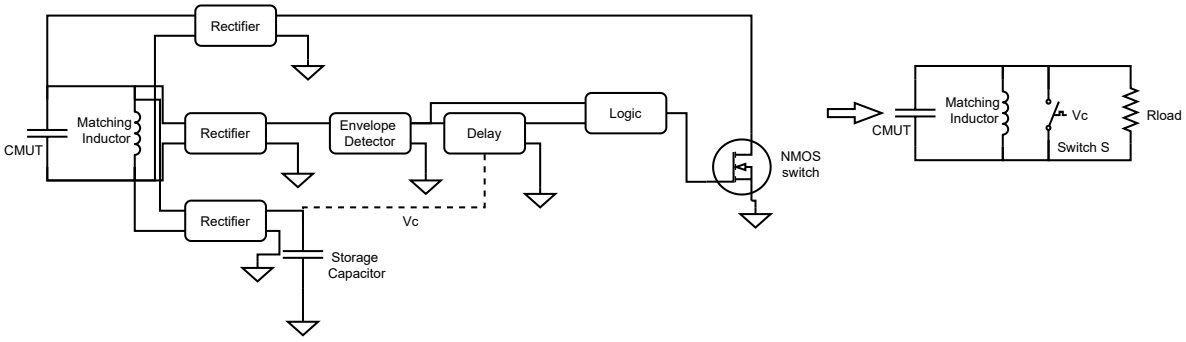

Figure 2.6: Schematic diagram of initial telemetry circuit.

The probe connected to the Verasonics system is programmed to generate 24-cycle 4 MHz sinusoidal acoustic waves, with a pulse repetition frequency of 1 kHz. The important components of this circuit are: the matching inductor, envelope detector, delay element and the NMOS. The matching inductor is used for compensating the CMUT's capacitive impedance (Sec 1.2.2). The CMUT transduces these acoustic waves into electrical signals. After rectifying the waves, the envelope of the burst is detected by the envelope detector. The envelope is delayed with a delay (by the delay element) directly proportional to the voltage level of the storage capacitor (Vc) i.e. the desired parameter. The logic block drives the NMOS switch in such a way that it shorts the CMUTs for the amount of time equal to the delay (produced by the delay block) for every second burst. Hence the switch S is controlled by Vc which either opens or shorts the CMUT. This is how load impedance modulation is achieved (please refer [23] for further information).

Figure 2.7 illustrates the PWM protocol which uses back-scattering and load impedance modulation to transmit the voltage level of the storage capacitor from the CMUT to the outside world (Verasonics

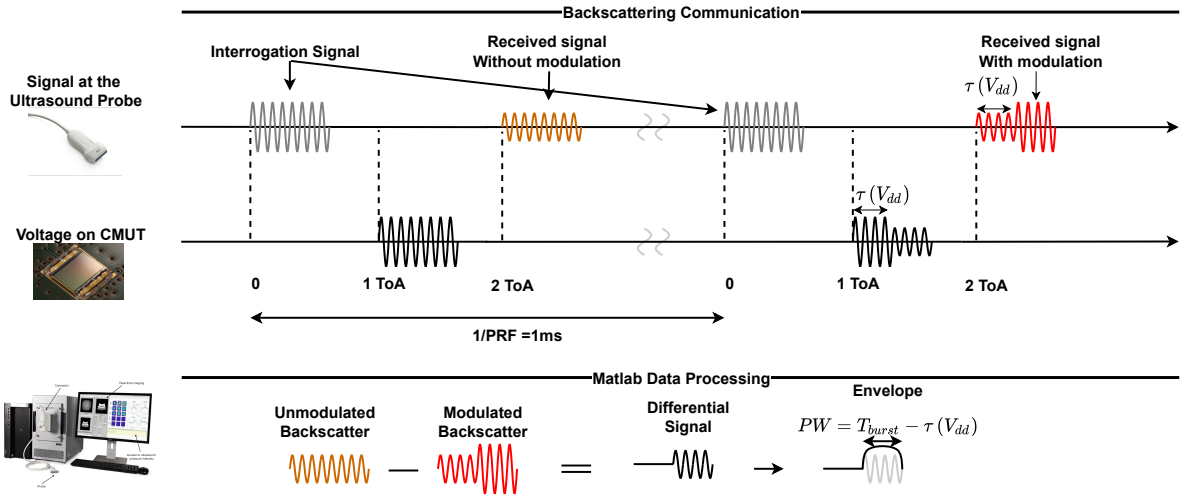

Figure 2.7: PWM protocol based on load impedance modulation and back-scattering (courtesy I.Subramaniam)

system). The protocol starts with the probe generating the 24-cycle burst. After one ToA, the acoustic waves reach the CMUT device, and the storage capacitor is charged. The rest of the energy is reflected back and it is detected by the probe after two ToAs. For the second burst, after one ToA, the switch is closed and the CMUT gets shorted for a duration proportional to the voltage level of the storage capacitor (see fig 2.7). When the CMUT gets shorted, most of the incoming energy is reflected back and it can be detected at the probe side, after 2 ToAs. At the Verasonics end, the modulated and the un-modulated waves are subtracted from each other and the width of the difference contains the encoded value of the storage capacitor voltage level.

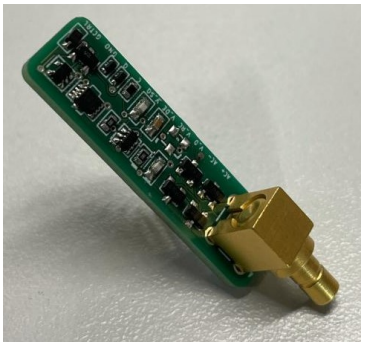

Figure 2.8: Initial (up-link data) telemetry circuit [23].

2.7. Heat Map

The PWM protocol used in the initial telemetry circuit provides information of the voltage level of the storage capacitor in an implant. The storage capacitor gets charged when sufficient acoustic energy reaches the CMUT surface. Without the convenience of focusing of acoustic beams (similar to RF power transfer), power transfer would require very high input power (electrical/acoustic). Hence the challenge is to focus the ultrasound beams on the CMUT, whose size is in order of several mm^2.

In [23], the above mentioned initial telemetry circuit (see Fig. 2.8) is utilized to generate a heat map that displays the voltage level of the storage capacitor when the ultrasound beams are focused at each coordinate point in the map. Figure 2.9 shows the coordinate system used in the heat map. The red rectangle in the figure is the Region of Interest (RoI). The focusing of the ultrasound beam starts at (y,z) = (-2 mm,80 mm) i.e. left bottom corner of RoI. The scan progresses by increasing the depth (z) and reducing the x to cover the whole system with the last point being (y,z) = (+2 mm,150 mm) i.e. the right top corner.

Go to ToC

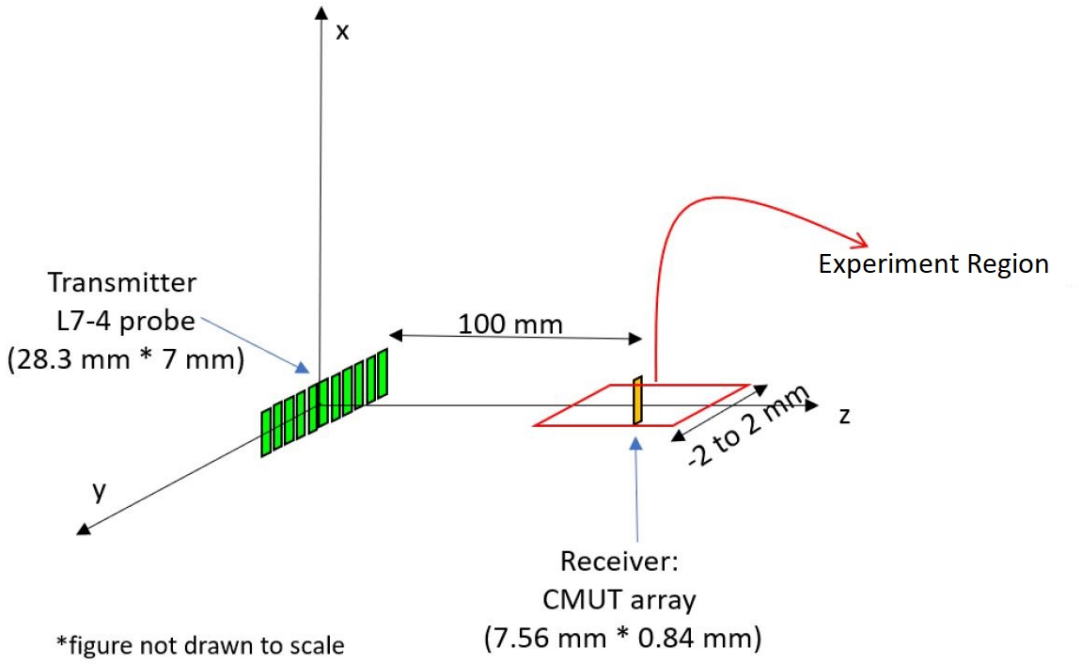

Figure 2.9: Coordinate system representing the probe and CMUT PCB placement [23].

Figure 2.10 shows the two consecutive bursts of which one burst is modulated (Fig. 2.10b). The storage capacitor starts storing energy when the ultrasound beam reaches the CMUTs. When the focused coordinate point is near the CMUT region then we see a longer modulated pulse width. Hence, this modulated width of the second pulse varies for each coordinate point. As discussed in Section 2.6, this pulse width is directly related to the voltage level of the storage capacitor. The heat map (Fig. 2.11) plots this pulse width corresponding to each coordinate point.

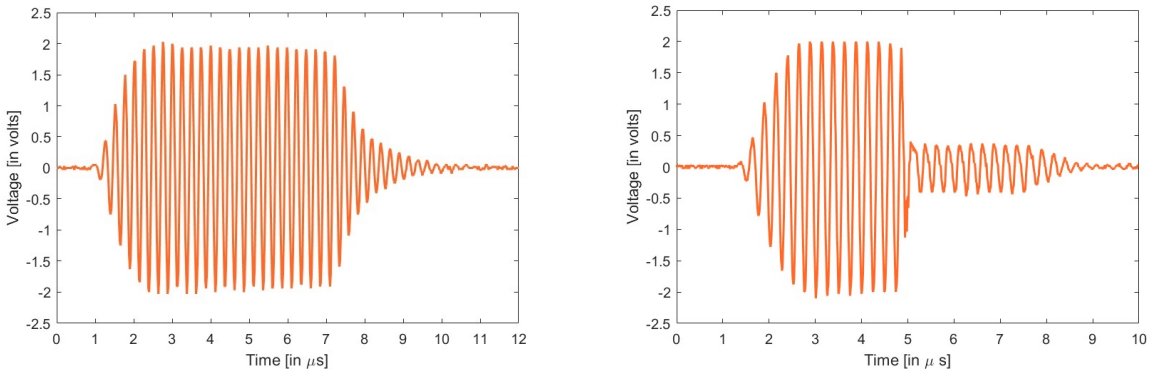

(a) Voltage level measured at CMUT (unmodulated signal) [23].

(b) Voltage level measured at CMUT (modulated signal) [23].

Figure 2.10: CMUT voltage levels.

In previous research [21], it was observed that maximum power is transferred when the ultrasound beam incidents the CMUT almost perpendicular to its surface. Following this, the CMUT is placed in front of the probe center. The heat map (Fig. 2.11) also follows this observation, as it can be seen that the maximum power transfer coordinate or the hot-spot is (y,z) = (0.07 mm, 100.74 mm) i.e. the ultrasound beam is made to incident perpendicular to the CMUT surface. The -3dB width (half-power beam width) was observed to be 1.05 mm in the y direction and 8mm in the z direction i.e. the yellow region in the figure. It is therefore essential that the ultrasound beam is focused only in this region to ensure maximum power transfer. The hot-spot (intersection of (a) & (b) lines) and the half power beam width is found by scanning the whole region around the CMUT.

Go to ToC

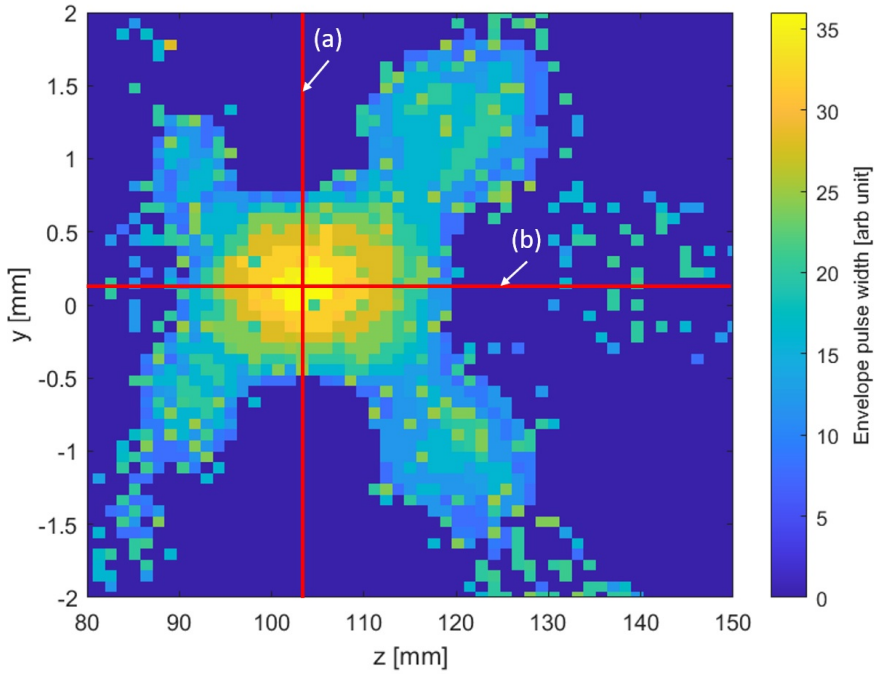

Figure 2.11: Heat map displaying the pulse width of the received ultrasound burst upon focusing the bursts at all points of coordinate-system [23]. Lines (a) & (b) intersect at the coordinate point enabling maximum power transfer.

The above mentioned hot-spot is tracked by scanning the whole coordinate system. The total scanning time for the whole coordinate system is more than 3 minutes, which also implies that the hot-spot can only be tracked every 3 minutes. Additionally, the setup does not move in space and hence heat map is always valid. However, it may happen that during the scanning, the device may move if it is present inside a human body. Assuming that the implant is near the chest surface of a human body, the implant can movements can range between 4 to 12 mm with a frequency of 0.2–0.34 Hz (12–20 breaths per minute) due the lung movement during breathing. Additionally, the implant position can be affected by the weaker vibrations of the heart ranging from 0.2–0.5 mm and a frequency range of 1–1.34 Hz (60–80 beats per minute) [59], [60]. Although the dimensions of the movement and the frequency appear small, it shows a drastic change in the power transfer efficiency when the implant is a few mm^2 in size. The lateral dimension of the hot-spot region shown in Fig 2.11 is also the beamwidth of the ultrasound probe focusing on the implant. This beamwidth is evidently only a few mm wide. As mentioned in Section 1.1, previous research has shown that the power received by the implants can reduce by 70 % when there is 0.5° shift in the focused ultrasound beam i.e. about a 1 mm shift from the implant's location in the lateral direction of the beam's axis [21]. Therefore any small breathing or heart movements can move the implant very far from the focus region of the ultrasound probe. This would ultimately shift the maximum power transfer point and render the scan not valid. It is therefore required to change the focus point of the ultrasound probe when there is a small movement. Scanning the RoI to track the hot-spot is arduous and can fail at times when there is frequent movement in the human body. Alternatively, the time/phase reversal method offers a faster and more direct approach that can track the implant when there is a constant change in the position of the implant.

With Section 2.2.2 in the back of the mind, the reflected burst in the back-scattering principle arrives at the 128 channels of the probe, at different instants of time i.e. each channel has a delay with respect to the other. With the initial telemetry circuit in place, both the modulated and un-modulated signals arrive at the 128 channels at different instants in time. These delays can be reversed to focus back on the reflected surface.

There are three reflecting surfaces transmitting back these bursts: 1. PCB holding the CMUT, 2. non-modulating CMUT drums region and 3. the modulating CMUT drums region which is connected to the initial telemetry circuit (also the desired region in tracking). It is therefore important to ascertain

whether or not the reflected bursts are being received after reflecting at the region of the modulating drums or not. The modulated width is obtained by subtracting successive un-modulated and modulated signals (see Fig. 2.7). This modulated width cannot be obtained when the bursts are reflected at either the PCB or the non-modulating CMUT drums region. Furthermore, these modulated widths, very similar to reflected bursts in back-scattering, arrive at the 128 channels of the probe at different time instants. Hence by measuring and reversing the delays associated with these modulated widths, it would be possible to make the channels of the probe focus the ultrasound beam on the modulating CMUT drums region.

2.8. Tracking Algorithm

The tracking algorithm developed in this work involves the time/phase reversal method along with load modulation and back-scattering. Back-scattering and load modulation add a passive tracking trait to this method. First, ultrasound bursts generated at the probe travel toward the CMUT array. The CMUT array reflects back these bursts towards the probe, eliminating the need to actively drive the CMUTs in transmitting mode i.e. back-scattering. The CMUTs will now modulate the width of every second burst as discussed in the previous sections i.e. load modulation. The delays associated with the modulated widths originate from the modulating CMUT region and are received by the 128 channels of the probe, giving information about the modulating CMUT region (refer Section 2.2.2). These delays are then reversed and the ultrasound beam will directly focus on the modulating CMUT region.
To start with the tracking, a region of interest must be defined. In this work, this region of interest is called the coordinate system. The coordinate system can be obtained using B-mode imaging. A B-mode image looks very similar to a negative of a photograph. The bright region in the image represents the intensities of the ultrasound reflections from surfaces where there is a sudden change in the acoustic impedance [22]. Ultrasound waves get reflected at surfaces where there is a mismatch in the acoustic impedance, as discussed in Section 2.5. Such surfaces are formed due to the presence of organs or other objects like biomedical implants. Effectively the B-mode image shows an approximate region of the implant surrounded by the internal organs i.e. the coordinate system we require. Simultaneously, the probe can be brought into the plane of the implant to enable the focusing of the ultrasound beam on the CMUTs.

Initially, the boundaries of the coordinate system (as shown in Fig. 2.9) and the ultrasound burst parameters: burst frequency, pulse repetition frequency, burst amplitude and the number of cycles in each ultrasound burst, are defined. The scanning of the coordinate system starts from the first coordinate point. Two ultrasound bursts are sent to the focus point to check for pulse width modulation in the reflected bursts. In case no modulation is observed, the bursts are focused on the next point in the system. In case load modulation is observed, the delays associated with the modulated pulse widths seen by all 128 channels are measured. These delays are measured using a cross-correlation technique (in MATLAB) [61].

$$R_{xy}(\tau) = \int_{-\infty}^{\infty} x(t) \cdot y^*(t-\tau)dt \tag{2.16}$$

Cross-correlation of two signals ($x(t)$, $y(t)$) gives a measure of the similarity between the signals, as its output ($R_{xy}(\tau)$). The output of cross-correlation is a function of τ. Considering the delay between the two signals equal to zero, in case the two signals are very similar, the integral (R_{xy}) sums up to a high value and in case there is no similarity, the integral sums up to a very low value, both at $\tau = 0$. It is considered that the two signals are very similar as we are sending bursts with the same parameters every time. Accordingly, we will find a high value (peak) in the ($R_{xy}(\tau)$) function at $\tau =$ delay between the two signals. Finding the location of this peak gives us the delay i.e. the output of cross-correlation of two signals gives the delay between the signals as its output.

The delay of each modulated pulse width is measured with respect to a reference channel (reference modulated pulse width) i.e. the phase reversal technique is implemented. Often these measured delays have rather big errors. This is highly undesirable. Ideally, the time delays associated with each channel must follow a 2nd order relationship (as discussed in Section 2.2.2) in order to focus at a single point. Accordingly, this knowledge can be used to utilize the measured delays even in the presence of error. Curve-fitting or 2nd order regression analysis can be used to derive a relationship similar to eq. 2.14) using these delays. This relation in turn produces the delays required for the channels to focus at a

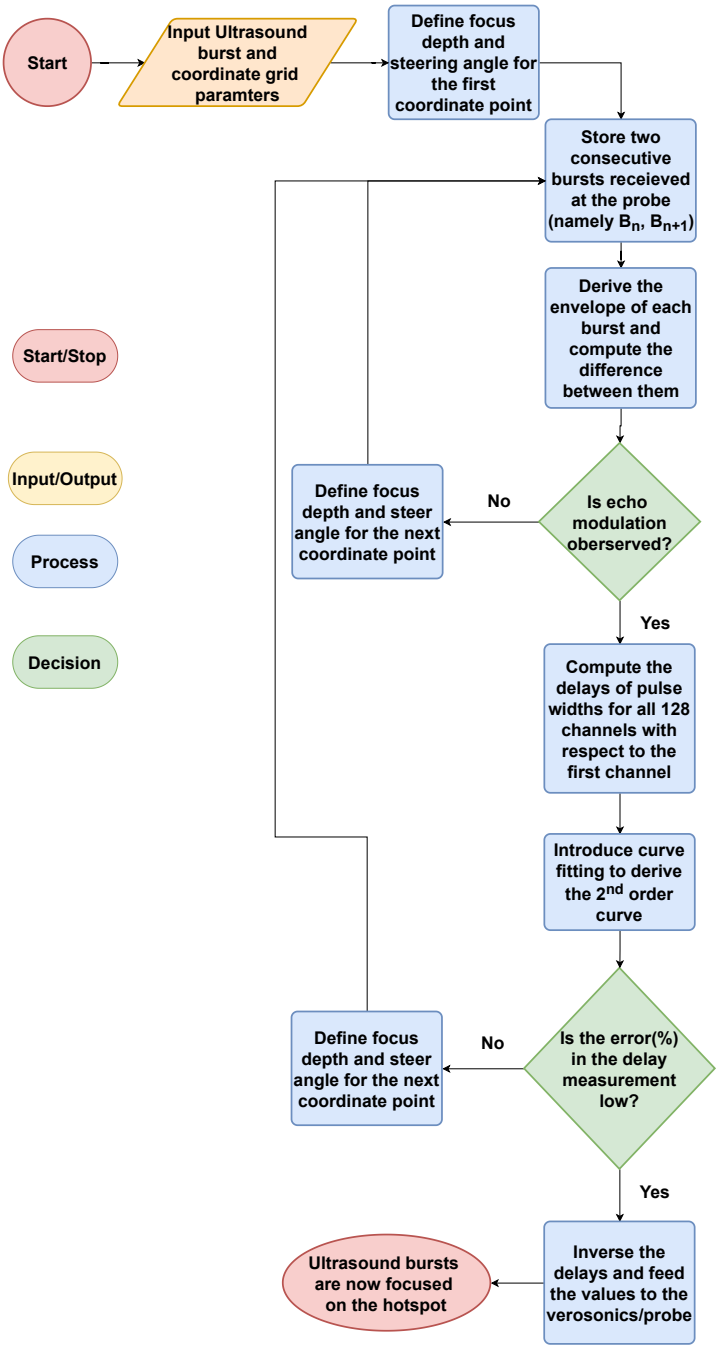

Figure 2.12: Tracking Algorithm.

single point since they follow a 2nd order relationship. Using the same derived relationship, the error percentage in the measured delays can be estimated. The estimated delays and the error percentage in the measured delays are further discussed in Section 2.9.

In case the error percentage is high (more than 8% when compared with the derived relationship), the measured delays are discarded and the focus point is shifted to the next coordinate point to measure modulation once again. In case the error percentage is low (less than 8%), the estimated delays are inverted and fed as inputs to each channel of the probe. This focuses the ultrasound bursts at the active CMUT region. Figure 2.12 illustrates the above discussion in the form of a flowchart.

2.9. Experimental Results & Discussion

Figure 2.13 shows a pictorial illustration of the coordinate system considered for the experiment. The origin is at the center of the probe and the region of interest (RoI) extends from $70mm$ to $110mm$ in $+z$ direction (focus depth) and from $-2mm$ to $2mm$ in x direction (focus steer). Scanning is made to start at $(x, z) = (-2mm, 70mm)$ i.e. bottom left corner. This starting point is to compare how quickly the tracking algorithm can reach the hot-spot.

First, the rigorous way of scanning the whole coordinate system to find the hot-spot is performed. Figure 2.14a shows the heat map (in [23]) that is reconstructed for the new coordinate system. Once again lines (a) and (b) intersect at the hot-spot, which is situated at $(x, z) = (0mm, 87.78mm)$. Next, the tracking algorithm is implemented with the same starting point and scanning path (previously mentioned in section 2.7). Figure 2.14b shows the hot-spot (red dot) tracked by the algorithm at $(x, z) = (-0.069mm, 86.55mm)$. The modulation is first observed near the first coordinate point ($(x, z) = (0mm, 87.78mm)$), also seen in the heat map (Fig. 2.14a). At $(x, z) = (-1.72mm, 75.51mm)$ i.e. almost bottom-left corner, the measured modulated delays were seen to contain a low error percentage. Following this, the estimated delays were inverted and fed to the probe. The focus point, immediately shifted from $(x, z) = (-1.72mm, 75.51mm)$ (blue-dot) to $(x, z) = (-0.069mm, 86.55mm)$ (red-dot).

Figure 2.15 shows the voltage level measured at CMUT at the hot-spot. The figure shows two consecutive bursts i.e. the first un-modulated and its consecutive modulated burst. Figure 2.16a shows the recorded phases of each channel at the coordinate point $(x, z) = (-1.72mm, 75.51mm)$. The blue dots in the figure represent the delays measured using cross-correlation. It can be seen that the measured delays contain some errors, which are highlighted in the figure. These errors were observed to be random and affect all the channels. The following reasons are held accountable for these errors based on some debugging:

1. The processing time of the verasonics software sequencer (Section 1.2.4). In order to maintain a particular Pulse Repetition Frequency (PRF) (of 500 Hz in this case), the hardware and the software sequencer are not run in sync with each other. The hardware sequencer often performs transmission and acquisition events quite quickly. Whereas delay measurements for 128 channels and 2nd order curve fitting performed by the software sequencer are time consuming. Therefore at high PRF ($\geq$ 1 kHz) the hardware acquisition and DMA transfer of the recorded data is faster than the software sequencer's processor. At high PRFs, it is observed that often the software sequencer is computing on the data acquired from two different focus points since multiple channels data is seen to be drastically out of phase as seen in Appendix A. Lowering the PRF below 1 kHz has been seen to be beneficial as the hardware sequencer is now much slower.
2. The recording electronics of the verasonics contain a Time Gain Control (TGC) amplifier and a 14-bit ADC. The maximum sampling frequency that could be achieved using the verasonics system is four times the burst frequency. This implies the reflected burst seen by the probe contains 4 samples of the signal amplitude for every wavelength. It is observed that the peaks of the burst waveform are commonly missed during the sampling. These missed peaks result in the shift of the location of the maximum cross-correlation discussed in Section 2.8. This shift is about a few wavelengths, hence the error in the delay measurements.
3. Non-uniform acoustic coupling between the probe and gel-phantom adds further arbitrary delays to the wave-fronts seen by each channel. It is observed that when the coupling gel contained air bubbles the delay measurement are often erroneous which could have been caused due to diffraction caused by these bubbles.

A typical delay pattern (generated by the verasonics system, Fig. 2.16b) can be seen to follow a second order relation (an elliptical pattern) between the delay and channel number very similar to eq. 2.14. For focusing of ultrasound bursts at a single point, the verasonics system takes the steering angle (θ) and focus depth (F) as its input and then generates time delays (Δt_n) for each channel (n^{th} element). The measured delays (Fig. 2.16a) follow an elliptical pattern, although with error. Since the relationship between individual element time delays is already known, this knowledge can be used to eliminate these errors i.e. further processing the measured data. This is achieved using the weighted linear least squares method with the measured delays as its inputs. Weighted linear least squares can be used to derive a curve, a 2nd order curve in this case, using the measured delays itself. Considering this estimated curve as the ideal delay curve, the percentage of error in the measured data can be

obtained by comparing this 2nd order polynomial curve with the measured data. The percentage of error is then expressed in terms of goodness of fit (gof) [61]. This gof parameter expresses the closeness between the original data and the estimated curve. If the gof is observed to be greater than 92% (or the error percentage is less than 8%) then the 2nd order curve produced using the measured delays is inverted and then fed to the probe to focus on the active CMUT region. The contribution of the erroneous time delay measurement is lowered by reducing the contributing weights of the most deviated measured delays (with high error) to zero. This effectively eliminates the errors to produce a smooth 2nd curve (the red curve in Fig. 2.16a) needed as input to the probe. It should be noted here that although curve fitting reduces measurement errors, it will also deprive the algorithm of its robustness against an inhomogeneous propagating medium. An inhomogeneous propagating medium alters the wavefronts of the US beam since the acoustic impedance is non-uniform. This consequently delays a few wavefronts of the beam that propagate through the different acoustic impedance regions. The probe would therefore also observe an irregular pattern in the measured delays. The algorithm would however use the 2nd order curve fitting to invert a 2nd order delay pattern that may result in focusing the US beam away from the actual location of the implant.

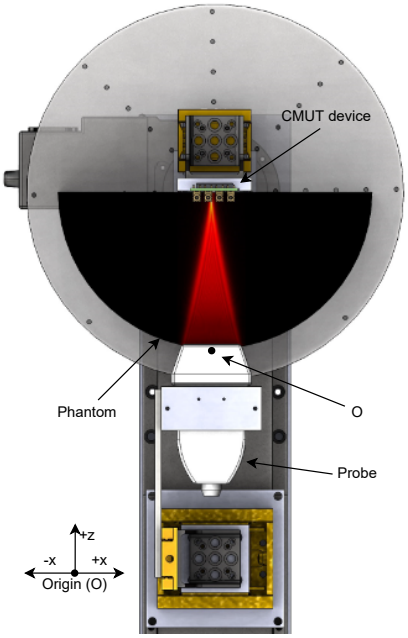

Figure 2.13: New coordinate system with the probe's center at origin (courtesy Y. Westhoek).

The algorithm requires capturing at least one modulated pulse width to invert the delays. In terms of speed, if modulation at a coordinate point can be detected with the gof parameter being greater than 92%, the average time spent at this coordinate point for processing, before shifting to the hot-spot is 0.2 s. The average time taken by different processing steps in the algorithm (Fig. 2.12) is presented as follows:

1. Ultrasound burst's Time of Flight and DMA transfer from acquisition modules to host PC's memory: 0.02 s (refer Sec 1.2.4).
2. Deriving the envelope and computing pulse width: 0.02 s.
3. Computing delays of 128 channels: 0.08 s.
4. 2nd order curve fitting and gof parameter calculation: 0.035 s.
5. Inverting delays and focusing at the hot-spot: 0.03 s.
6. Changing the focus to a new coordinate point: 0.035 s.

Since the response time is low and the accuracy of the tracked hot-spot is high enough, another experiment is performed where the CMUT is continuously moved at a particular speed inside the RoI to check if the tracked hot-spot moves in the same way as the CMUT. The following subsection discusses this experimental setup and the corresponding results.

Go to ToC

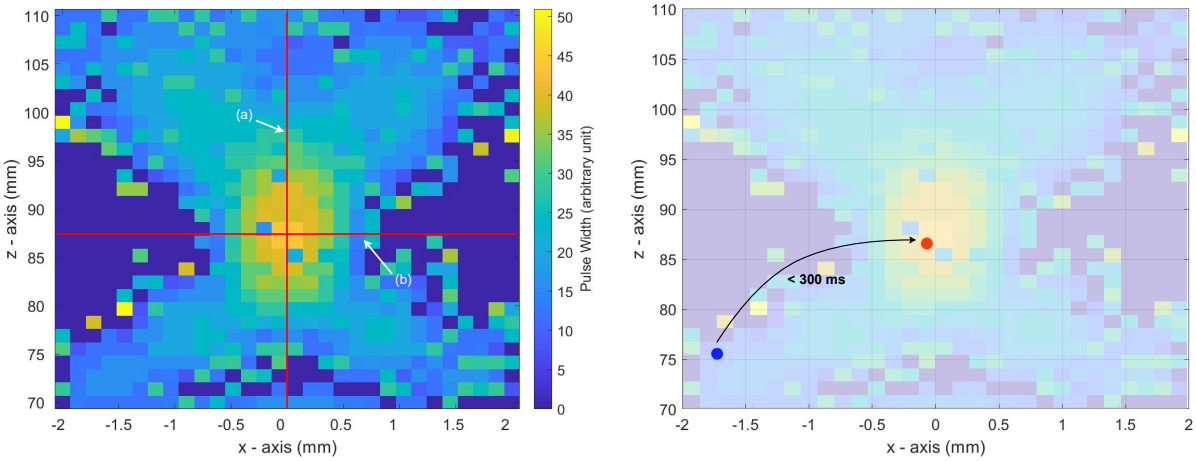

(a) Heat map for new coordinate system.

(b) Hot-spot tracked by the algorithm (red color dot).

Figure 2.14: Results: the heat map and hot-spot.

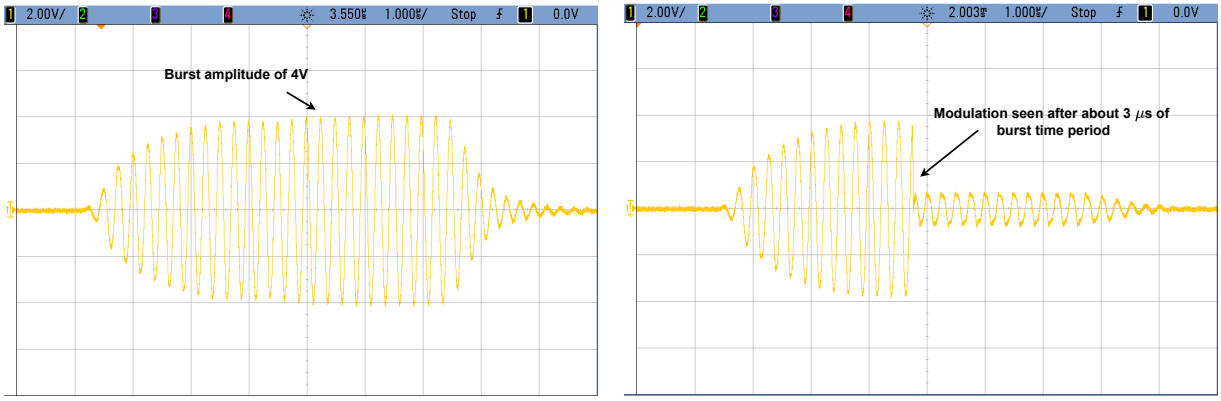

(a) Voltage level measured at CMUT (unmodulated signal).

(b) Voltage level measured at CMUT (modulated signal).

Figure 2.15: CMUT voltage levels measured when ultrasound bursts are focused at the hot-spot.

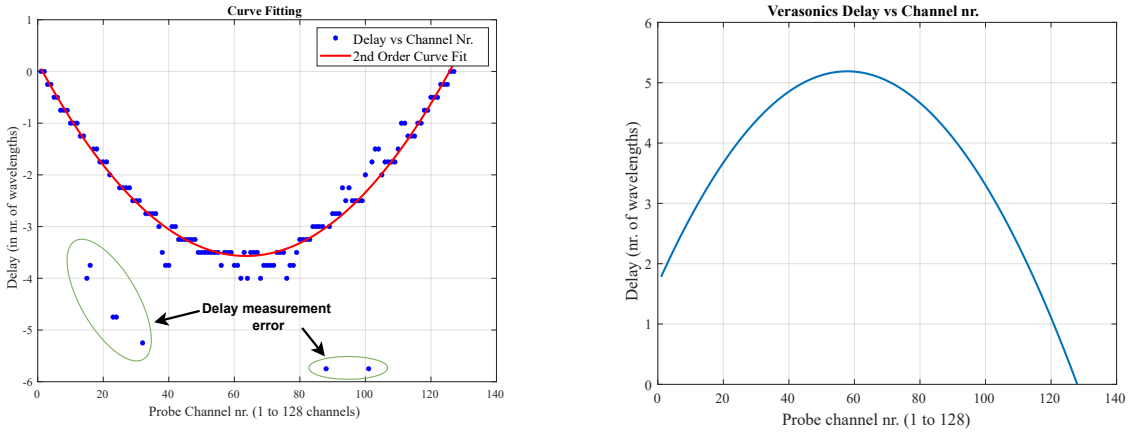

(a) Measured delays and the 2nd order curve.

(b) Typical pattern of delay given as input to the probe channels.

Figure 2.16: Delays corresponding to each channel of the probe.

Go to ToC

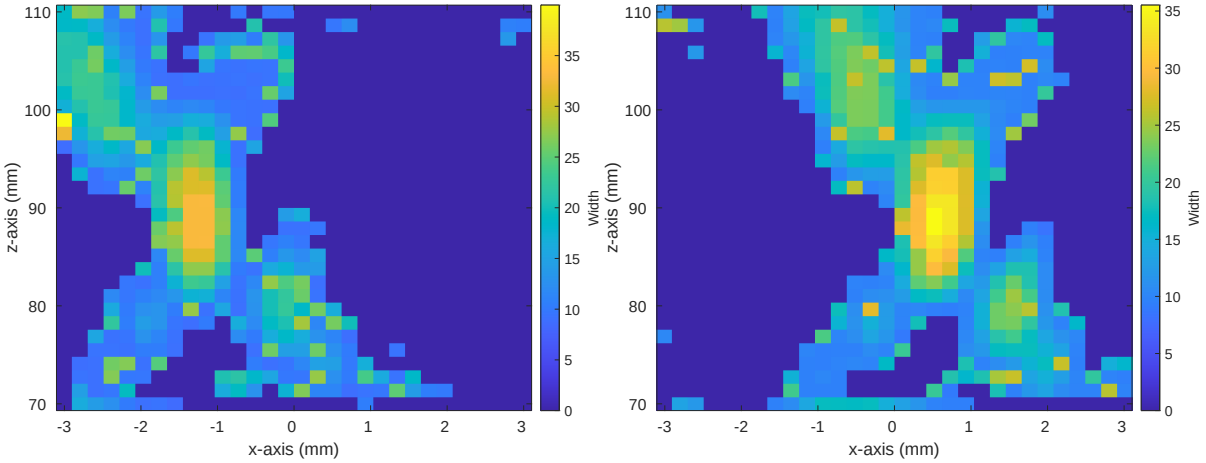

(a) Heat Map before moving.

(b) Heat Map after moving.

Figure 2.17: Heat maps showing two positions of the CMUT device used to test the tracking algorithm.

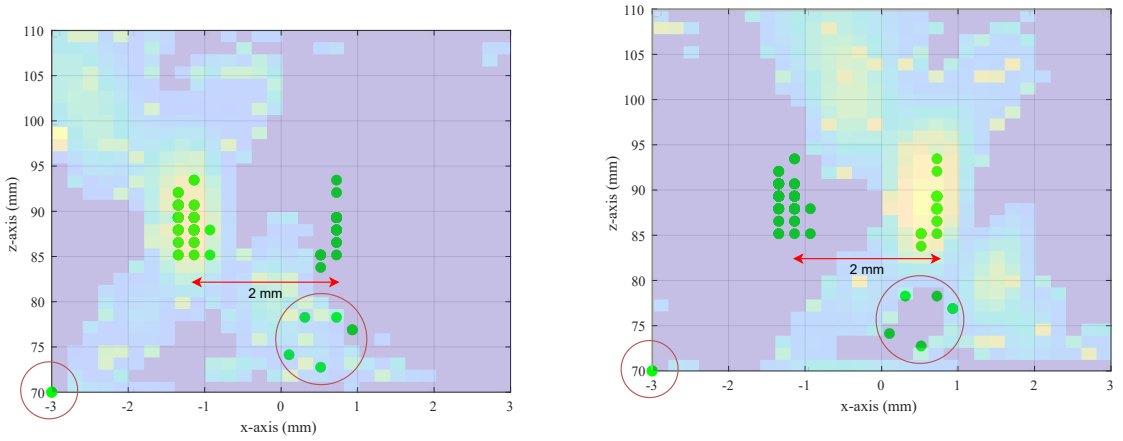

(a) Highlighted points tracked before the CMUT was moved.

(b) Highlighted points tracked after the CMUT was moved from left to right by 2 mm.

Figure 2.18: The location of the coordinate points tracked by the algorithm (in green colored dots). The erroneous tracked points highlighted with a red circle.

2.9.1. Tracking a moving CMUT

Consider the experimental setup shown in Figures 2.4 & 2.13. A new heat map is reconstructed with the CMUT device situated away from the central axis of the probe at around as shown in Fig 2.17a. This experiment involved moving the CMUT device along the x-axis by a distance of 2 mm to the right (+ve x-axis). The resulting heat map is shown in Fig 2.17b. Before moving the CMUT from its initial position, the hot-spot of the CMUT device is tracked using the algorithm. The CMUT device is then manually moved to its new position in about 4 seconds using the micromanipulators present on the rotary stage of the setup (refer Sec 2.4). The algorithm was seen to track the new hot-spot as well. Figure 2.18a and 2.18b show the tracked points before and after the CMUT is moved from its initial position.

To test the tracking capability when the CMUT array is constantly moving, some changes in the experimental setup are made. These changes are highlighted in Fig 2.19. Since the experiment should involve moving CMUTs, the propagating medium is changed to water from gel phantom. This allows us to move the CMUTs at a desired speed and evaluate the tracking capability of the algorithm. The CMUTs are immersed inside a water tank (filled with water) that contains a window on the side. This window is fitted with a PET foil of about 30 µm thickness. The probe is pressed against this sheet along with some acoustic coupling gel in between the two. This sheet is very thin, in comparison to the wavelength being used and acts as a propagating medium or the ultrasound while keeping the water

contained inside the water tank.

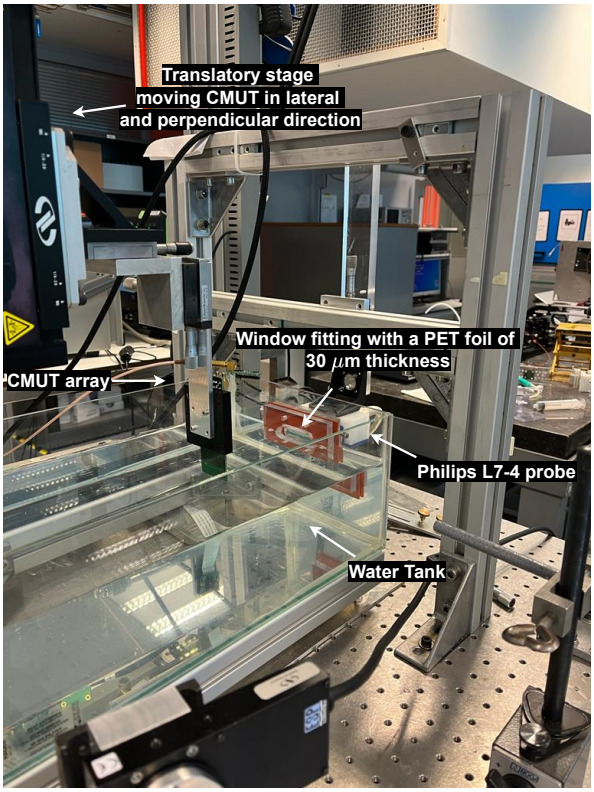

Figure 2.19: Experimental setup to test the tracking capability of the water tank when the CMUT is constantly moving.

The ultrasound waves now propagate in a water medium. A translatory stage is used to move the CMUT array at a constant speed. Similar to Fig 2.18 the CMUT device is moved between two positions at constant speed lateral to the central axis of the ultrasound probe. It is observed that at speeds less than 1.25 mm/sec, the algorithm is able to track lateral movements of the CMUT array. As mentioned previously, the response time of the algorithm is 0.3 seconds. The major contributor of this time is the software processing performed in MATLAB (delay computation and curve fitting). At higher moving speeds of CMUTs, this 0.3 seconds of software processing becomes higher than the time taken by the CMUTs to reach a new position away from the hot-spot. Consequently, even after tracking the CMUTs, the CMUTs are outside the hotspot region and the PWM modulation required for tracking will not be observed. A demonstration of the tracking experiment where the CMUT device is moved between $(x, y) = (-2mm, 120mm)$ and $(x, y) = (+2mm, 120mm)$ at a speed of 0.5 mm/sec is shown here: [62]. At speeds higher than 1.25 mm/sec, it is observed that the algorithm is often not able to track the CMUT device. This happens because, at higher speeds, the shift in the CMUT location is much more than focused beamwidth i.e. the hotspot region in the heat maps (Figures 2.14a,2.17a, 2.17b).

2.10. Conclusion

The Time Reversal beamforming provides robust, efficient and computationally inexpensive means for tracking small implants (CMUT array in this work). Therefore a quick response tracking algorithm can be derived using this principle, as is done in this work. The algorithm initially starts searching for the PWM modulation that acts as the indication for power harvested by the CMUTs. Upon sensing a modulation it uses Time Reversal beamforming to locate the CMUT array in less than 0.3 seconds. The achieved accuracy, although good enough, is very dependent on the delay measurement accuracy of the system. A slight error in the delay measurement is seen to change the focus by a few wavelengths (mm) of distance away from the actual CMUT location. Therefore curve fitting is used to generate a 2^{nd} order delay pattern to focus on the CMUTs. To test the tracking ability of the algorithm a slight change in the experimental setup was performed. The propagating medium was changed to water and the

CMUTs were moved at a constant speed. The tracking algorithm is able to track the CMUTs that move at a speed of 1.25 mm/s.

This work provides proof of concept for implementing Time Reversal beamforming to locate small sized deep implants. In addition to locating the implant, the system also focuses an ultrasound beam on the implant i.e. an ultrasound link will be established between the implant and the external when the implant is located. This link will always be maintained since the implant is continuously tracked. This helps in continuously powering the device which can be further used for communication, navigation, etc. The next chapters present the other half of the thesis in which, this link is further used to communicate with the implant.

3

Ultrasound Communication

3.1. Introduction

Interaction with Implantable Medical Devices (IMDs) allows us to monitor physiological activities and deal with them appropriately. To mention a few, communication with the IMDs allows us to: :

- access endoscopic images from the ingestible capsules that are probed deep inside the body cavity which would also require high data rates [63].
- relay pressure sensor readings to diagnose and treat cardiovascular issues, enuresis, glaucoma, etc [18].
- Glucose monitoring for closed-loop insulin administration [64].
- record gastric electrical activity to better understand gastric dysrhythmias [65].
- set and tune the output current amplitude, repetition intervals and pulse of Implantable Pulse Generators that stimulate the vagus nerve for epilepsy treatment [66], [67].

In nearly all the above medical use cases, RF transmission has been the steadfast communication technology. However, RF transmission suffers from a few disadvantages. High frequency RF transmission (> 1GHz) that offers high data rate and bandwidth, suffers from significant attenuation of the transmitted signal (> 10 dB/cm) [17]. RF transmission with carrier frequencies less than 1 GHz implements communication in the near-field region since the wavelengths are in the range of a few centimeters (in the range of the implant's location). This brings additional requirements of proper antenna alignment due to the directional sensitivity of RF receivers in the near-field region to avoid distortion and interference [68]. Furthermore, wavelengths in the range of cm also require the implant's antenna to be in the same range.

Considering ultrasound (US) as an alternative to RF transmission for communication is justified due to the same reasons as for the power transfer (refer Chapter 1). Although US offers advantages over RF transmission, there are certain challenges that need to be addressed. Focusing ultrasound beams, one of the advantages of US power transfer, increases the directional sensitivity of the implant. For an implant of 1 mm^3 volume, a shift of a few mm in the focus point's location can significantly reduce the amplitude of the voltage signal (even by 50%) harvested by the US transducer. This in turn reduces the SNR of the data signal received by the implant. Diagnostic US sonographic scanners operate in the frequency range of 2 MHz to 18 MHz [69]. The implants that utilize ultrasound for power transfer and communication that are found in the literature also use a transmission frequency not greater than 20 MHz. Additionally, US transducers are operated in resonance conditions i.e. in a narrow frequency band in the range of kHz to MHz. These two reasons imply that the data rate achieved based on the carrier frequency alone is always a few orders of magnitude lower than what could be achieved using RF transmission. This calls for the use of complex modulation techniques such as Frequency Division Multiplexing (FDM), Quadrature Amplitude Modulation (QAM), Quadrature Phase Shift Keying (QPSK), etc, in order to transmit symbols of multiple bits instead of single bit transmission for greater data rate [70]. These complex modulation techniques require many power hungry components and circuits such as Phase Locked Loops (PLLs) for demodulation while the implant receives data. Therefore

the typical power consumption versus data rate disparity is introduced as another challenge. A good way to deal with this is implementing non-coherent demodulation for forward telemetry (external world to the implant) and data encoded passive communication for back telemetry (implant to the external world). Non-coherent demodulation saves power consumption since the generation of the clock and maintaining the coherency between the locally generated clock and external carrier pulse is not required. The use of complex modulation techniques to transmit multiple bits while refraining from generating a carrier burst (passive modulation) can maintain a good data rate at low power [71].

The objective of this part of the thesis is to develop a communication protocol that implements the above mentioned non-coherent demodulation and passive modulation. Prior to discussing the protocol an overview of the implants implementing US based communication is presented while emphasizing on their communication protocols and data encoding methods, in Section 3.2. Moving further into this literature review, Section 3.3 introduces the different parts of the circuit designed to perform tracking and data communication. Section 3.4 discusses the proposed protocol that involves three functions of the designed circuit namely: tracking, back telemetry and forward telemetry. Section 3.4.2 revisits the proposed protocol and circuit while describing the link between the circuit parts and the proposed protocol in a flowchart. Moving further Section 3.5 describes different components used in the circuit while presenting the simulation results. Following these following results, the experimental results are discussed in Section 3.6 followed by the chapter conclusion, Section 3.7.

3.2. Overview of US based Implants

Wireless communication involves the transmission of a modulated carrier wave (either analog or digital) and the type of modulation scheme determines the electronic architecture of the implant. This modulation is modifying one of the wave parameters namely: amplitude, frequency & phase to represent the data required to be transferred. Complex modulation schemes modulate more than one of these parameters at a given time, thereby increasing the data rate. The literature consists of various US implants and experiments implementing common modulation schemes such as Amplitude modulation (AM), Amplitude Shift Keying (ASK), Pulse Position Modulation (PPM) etc., and complex symbol modulation such as Quadrature Amplitude Modulation (QAM), Quadrature Phase Shift Keying (QPSK) that are used for high data rates. Moving further in the report, the two modulation schemes: ASK & PPM that served as the inspiration for the communication protocol implemented in this work are discussed.

Amplitude Shift Keying (ASK)

Amplitude Shift Keying involves the transmission of data in the form of a modulated amplitude of a wave (carrier wave) to represent binary bits: ’0’ and ’1.’(Fig 3.1). In [72], a modulated US burst signal is made to incident on the piezo based US transducer of the implant. This ASK modulated US wave is demodulated using an amplifier stage followed by an envelope detector and a hysteresis comparator [73]. The amplifier stage employs a Low Noise Amplifier (LNA) and a Variable Gain Amplifier (VGA) to boost the amplitude of the electrically converted modulated acoustic signal. The envelope of this amplified signal is detected and converted into a digital signal using the comparator. This digital signal represents the binary bits that are intended to be transferred as shown in Figure 3.1).

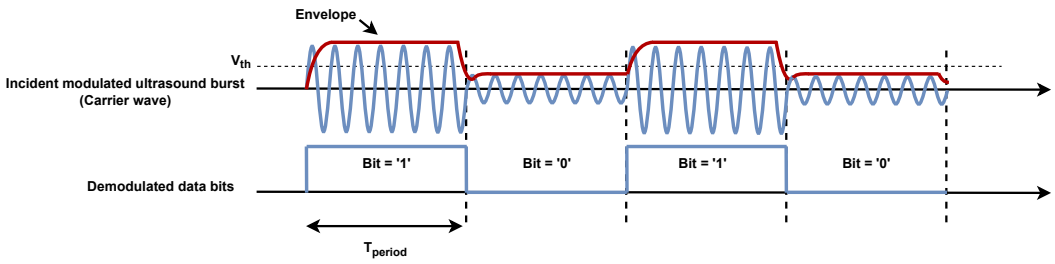

Figure 3.1: Amplitude Shift Keying (ASK) Demodulation. If the envelope level (in red) is greater than V_{th} then bit ’1’ is transmitted. If the envelope level is lower than V_{th} then bit ’0’ is transmitted.

The implant does not involve any typical matching inductor or resistor for operating the piezo element in resonance. Instead, the variable gain stage with gain varying between 30 dB and 58 dB is designed to amplify the low amplitude electrical signals (gain of 58 dB) while avoiding saturation of the receiver

when harvesting higher amplitude electrical signals (gain of 30 dB). This amplifier stage along with the envelope detector and hysteresis comparator, implemented using CMOS 0.18 µm technology, is reported to consume a very low power of 184 µW and achieve a data rate of 50 kb/s (kilobits per second) while using a carrier frequency of 1 MHz. This type of demodulation does not require on-board Phase-Locked Loops (PLL), Injection Locked Oscillator (ILO) or other forms of digital clock generator circuit for decoding transmitted bit stream [74]. However, the absence of a clock renders the extracted data bits purposeless and the maximum data rate is limited to the carrier wave frequency and the time constant of the envelope detector.

ASK modulation can also be implemented for back-telemetry, as reported in [41]. In this work, back telemetry and forward telemetry is performed simultaneously by utilizing two piezo transducers on the same implant. The implant involves a number of units performing: power management, clock recovery, power amplifier, a frequency generator, a finite state machine and a pseudo random binary sequence generator as shown in Figure 3.2. One of the two piezo transducers (piezo 'a') is utilized for power transfer and forward telemetry. The power management unit, which consists of a charge pump and storage capacitor, harvests energy from the incident ultrasound burst. The input clock, recovered from the incident US burst, is up-converted using the frequency generator. The up-converted clock and the stored power are used to drive the other US transducer (piezo b) using the power amplifier. A reported data rate of 95 kb/s of data rate at a depth of 8.5 cm is achieved while utilizing a transducer driving (carrier) frequency of 2.45 MHz, which is recovered and up-converted from an input carrier frequency of 950 kHz. It is also reported that a minimum of 100 µW of power is required only to drive the forward telemetry transducer (piezo 'b') for the above mentioned depth. Driving the transducer at a higher frequency for a higher data rate and for increased depth would consequently require much more power. Since the other implant units need to be powered from the same US waves, piezo 'a' needs to be primarily used for power transfer with time multiplexing the forward telemetry [65]. This gives little room for increasing the data rate in the forward direction. Additionally, since the power required to drive piezo 'b' for back telemetry, is also extracted from piezo 'a', the use of two transducers appears to be inefficient. As long as the incident and reflected US waves are made to travel in the plane of the transducers, a single transducer can be utilized to save space and power (refer Section 2.5).

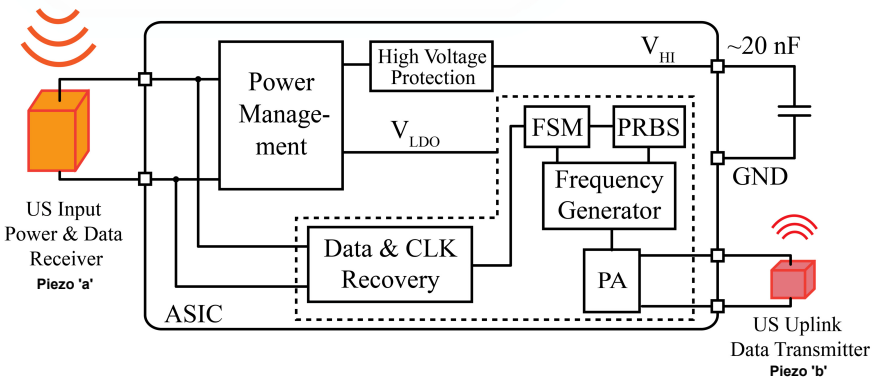

Figure 3.2: Block diagram representing US based powering and communication system developed in [41].

Pulse Position Modulation (PPM).
Consider the data and clock signals shown in Figure 3.3. This Figure demonstrates the transmission of a bit stream '1001' using Pulse Position Modulation (PPM). Bit '1' is represented by a data pulse that is delayed by δ in the time domain with respect to the clock signal. Bit '0' is represented by a data pulse that has no delay with respect to the clock signal. In other words, the position of the clock pulse determines the type of data bit that is being transmitted. The position of this delayed pulse with respect to the clock cycle determines its place value i.e. B0, .., B3 (Bn). In [75], the authors used this principle to develop what is called Ultrasound Wide Band (UsWB) communication protocol.

UsWB was developed in order to effectively mitigate the scattering and multi-path effect faced by ultrasound bursts in the human body. Based on acoustic wave propagation equations: the continuity equation, force equation and equation of state [76], a tissue model for ultrasound propagation was developed by the authors. This model is used to mimic the characteristics of a human arm that includes

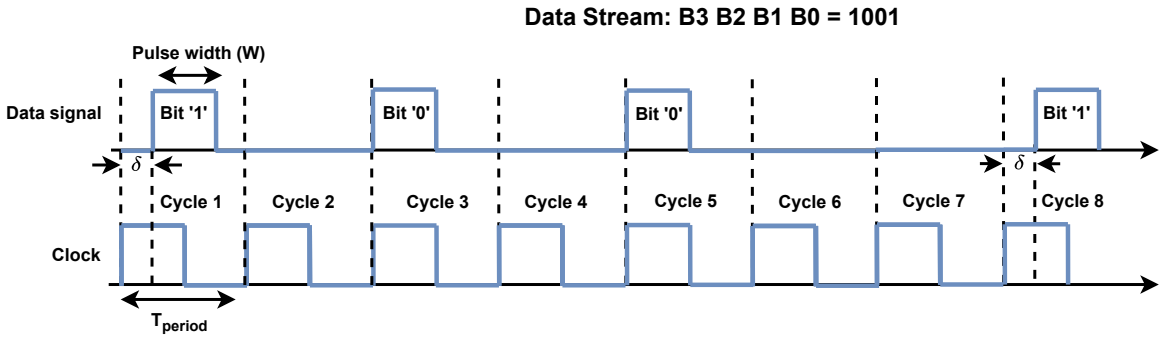

Figure 3.3: Pulse Position modulation showing two signals: data and clock, implemented in [75]. Bit '1' is represented by a pulse with a delay of δ between the clock signal and the data signal. Bit '0' is represented by a data pulse with no delay between the data signal and the clock signal.

skin, fat, muscle and bone. By placing an ultrasound emitter at one of the ends of the arm, a simulation of wave propagation is performed. It was seen that the reflections made by the change in the medium added attenuated replicas of the original ultrasound pulses in the time series recorded by a receiver at a place at the other end of the arm, i.e. multi-path effect. These replicas can cause destructive interference and attenuate the original US echo. Figure 3.4 depicts this multipath effect seen in intra-body communication using US devices. Figure 3.4a demonstrates three paths the US waves can travel to reach the receiver (RX). The change in acoustic impedance due to change in propagating medium (lungs, bone, intestines, air) causes reflection of these waves and hence creates additional paths for propagation. These multipath replicas (Fig 3.4c)can be seen to appear as an extension of US burst transmitted from TX to RX.

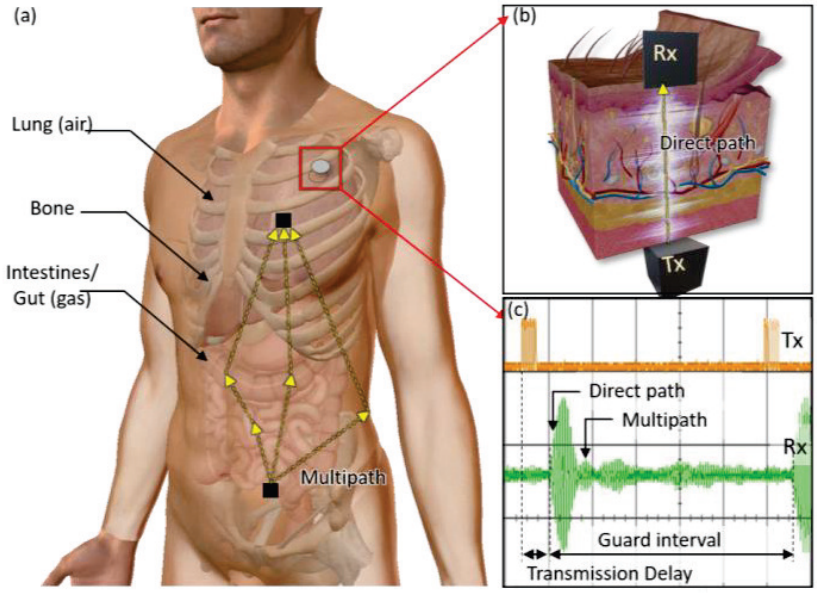

Figure 3.4: (a) Depiction of an intra-body communication between a single US transmitter (TX) and Receiver (RX) (b) Depiction of the desired direct path. (c) Replicas (multipath) of the original burst (direct path) providing destructive interference [68].

UsWB involves the use of ultrasound pulses with pulse widths (W) (Fig 3.3) that are in the order of a few hundred nanoseconds. By using such short-lasting pulses the authors managed to isolate the multi-path effect replicas. Since the pulses had a small width, the delays caused by the scattering proved to be greater than the pulse widths themselves and hence destructive interference and pulse overlaps can be avoided. Furthermore, the protocol allows for data rate and power rate adaption by using a time hopping sequence, wherein data bits are transmitted at different instances of the clock cy-

cle as shown in Figure 3.3. This time hopping sequence can be utilized to communicate with individual implants in a network of implants by designating each implant with a specific hopping sequence. When the external transmitter tries to communicate with a particular implant, the corresponding hopping sequence can be utilized to transfer data bits while rendering other implants inactive. Furthermore, this hopping sequence method allows for flexibility in data rate and power consumption. For low data rate measurements such as pressure recordings, the data pulses can be placed far apart in time to minimize power.

Based on this principle, the authors implemented UsWB using an FPGA-based prototype in [64]. A data rate of 700 kb/s (kilobits per second) at a transmit power of 40 µW and a lower data rate of 70 kb/s at a transmit power of 8 µW was successfully achieved by the authors. While the protocol allows for high speed data communication at lower power consumption, it requires coherent detection to compute the delays (δ). It requires time hopping synchronization in order to decode the data bit stream sent to the particular implant [75]. Furthermore, along with time hopping synchronization, a clock signal is required to determine the type of data bit ('1' or '0') that is being transmitted. It should, however, be noted that the use of short duration US pulses (UsWB) is able to achieve a high data rate of a few hundred kb/s while compensating for multi-path effects.
ASK scheme can be implemented using a switch that turns OFF and ON to modulate the amplitude of a US burst. PPM modulation can be decoded easily with the presence of a clock signal and by using similar components that are used for ASK demodulation in Figure 3.1. Both the schemes are able to provide a data rate of a few tens of kb/s to a few hundreds of kb/s making them a good option for applications involving ECG, EEG & audio signal acquisitions [77]. Owing to their implementation simplicity, reported low power consumption and good data rates these two schemes are adopted for data communication in this work. In this section, an overview of US based communication schemes has been discussed. For a low power US based implant non-coherent demodulation for Forward Telemetry and passive modulation involving backscattering of US burst for Back Telemetry serves as an optimal solution (as mentioned in the previous section). Accordingly in this work Amplitude Shift Keying (ASK) of the back-scattered US burst is used to implement Back Telemetry and a variant of the PPM scheme is used to implement non-coherent demodulation for Forward Telemetry. The rest of the report discusses the US protocol formulated in this work along with its proof of concept. This starts with the next section where an overview of different parts of the circuit developed in this work. The protocol is based on the ASK and PPM discussed above with slight changes made to adapt to decrease the complexity of the circuit design.

3.3. Circuit Overview

Figure 3.5 depicts a block diagram of various parts of the circuit that is proposed in this thesis. This circuit implements both the PWM protocol developed in the previous work [78] and the data communication protocol formulated in this work. The circuit involves the following parts:

a. Maximum power transfer using external inductor and resistor to operate the CMUT drums in resonance.
b. The tracking circuit that implements the PWM protocol used in the tracking of the CMUTs.
c. A clock recovery circuit and a counter that is used in the data communication protocol.
d. An amplitude demodulator for extracting data bits from PPM modulated US burst sent from the verasonics to the CMUTs.
e. A microcontroller unit that acts as the brain of the device and switches between different states to implement both tracking and data communication (further discussed in Section 3.4).
f. A modulating switch that shorts the CMUTs to modulate the amplitude of the reflected ultrasound burst, hence implementing ASK for Back telemetry and also PWM protocol as mentioned in Section 2.6.

a. Max Power Transfer:
The ultrasound probe transmits bursts of 4 MHz frequency. To harvest maximum energy from the incident ultrasound bursts the CMUT's reactive impedance must be zero and the load resistance must be equal to that of CMUT's source's resistance as discussed in Section 1.2.2).

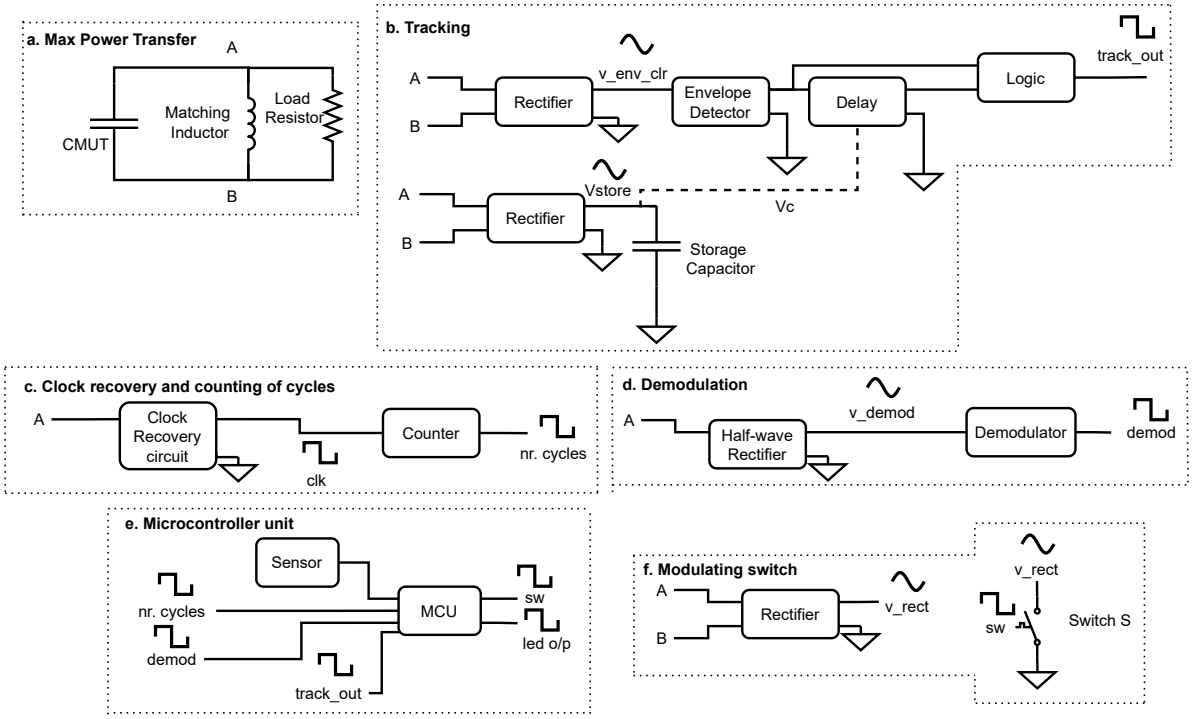

Figure 3.5: Block diagram of the proposed circuit.

A matching inductor connected in parallel with the two terminals of the CMUTs compensates its capacitive impedance. When the capacitive impedance is matched, the reactive impedance seen across the two terminals of the CMUTs is negligible. Consequently, the amplitude of the voltage, which is harvested from the ultrasound burst, across the CMUTs reaches a maximum. The value of this matching inductor was previously estimated to be 1.845 µH as mentioned in Section 1.2.3. Since this value is an estimate a small number of other inductors in the range of this estimate are connected in parallel with the CMUTs and the RMS voltages of the received ultrasound burst are noted to determine the appropriate matching inductance. Figure 3.6 shows these observation results. It can be seen in the figure that when an inductor of 3.9 µH is connected across the two terminals of the CMUT, the observed amplitude of the US burst is maximum. This indicates that the compensated reactive impedance is the lowest for 3.9 µH and hence 3.9 µH is the appropriate matching inductor.

After compensating the capacitive impedance of the CMUTs, R_m (Fig 1.4) needs to be compensated for maximum power transfer. As mentioned in Section 1.2.3 value of the matching resistor R_l would be slightly different from its estimated value using impedance spectrum analysis. Once again a small range of resistors, R_{load} is connected across the CMUTs. The power consumed by this load resistor is noted down. When this load resistor is equal to the internal resistance of the CMUTs, we observe that the harvested power is maximum. These observation results are shown in Fig 3.7. Maximum power is harvested from CMUTs when the load resistance is equal to 300 Ω.

After connecting 300 Ω and 3.9 µH across the CMUT terminals, it is now prepared for efficient power transfer as well as data communication.

b. Tracking:

Figure 3.8 shows the schematic diagram of the circuit implementing the PWM protocol that is used to track the CMUTs. The circuit design is adopted from previous work with a small change [78]. The envelope of the rectified ultrasound burst is detected using a common RC envelope detector. This envelope of the burst is converted into a digital signal using a comparator with hysteresis (upper threshold voltage, V_{th} = 0.6V and lower threshold voltage, V_{tl} = 0.3V). This digital signal *env_clk* goes high if the CMUTs received a US burst, hence indicating the presence of a US burst.

One of the main components of the tracking circuit is the varactor diode that is used to relate the length of the modulation in the PWM protocol with the amplitude of the incident burst [23]. The capacitance of the varactor diode is a function of the reverse bias voltage applied across it. An RC delay

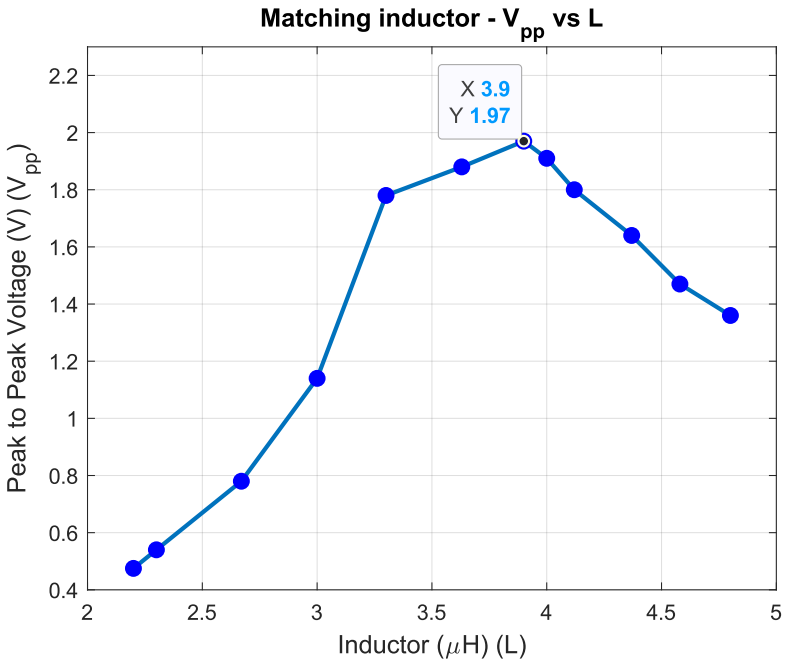

Figure 3.6: Inductance matching for maximum power transfer.

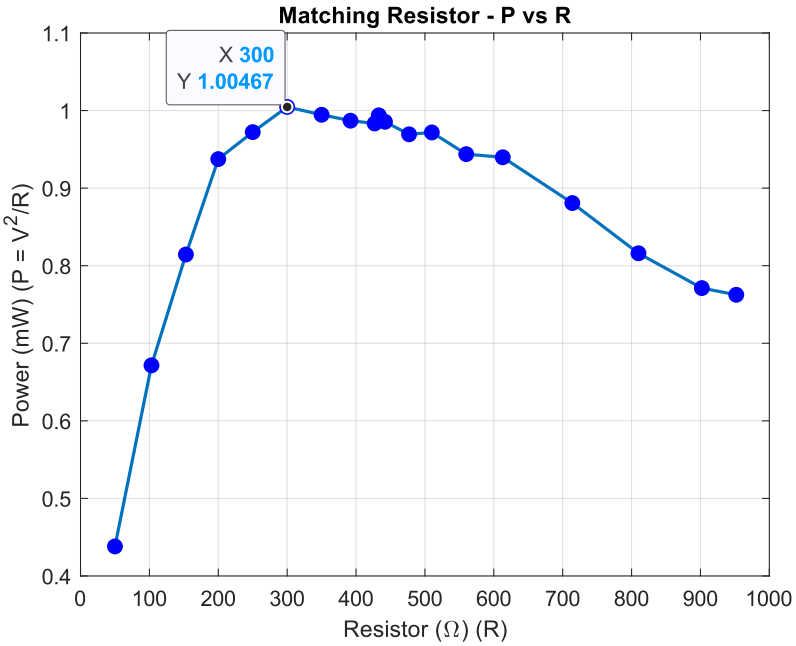

Figure 3.7: Resistor matching for maximum power transfer.

element is used to delay the digital envelope signal *env_clk*. This delay is made variable by using the above mentioned varactor diode as the capacitive part of the RC delay element (Fig 3.8).

The US burst is rectified and the energy is stored in a storage capacitor. This storage capacitor is used to bias the varactor diode. The voltage of the storage capacitor (V_c) is proportional to the amplitude of the ultrasound burst. This implies that the capacitance of the varactor diode and hence the delay produced by the RC delay element is also proportional to the amplitude of the ultrasound burst. This delayed signal is once again converted into digital using a Schmitt trigger. Hence the signal *track_out* is basically a burst amplitude dependent time delayed envelope signal. This *track_out* is used to turn

on a switch connected across the CMUTs to modulate the amplitude of the incident ultrasound burst to implement the PWM protocol discussed in Section 2.6.

Furthermore, a D flip-flop is used in toggling mode to identify even or odd bursts (Fig 3.8). The inverting output $\overline{Q}$ is connected to the input *D* of the flip-flop and the digital envelope *env_clk* signal is given as the clock input of the flip-flop. The output *q_track* of the flip-flop toggles between high and low every time there is a rising edge in the *env_clk* signal. Hence the output of this flip-flop indicates that the current burst is either an even burst or an odd burst.

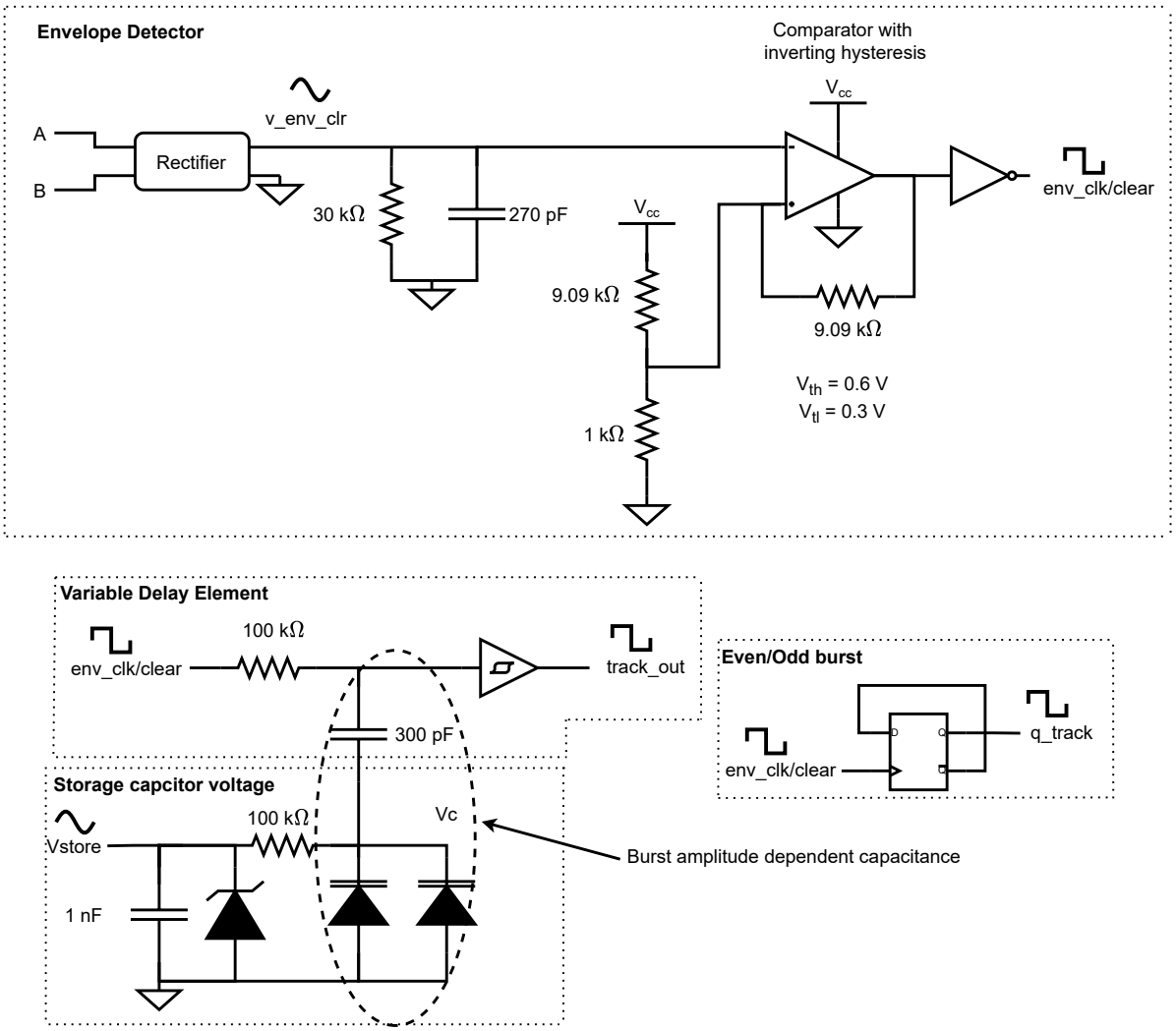

Figure 3.8: Schematic diagram showing the elements implementing the PWM protocol used in the tracking of the CMUTs.

Figure 3.9a shows the burst amplitude dependent time delayed envelope signal. The first burst with a low amplitude produces a *track_out* signal that is delayed by w_a in the time domain. The second burst with a higher amplitude produces a *track_out* signal that is delayed by w_b such that w_b is greater than w_a. Figure 3.9b shows the output of the toggling mode D Flip-Flop used to identify the even/odd burst. Every odd burst is identified by a low level *q_track* signal and every even burst is identified by a high level *q_track* signal.

c. Clock Recovery and Counter:

The Back Telemetry protocol proposed in this work implements the ASK scheme on the backscattered US burst (as mentioned in Section 3.2). The ASK scheme requires a reliable clock signal to modulate the amplitude of the burst signal according to the data bit intended to be transferred (further discussed in Section 3.4.1 and 3.5). Furthermore, tracking of the CMUTs is achieved by transmitting an ultrasound burst of 24 cycles. The proposed communication protocol utilizes 128 cycles in a single burst for data

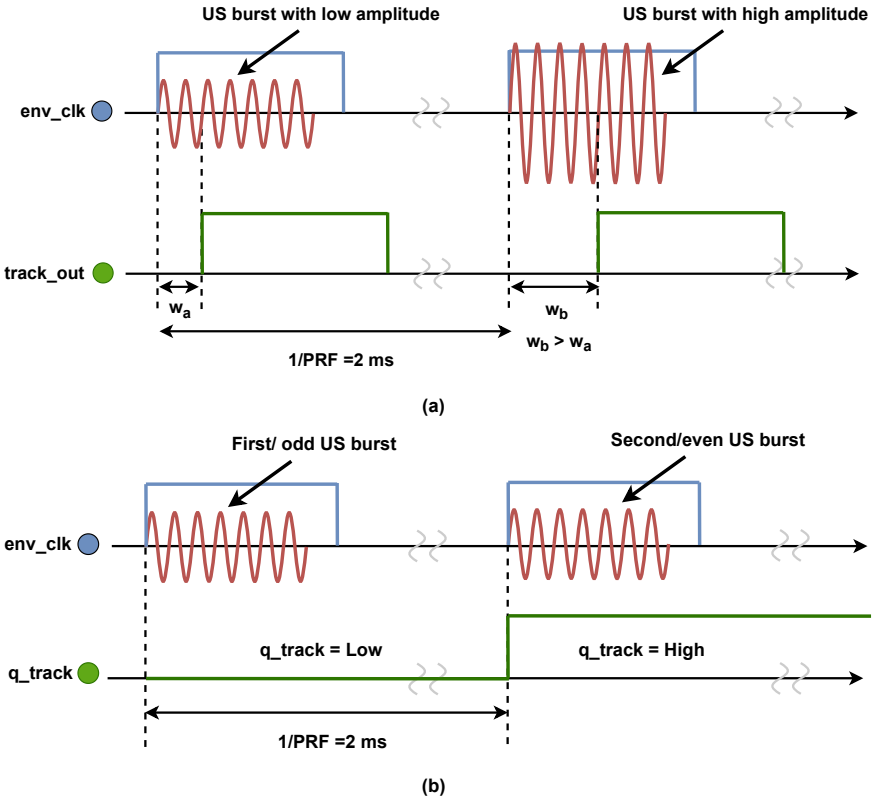

Figure 3.9: (a) Waveform depicting the output signal *track_out*. (b) Waveform depicting the output signal *q_track*.

transfer. The switch between the tracking of the CMUTs and the data transfer is dependent on the number of cycles present in a single ultrasound burst (further discussed in Sec 3.4). Therefore a clock signal and a counter are needed.

This clock is generated by using a comparator that is provided with external hysteresis [73]. This comparator converts the sinusoidal waves into square waves of amplitude equal to V_{cc}. Figure 3.10 shows the schematic diagram of the clock recovery circuit. The (relatively) positive terminal of the CMUTs is connected to the negative input of the comparator. An inverting external hysteresis is applied by using a feedback resistor. The upper threshold and lower threshold voltages are: V_{th} = 0.2 V and V_{tl} = 0.1 V. These threshold values are selected to ensure a clock is generated even when the CMUTs are short-circuited for modulation. The output of the comparator is inverted to produce the clock signal. This clock signal is connected to a 7-bit counter to count the number of sinusoidal waves in the burst.

A 7-bit synchronous positive-edge triggered up-counter is designed using J-K Flip-Flops to count the number of cycles in the clock signal. The inputs J and K of flip-flops are connected to use flip-flops as T flip-flops. The output of the envelope detector is connected to the 'clear' input of the counter to make sure that the number of cycles is counted only when the CMUTs receive a US burst. This also resets the counter when no ultrasound burst is received by CMUTs. Figure3.11 shows the schematic diagram of this counter.

a 7-bit Counter requires 7 Flip-Flops, T Flip-FLops in the case. The clock signal is connected directly to the clock inputs of all the Flip-Flops to operate the counter synchronously. The counter has 7 outputs namely: *q0*, *q1*, *q2*, *q3*, *q4*, *q5* and *q6*. This counter counts up to 128 cycles and also starts counting from zero after it has completed counting 128 cycles.

d. Demodulation:

The proposed data communication protocol utilizes a variant of PPM for Forward Telemetry (discussed further ins Section 3.4.1). An amplitude demodulator is used to convert the modulated burst into pulses representing data bits and hence decode the information transmitted from the Verasonics to the CMUTs. Figure 3.12 shows the circuit used to demodulate an amplitude modulated signal. The ultrasound burst received by the CMUTs is rectified to produce the signal *v_demod*. An RC low pass filter is used to

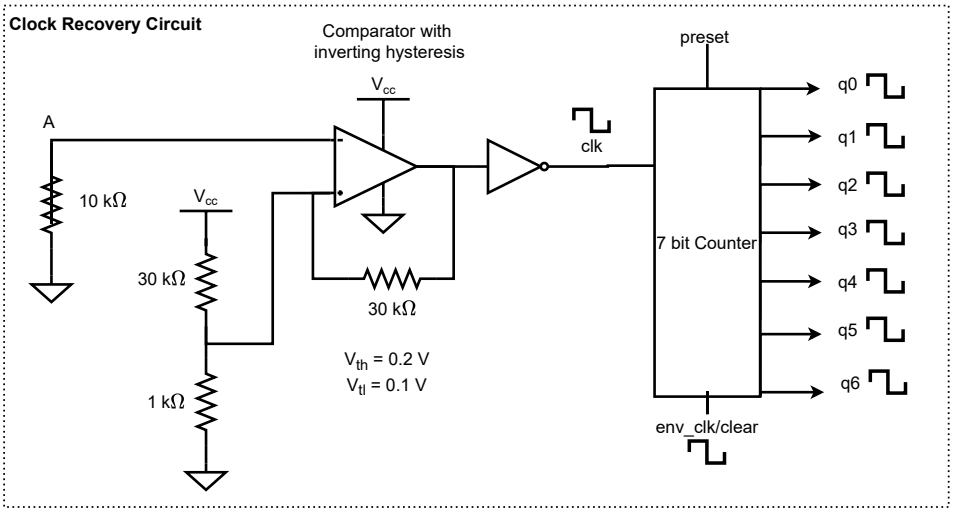

Figure 3.10: Clock recovery circuit using a comparator with external hysteresis. The output of the clock is connected directly to the counter.

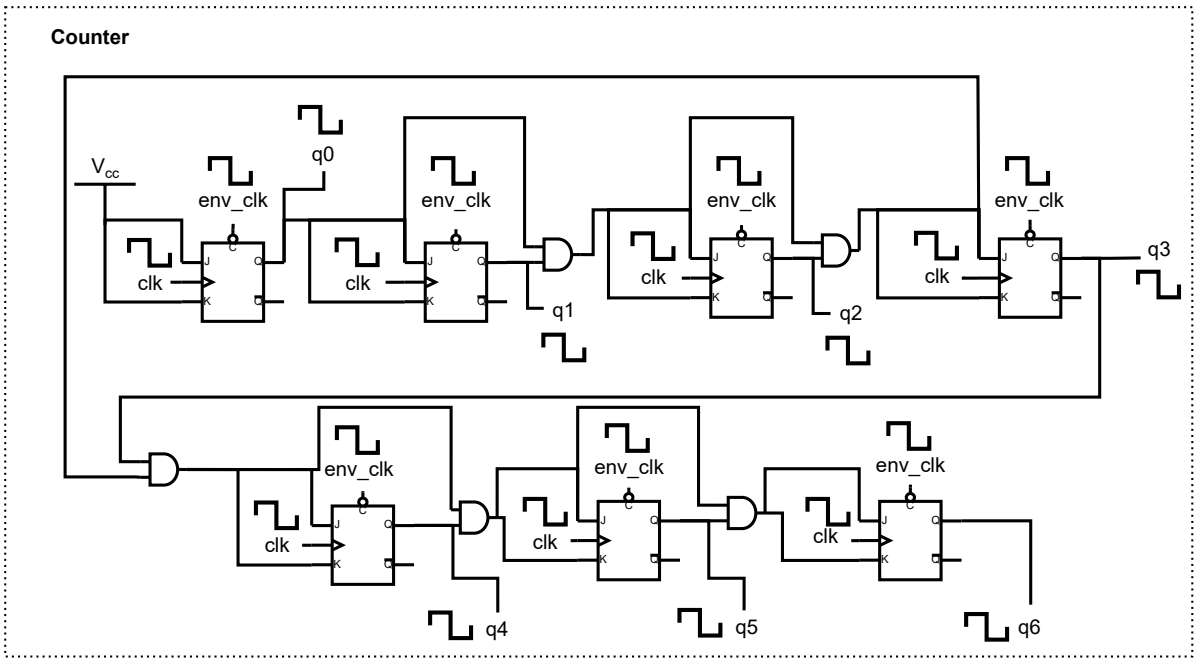

Figure 3.11: 7-bit synchronous positive-edge triggered up-counter is designed using J-K Flip-Flops.

filter out high frequency components in *v_demod*. The low pass filter produces a signal similar to that of the envelope of the burst since it allows low only frequency signals. A comparator with hysteresis (V_{th} = 0.6V and V_{tl} = 0.4V) is used to convert this filtered signal into a digital signal i.e. into pulses representing the data bits. The demod signal is high when no burst is received by the CMUTs and is low when the CMUTs receive a burst.

e & f. Microcontroller Unit & Modulating Switch:
The digital signals generated by the demodulator, counter and the tracking part of the whole circuit is given as an input to the microcontroller (MC). This MC acts as the brain of the whole circuit and is programmed to switch between different states (Sec 3.4) and perform tracking and data communication. Figure 3.13 shows a block diagram of the microcontroller and the modulating switch. A Teesny 4.0 [79] board is used as the microcontroller. An NMOS switch connected across the CMUTs through a rectifier is used to modulate the amplitude of the incident burst to implement PWM protocol for tracking and

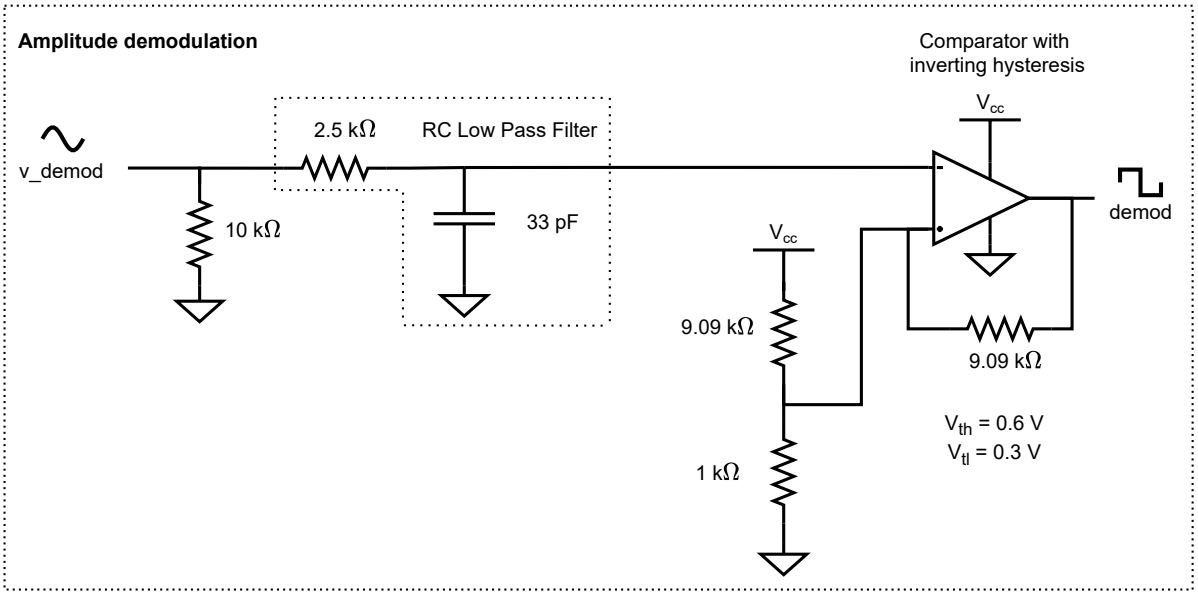

Figure 3.12: Demodulator circuit used to indicate a break in the ultrasound burst.

ASK for back telemetry(Sec 2.6 & 3.4.1).

A total of 19 pins of the microcontroller are used as shown in Fig 3.13. The MC reads the output of the 7-bit counter (*q0* to *q6*) to determine the burst length. It reads the *env_clk* and *q_track* signals to determine the odd and even bursts. Signals *track_out* and *demod* are read to implement the PWM protocol used in tracking and to decode the transmitted data from the ultrasound probe to the CMUTs, respectively. Signals *sda* and *scl* represent the I^2C data and clock lines of the sensors that are connected to the microcontroller. These two pins are intended for communicating vital readings with a sensor. The red, yellow and green LED signals, connected to their corresponding LEDs, are used to demonstrate the decoded data received by the CMUTs from the ultrasound probe (verasonics). The MC generates a digital output signal *sw* that is used to turn on the NMOS switch for modulating the amplitude of the ultrasound burst.

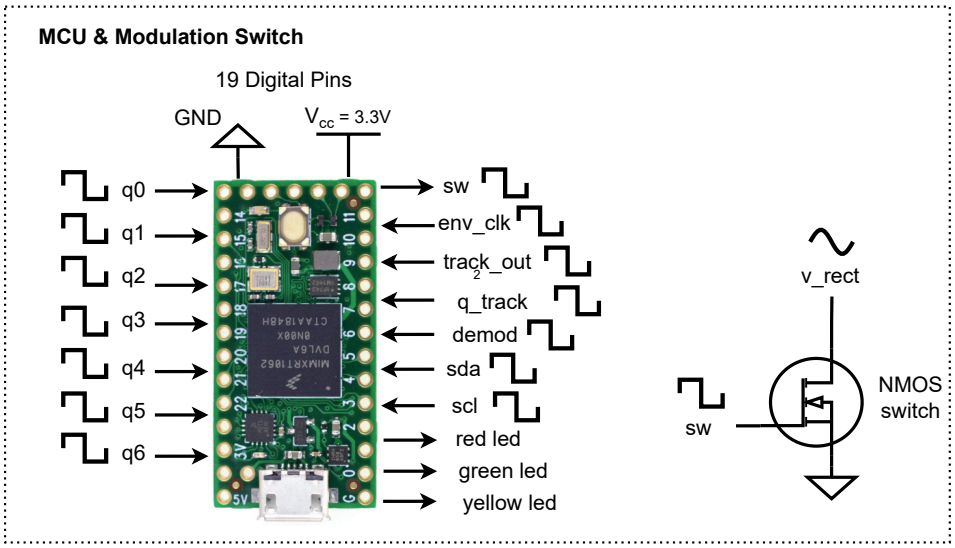

Figure 3.13: Microcontroller unit and the modulating switch.

3.4. Communication Protocol

The protocol that is discussed in this chapter is formulated to perform three functions, namely: tracking of the biomedical implants as discussed in the previous chapter, forward telemetry to turn on the LEDs for indicating the decoded bit stream and back telemetry to transfer measured sensor readings such as heart rate or blood oxygen level to the outside world. Figure 3.14 shows a conceptual block diagram of this protocol that implements these three functions. Starting with an OFF state, no ultrasound beam focusing is done previously. The CMUTs did not harvest energy and the storage capacitor does not contain any energy. The location of the CMUTs is not known yet and hence the tracking algorithm is implemented (T_1 .... T_n). The algorithm begins by scanning the Region of Interest (RoI) by focusing the ultrasound beam at various coordinate points (Fig 2.9). When the ultrasound beam is focused near the CMUTs region, the ultrasound energy is harvested and the capacitor starts to store the energy. After harvesting enough power, the circuit implements the PWM protocol for tracking the CMUTs location (Sec 2.6). After successfully locating the implant the ultrasound beam is now focused on the CMUT drums, hence establishing a focused US link between the CMUTs and the probe. Assuming that this focused US link transfers sufficient power to the CMUTs data communication is now established. Either forward telemetry or back telemetry is performed. To ensure that the ultrasound link is strong i.e. to maintain the focal region of the ultrasound beam around the CMUT drums, the communication is terminated and tracking is performed after every 5 words (D_1 .... D_5) of data transfer. In case the CMUTs are out of the focal zone, the algorithm tracks the CMUTs and then performs data communication after establishing a reliable focused US link again.

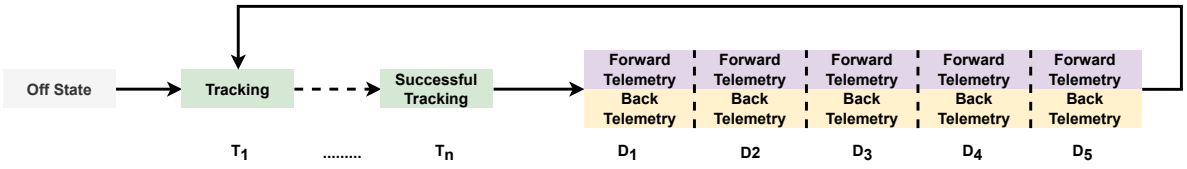

Figure 3.14: A conceptual diagram of the communication protocol.

Ultrasound bursts are sent toward the CMUTs every 2 ms i.e a Pulse Repetition Frequency of 500 Hz is maintained. Every burst travels towards the CMUTs and gets reflected back towards the probe. This echo is again sensed by the probe. In this protocol, two bursts are grouped together to form a single word. The first burst is called the command burst and the second burst is called the function burst. The command burst is used to set the state of the microcontroller (MC) and the function burst is used to perform the action corresponding to that particular state. Ultrasound bursts traveling inside a human body are often distorted and attenuated due to reflectors and multi-path effect (Sec 3.2) especially when it is assumed that the implants are moving. By using the difference between two consecutive bursts separated by a small time interval (in this work 2 ms), the influence of transducer offsets and distortion can be avoided. This difference between the command burst echo and the function burst echo is utilized in Tracking and Back Telemetry as discussed in the further sections. Similar to the functions performed by this circuit, the microcontroller also has three states: tracking state, forward telemetry and back telemetry. The following sub-sections describe these states and the protocol in more detail.

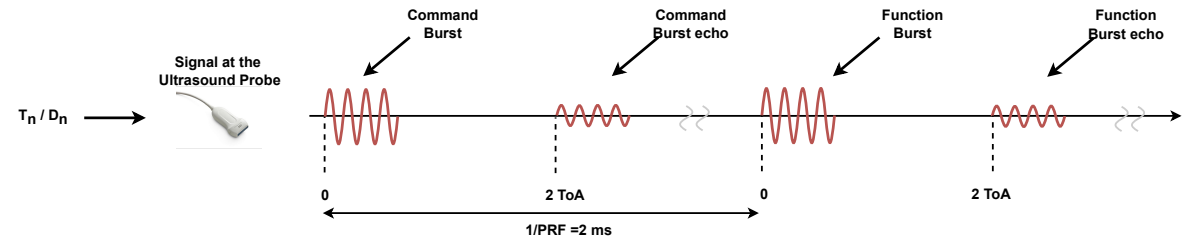

Figure 3.15: Two ultrasound bursts forming a single word of the communication protocol.

Table 3.1: Summary of the logic implemented by the Microcontroller.

Input signals			Condition	Decision (D)/Action (A)	Output signals	
q_track	**demod**	**nr. cycles**			**sw**	**LED**
0 (odd burst)	No Modulation	24	∼(does not matter)	D - PWM modulation of the next burst for Tracking State (T.S.) =>T.S. = 1	0	∼
0 (odd burst)	No Modulation	128	∼(does not matter)	D - ASK modulation of next burst for Back Telemetry (B.T.) =>B.T. = 1	0	∼
0 (odd burst)	Pulse Position Modulation	128	∼(does not matter)	A - Decode the Forward Telemetry (F.T.) data bits using the Amplitude Demodulator =>F.T. = 1	0	∼
1 (even burst)	∼(does not matter)	24	T.S. = 1	A - The variable delay element produces the track_out signal which is delayed proportional to the storage voltage capacitor	track_out (output of the variable delay element)	∼
1 (even burst)	∼(does not matter)	128	B.T. = 1	A - The Microcontroller turns on the switch to transmit data serially as discussed in the communication protocol section	Back Telemetry Data bits B0 to B7	∼
1 (even burst)	∼(does not matter)	128	F.T. = 1	The Micrcontroller turns on the LEDs to display the Forward Telemetry data bits	0	Turns on LEDs to indicate the decoded F.T. bit stream

3.4.1. States of the Microcontroller

As mentioned in the previous section, a total of 19 pins are used by the MC of which 4 pins produce output signals, 2 pins supply power to the ICs and the rest of the pins are the input to the MC from the rest of the circuit. Table 3.1 shows a summary of the logic implemented by the MC. The input signal *q_track* as mentioned previously is low for odd bursts and high for even bursts (Fig 3.9b). The *demod* signal is the output of the amplitude demodulator (Sec 3.3). This *demod* signal contains a train of pulses when the command burst is modulated to perform Forward Telemetry using PPM. The input signal *nr. cycles* is the output of the counter indicating the width of the US burst received by the CMUTs. The MC changes its state based on the command burst. If the command (odd) burst contains 24 cycles, the circuit performs pulse width modulation of the function (even) burst for tracking. If the command burst contains 128 cycles, ASK of the function burst is implemented to perform Back Telemetry. If the command burst is modulated based on Forward Telemetry data bits, the MC stores these data bits and turns on the LEDs indicating the decoded bit stream during the function burst.

As mentioned previously, the protocol essentially performs three functions: Tracking, Back Telemetry & Forward Telemetry. The MC used in the circuit acts as the brain to decide when to perform one of the above mentioned functions. Accordingly, three states of the MC are defined below that explain how the communication protocol works.

Tracking State:

As mentioned earlier, the state of the microcontroller is set by the command burst. Figure 3.16 shows a time sequence demonstrating how the tracking state of the MC is set by the Verasonics system. At the beginning, the Verasonics system generates a 24-cycle, 4 MHz ultrasound burst using the probe. This ultrasound beam is initially focused away from the CMUT drums since its current location is not known yet. The focus point is moved around the coordinate system (Sec 2.8) for tracking the implant. When the CMUT drums start harvesting enough power, the implant starts counting the number of cycles using the 7-bit synchronous up-counter. The ultrasound burst arrives at the CMUTs after 1 ToA (Time of Arrival). The counter counts more than 18 cycles (for a 24-cycle burst) and this makes the microcontroller switch to the Tracking state. Meanwhile, the backscattered US burst reaches the US probe after 2 ToA, which is indicated by a low amplitude signal in the figure.

Go to ToC

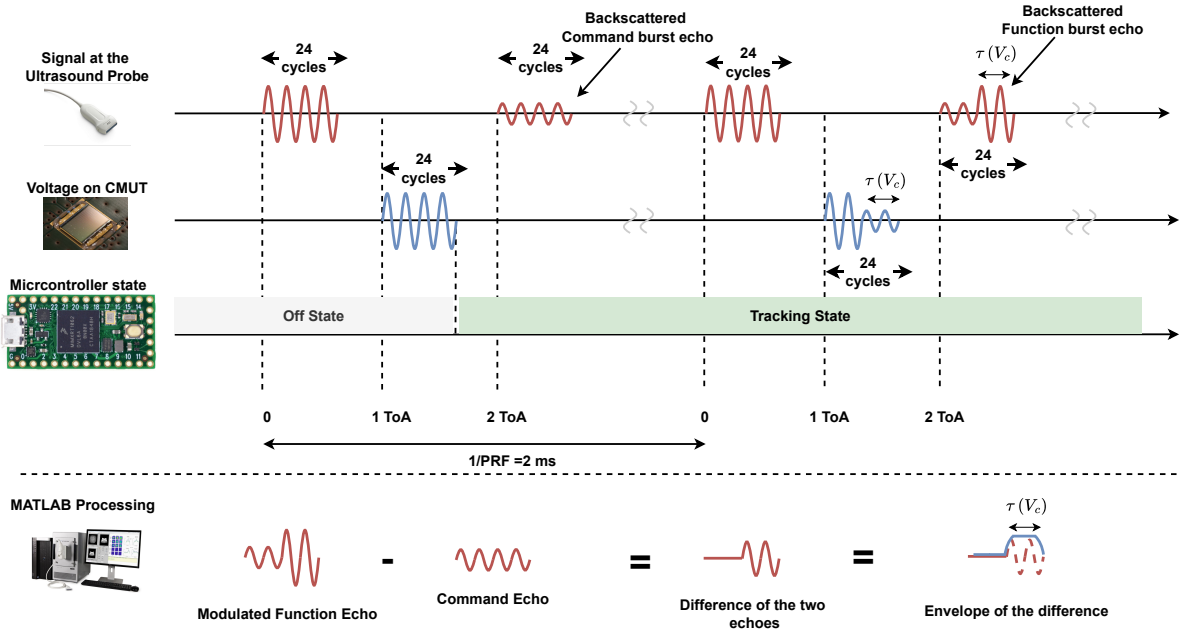

Figure 3.16: Tracking state of the implant.

After 2 ms, the second ultrasound burst is transmitted toward the CMUT drums. This second burst is modulated proportional to the power harvested by the CMUT drums ($\tau(v_c)$, refer Sec 2.6). The modulated backscattered burst now travels back and reaches the probe after 2 ToA. On the Verasonics side, the command burst echo and the function burst echo are recorded. These two echos are subtracted from each other and the envelope of this difference is derived on MATLAB. As shown in the figure, the width of this envelope is directly proportional to the power harvested by the CMUT drums. This modulated burst width is used in the tracking of the CMUTs as discussed in Section 2.8.

Back Telemetry:

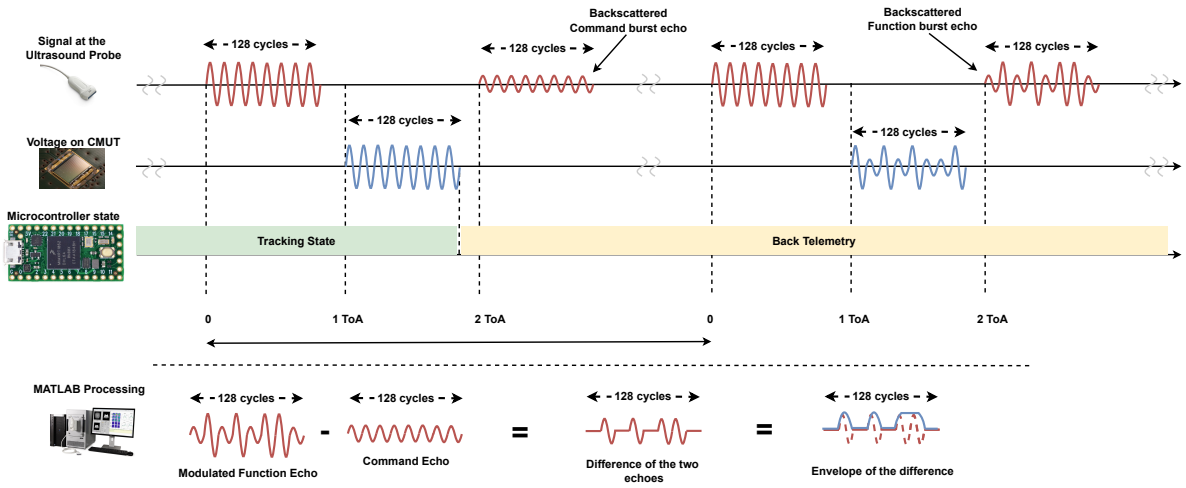

Figure 3.17: Tracking state to Back Telemetry.

Figure 3.17 shows another time sequence demonstrating how the microcontroller's state changes from Tracking to Back Telemetry. This state change is achieved by sending 128 cycles in a single ultrasound burst. When the counter counts more than 122 cycles in the US burst, the MC changes its state to Back Telemetry i.e. to modulate every second burst based on the bit stream intended to be transferred. When the CMUTs receive the function burst after 2 ms, the burst is modulated using ASK

for transmitting 8 bits of data. Similar to the Tracking State, the function echo and the command echo are recorded on the Verasonics and the envelope of the difference between these echos is derived to decode the data bits transferred from the CMUTs to the Verasonics.

The CMUTs transmit 8 bits of data every 4 ms. These 8 bits of data are modulated using Manchester data encoding [80]. Figure 3.18 shows an example of Manchester data encoding. The data bit '0' is represented by a falling edge and the data bit '1' is represented by a rising edge. The figure shows the transmission of bitstream '10001000'. Figure 3.19 shows this 8-bit stream transmitting a binary code '10001000'. Manchester data encoding, therefore, transmits data bits in the form of rising and falling edges. In order to decode the bit stream detection of these edges can be performed instead of detecting independent amplitude levels of each data bit that require precise circuit designs. Figure 3.19 shows the modulated function burst used in Back Telemetry. Similar to the Manchester encoded signal, data bit '0' is represented by a decrease in the amplitude of the sinusoidal waves and the bit '1' is represented by an increase in the amplitude of sinusoidal waves. The lower amplitude sinusoidal waves are achieved by closing a switch that is connected across the two terminals of the CMUTs. The US burst incidents on the CMUT drums and the backscattered burst travels back to the probe. When this switch is open the incident sinusoidal waves are rectified to store the harvested energy. Hence, this type of encoding allows the circuit to utilize the power harvested during the communication. When transmitting any bit stream combination, harvested energy from the high amplitude sinusoidal waves is stored in the storage capacitor (V_c). This energy can be used to turn on the switch connected across the CMUT terminals.

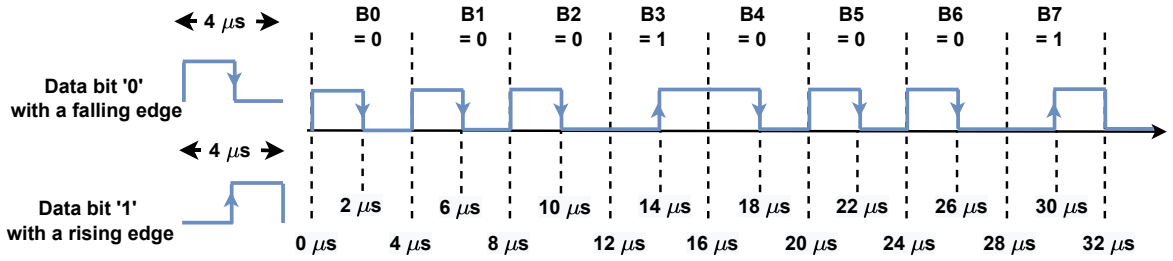

Figure 3.18: Example of Manchester data encoding used to transmit an 8-bit stream of '10001000'.

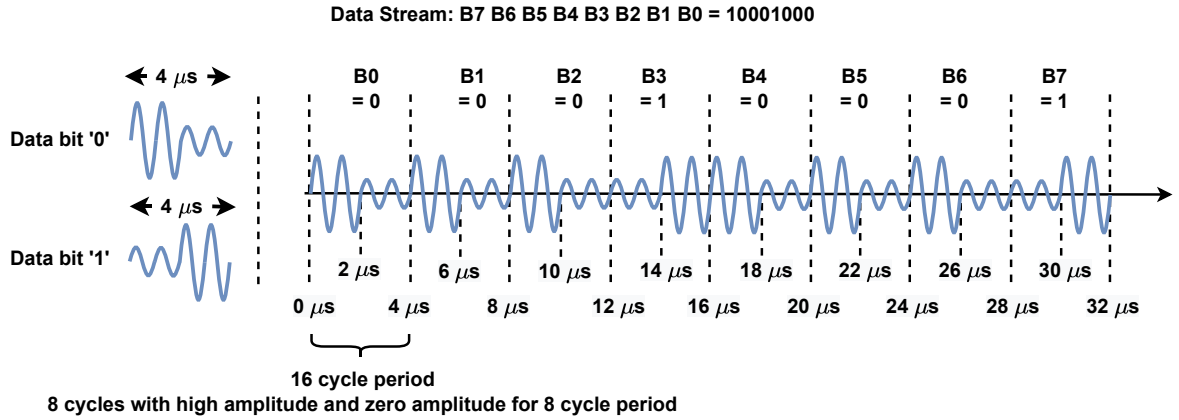

Figure 3.19: Example of a bit stream encoding in a single ultrasound burst using manchester line coding and .

The digital envelope of the burst *env_clk* signal is high when the CMUTs receive an ultrasound burst. The proposed circuit performs all the operations when this signal is high. In case a bit stream with the data bit 'B0' equal to '1' is to be transferred to the external transmitter, the CMUTs are shorted for the first 8 cycles (2 µs) of the burst. In this case, the envelope will not be detected until the very next 8 cycles of the burst, ultimately the counter will not count the first 8 cycles. Hence the bit '0' is always fixed as the starting bit for the 8-bit stream transferred to the Verasonics system. Figure 3.20 shows

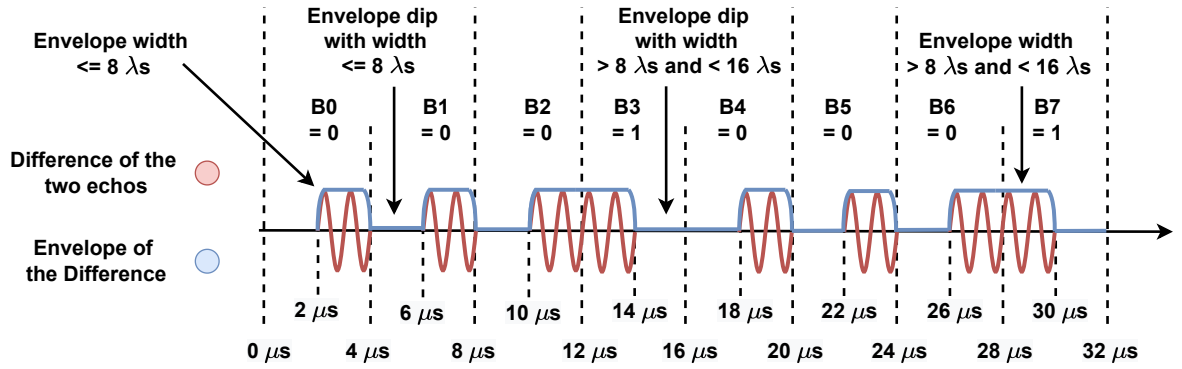

Figure 3.20: A depiction of the envelope and difference of two consecutive echos for a bit stream of '10001000'.

the envelope and the difference of the command and function echos received by the probe. From this figure following two points can be noted:

1. For the data bit pairs of '00' & '11', an envelope dip of width less than or equal to 8 cycles (or wavelengths) is present between two envelopes of width less than or equal to 8 cycles (or wavelengths).
2. For a data bit pair of '01', the envelope width will be greater than 8 cycles (or wavelengths) and less than 16 cycles (or wavelengths).
3. For a data bit pair of '10', a dip in the envelope can be seen. The width of this dip will be greater than 8 cycles (or wavelengths) and less than 16 cycles (or wavelengths).

Since the starting bit is always '0', based on the above bit pair information, modulated backscattered US bursts can be decoded to derive the bit stream on MATLAB. This is discussed further in Section 3.6.

Forward Telemetry:

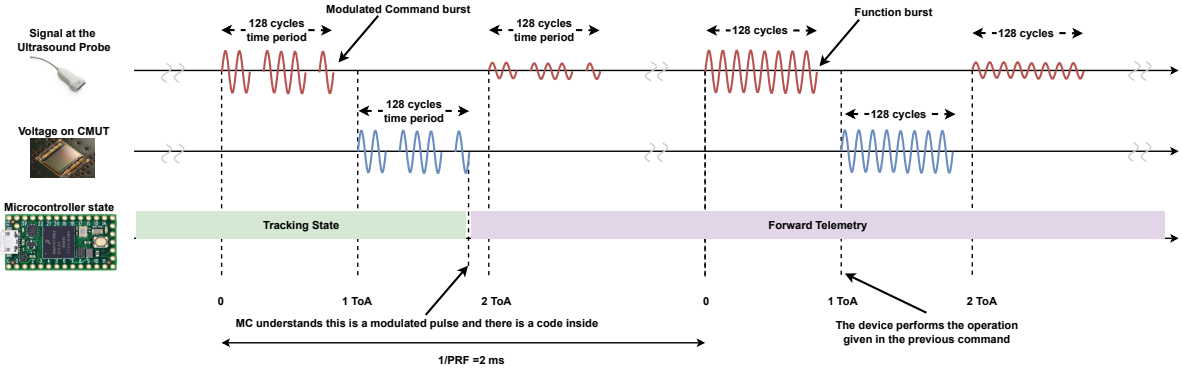

Figure 3.21: Tracking state to Forward Telemetry.

Figure 3.21 shows the change of MC state from Tracking to Forward Telemetry. The figure shows a modulated command burst received by the CMUTs. When the CMUTs receive this modulated burst, the amplitude demodulator (Sec 3.3) converts the demodulated wave into a train of pulses (demod signal). When the MC receives this train of pulses (*demod* signal), it switches to Forward Telemetry (sec 3.4.1). The encoded bit stream is simultaneously decoded by the MC and stores the bit values till the end of the function (next) burst.

Pulse position modulation is used in this protocol to transmit data in Forward Telemetry (sec 3.2). The modulation of the command burst is shown in Figure 3.22. The figure shows a modulated burst of 45 µs representing a bit stream of '00110101'. Data bit '1' is represented with a 4 MHz sinusoidal burst

of length 8 µs with an intermission of 4 µs (16 cycles). Data bit '0' is represented by a sinusoidal burst of 4 µs (16 cycles). In this type of modulation, the position of this intermission (bit '1') determines its bit place value i.e. B0, B1, ... B7. This is further discussed in Section 3.5. Similar to Back Telemetry a total of 8 bits of data is transmitted every 4 ms.

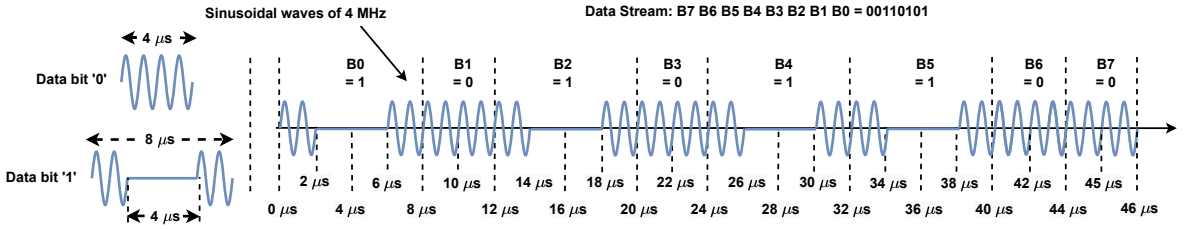

Figure 3.22: Forward telemetry encoding of data bits using Pulse Position Modulation (PPM).

As mentioned previously, the decoding of the Forward Telemetry data bits happens during the command burst. The MC controller stores the decoded bit values and turns on the LEDs during the function burst indicating the decoded bit stream. This transfer of data, from Verasonics (external transmitter) to CMUTs, is demonstrated by using 4 LEDs on the board (3 external LEDs and 1 LED on the microcontroller). This feature in the protocol is intended to show that an implant can implement forward telemetry during the command burst and use the power harvested during the function burst to perform various functions such as stimulating current generation or recording the body's vitals based on the data received from the outside world.

3.4.2. Synopsis of the Protocol and the Circuit

Figure 3.23 shows a flowchart that summarizes the working of the circuit and the protocol. It demonstrates the working of the circuit designed in this work while explaining how various signals are generated in the circuit and used by the MC. The flowchart starts with the Max power transfer inductor and resistor (Sec 3.3). The clock recovery circuit and the counter produce the number of cycles signal (Sec 3.3). The amplitude demodulator produces the train of pulses indicating the Forward Telemetry data bits (Sec 3.3 & 3.4.1). The tracking part implements the PWM protocol [23] and produces the track_out and q_track signal (Sec 3.3). The MC in the end is programmed to implement the logic represented by Table 3.1 (Sec 3.3). Hence MC outputs the sw signal to implement Back Telemetry and Tracking of the CMUTs (Sec 3.4.1 & 3.3) and turns on the LEDs indicating the decoded Forward Telemetry bit stream.

3.5. Simulation Results

Rectification, envelope detection, clock recovery and storage capacitor:

As mentioned in Section 1.2.2, CMUTs can be compensated using a matching inductor and by operating at its resonance frequency. Figure 1.4 shows this compensated CMUT which is essentially a voltage source (V_s) in series with an internal damping resistance (R_m) without the load resistor. This compensated CMUT element is used as the source of the ultrasound bursts in the following simulations. Figure 3.24 shows the schematic diagram of the compensated CMUT element as the voltage source and a series resistor of 300 Ω (the matching R_{load} value from Section 3.3). In the rectification and envelope detection block, two full bridge rectifiers (using BAT54 Schottky diodes) connect this CMUT to an envelope detector and a storage capacitor of 1 nF. The envelope detector uses a resistor of 30 kΩ and 270 pF. These R and C values amount to a discharging time constant (τ) of 8.10 µs. A voltage source of 3.3 V (node V_{cc}) is used to power the comparator ICs in the simulations. This is equivalent to 3.3 V pin of the MC that is used to power all the ICs in this circuit.

The storage capacitor block contains a current source of 0.5 µA connected in parallel to the storage capacitor to simulate the discharge of the capacitor through the rest of the circuit when CMUTs do not receive any ultrasound burst. In the clock recovery block, a comparator with hysteresis is simulated using the model of LTC6752. The positive terminal of the CMUT (ac+) is the input for the comparator producing the clock. The resistor divider consisting of 30 kΩ and 1kΩ form the reference voltage for the comparator and another resistor of 30 kΩ is the feedback resistor for external hysteresis. This resistor combination adds two threshold voltages at V_{th} = 0.2 V and V_{tl} = 0.1 V. In the digital envelope signal

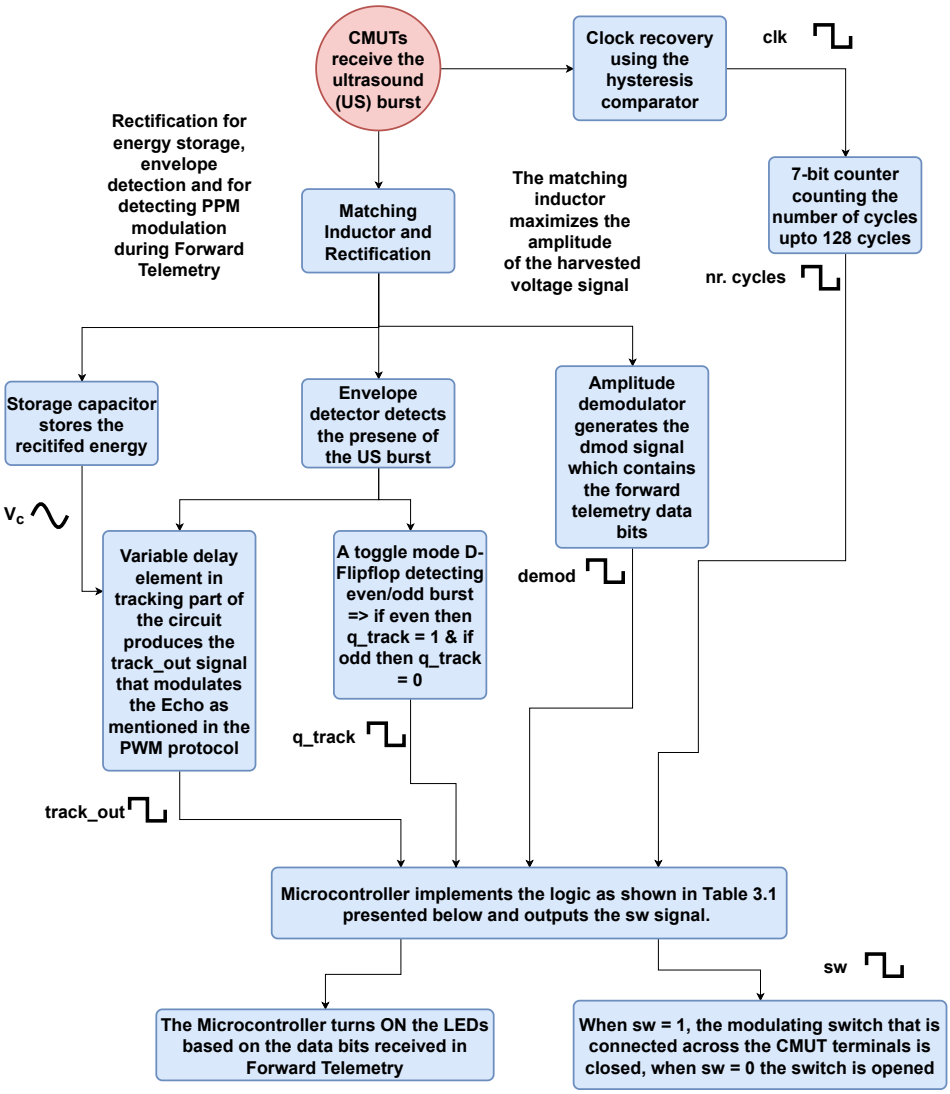

Figure 3.23: Flowchart depicting how the various signals are produced in the circuit.

block, the envelope signal *v_env_clr* is connected to the input of the comparator that produces the digital envelope signal *env_clk*. Similar to the clock generator, the resistor divider consisting of 9.09 kΩ and 1 kΩ forms the reference voltage for the comparator and another 9.09 kΩ operates as the feedback resistor for the external hysteresis. This resistor combination adds two threshold voltages at V_{th} = 0.6 V and V_{tl} = 0.3 V.

Figure 3.25 shows the waveforms of different voltage nodes when the CMUTs receive a 24 cycle ultrasound burst. It can be observed here that the *env_clk* signal goes high during the start of the burst and goes low only after a certain period of time after the end of the burst. This extra time period for settling down is given to make sure that *env_clk* does not go low during the modulation of the burst during tracking or back telemetry.

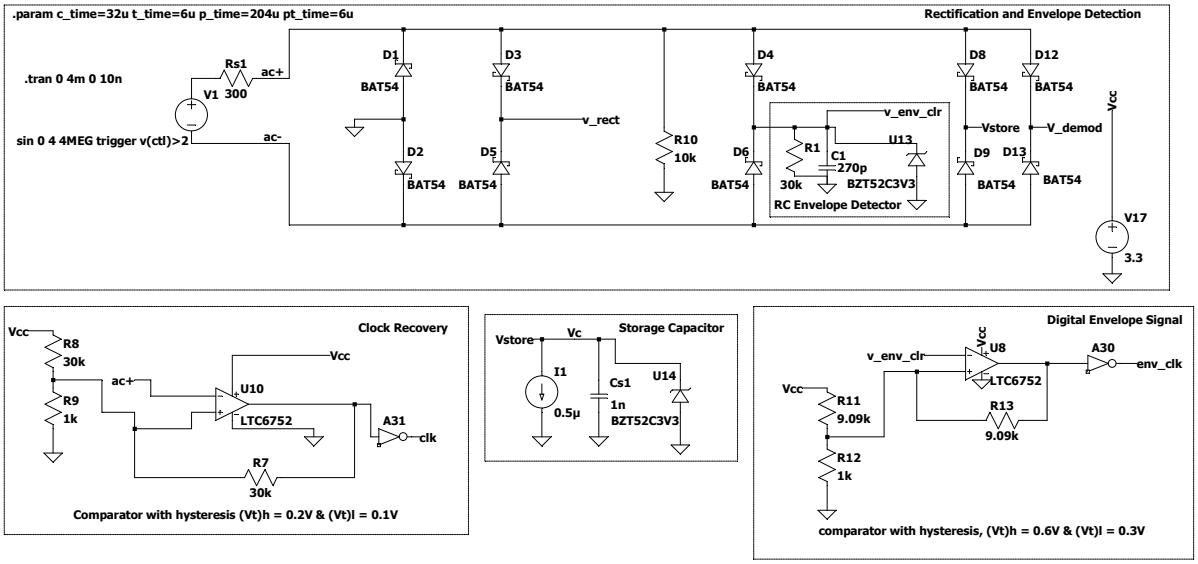

Figure 3.24: LT spice schematic presenting the envelope detector, storage capacitor and the clock recovery circuit discussed in Section 3.3.

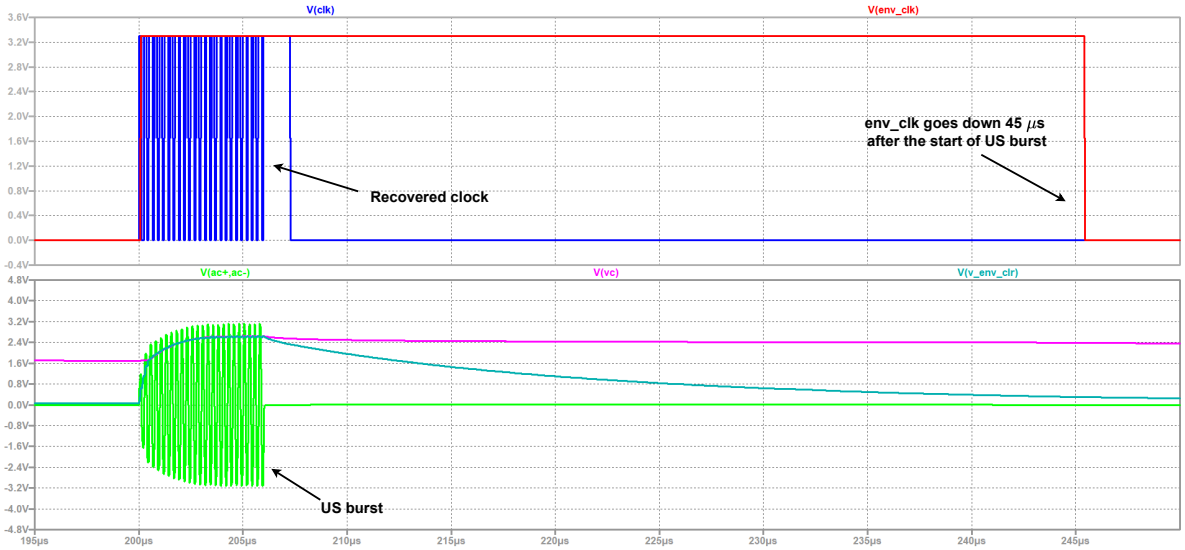

Figure 3.25: Simulating the case where the CMUTs receive a 24 cycle ultrasound burst. Waveforms of the signal nodes vstore, v_env_clr, clk, env_clk and the voltage across the source(ac+,ac-).

Counter:

Figure 3.26 shows the schematic diagram of the 7-bit synchronous up counter. In this schematic, a D Flip-Flop together with a single XOR gate is used as a T flip-flop for the counter. As mentioned in Section 3.3 the clear input of all the flip-flops is connected to the *env_clk* signal to clear the counter when the CMUTs do not receive any ultrasound burst. Additionally, the figure also consists of a logic circuit using 3 AND gates in the right bottom corner. This logic is used to disable the clock input after the counter counts 128 cycles. This is done to ensure that the counter does not start counting from zero in between the burst. The counter output can be seen in Fig 3.27 when the compensated CMUT source generated 24 cycles.

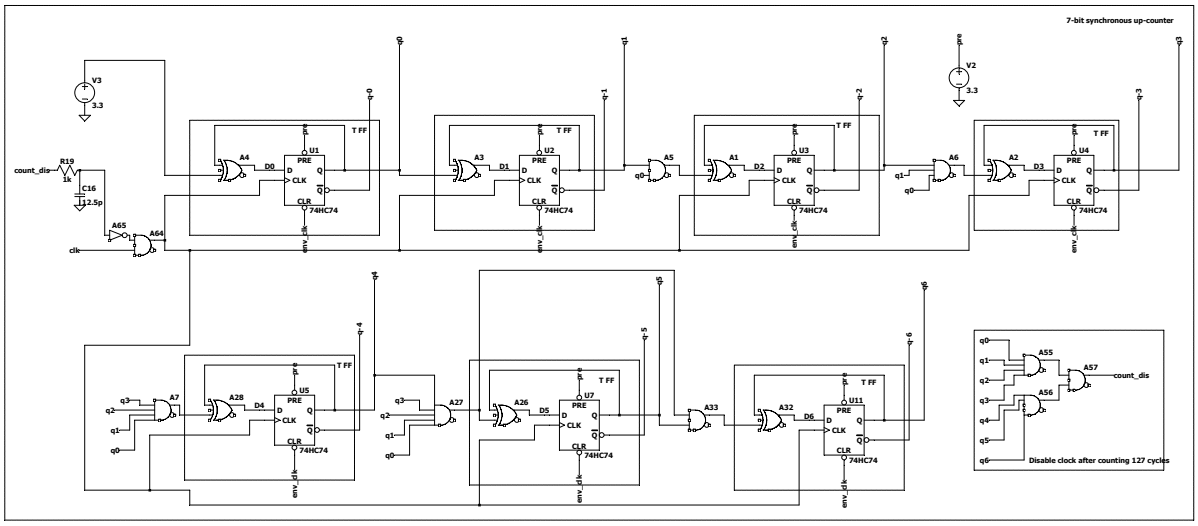

Figure 3.26: Schematic of the 7-bit synchronous up-counter using T Flip-flops.

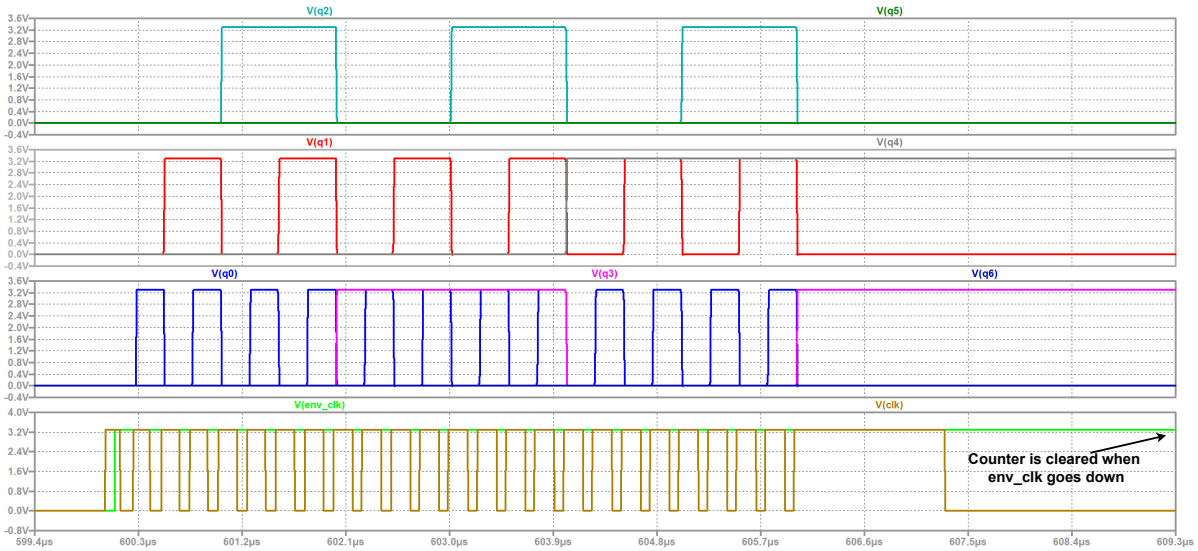

Figure 3.27: Output of the counter when simulating the CMUTs harvesting a 24 cycle burst.

State Selection (Back Telemetry & Tracking):

The change in the state from tracking to back telemetry takes place when a 128-cycle burst is sent to the CMUTs in the command burst. This logic is implemented using the output of the counters and a D flip-flop as shown in Fig 3.28. Node *a* goes high when the counter counts 18 or 19 cycles and node *b* goes high when the counter counts 122 or 123 cycles. The node *a* is connected to the input of a D flip-flop to remember this state of the circuit for the next burst. The clock for this flip-flop is produced by the signal *a* itself by adding an RC delay element of 12.5 ns. Therefore the output of this flip-flop *ff_out* goes high slightly after node a goes high. The node *qa* is a replica of *ff_out* with a delay of 32 µs. The circuit operates in a Tracking state when the node *qa* is high and in Back Telemetry when the node *qa* is low. When there are only 24 cycles in the input generated burst, node *qa* goes high and when there are 128 cycles node *qa* goes low. This way the number of cycles in the command burst and the node *qa* decide to initiate either the Tracking state or Back Telemetry state. This state change is demonstrated by the waveforms in Figures 3.29 and 3.30.

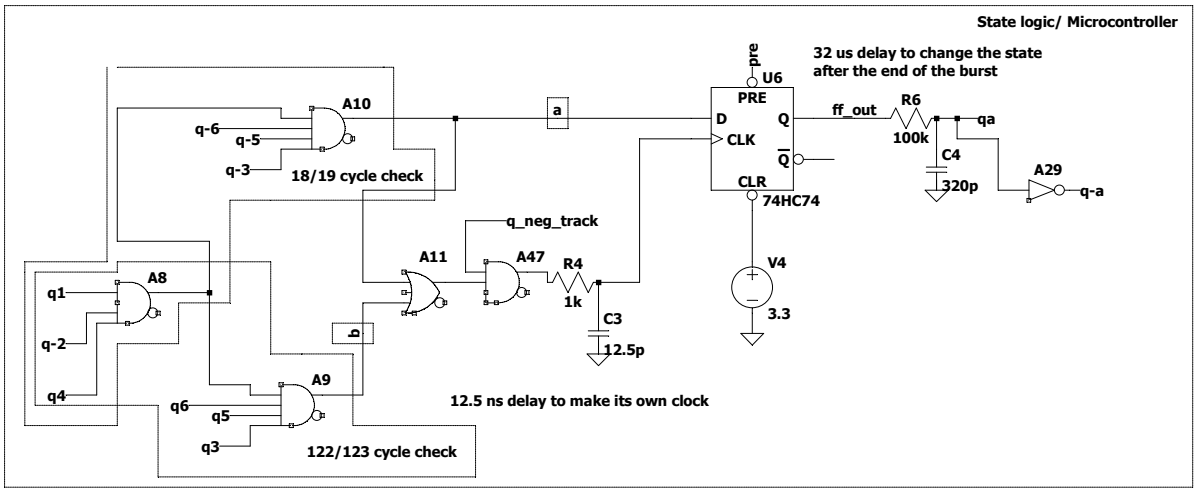

Figure 3.28: Logic circuit that decides the states between Tracking state and Back Telemetry state.

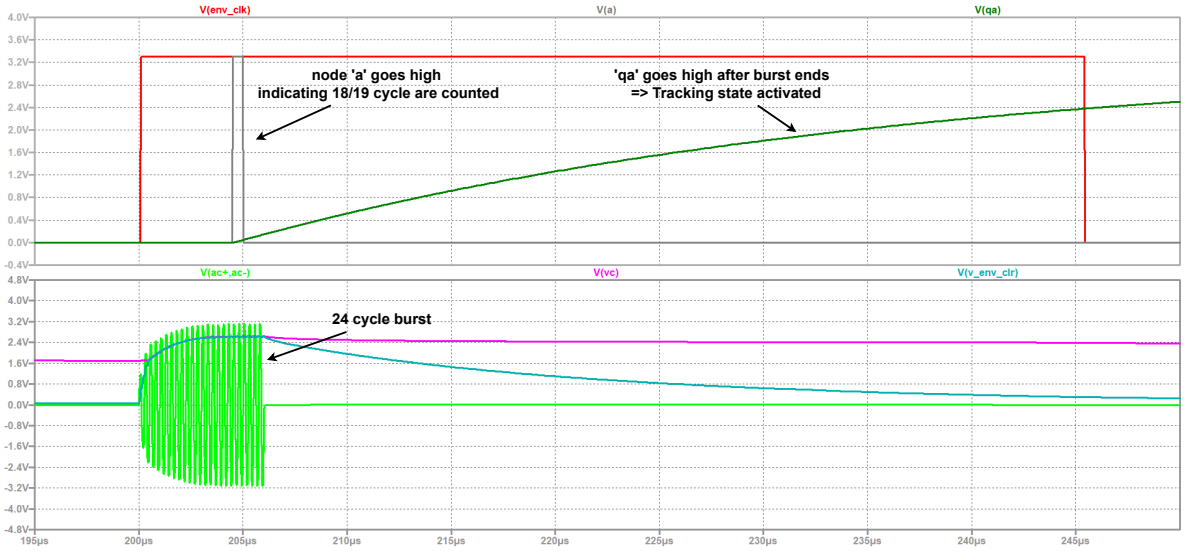

Figure 3.29: Initiation of Tracking state.

Go to ToC

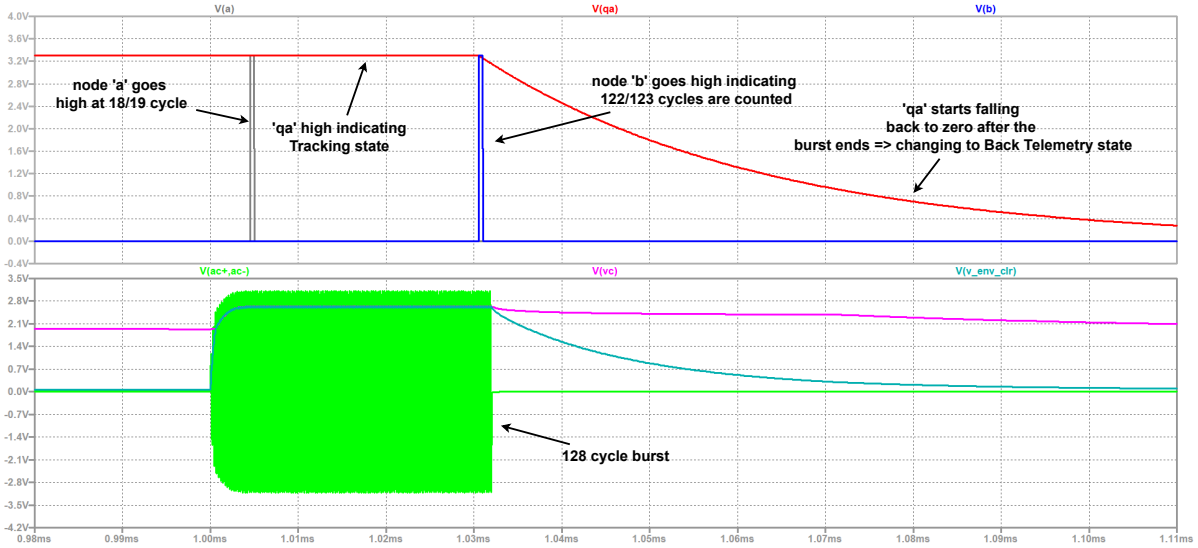

Figure 3.30: Initiation of Back Telemetry state.

Tracking circuit:

Figure 3.31 shows the LT spice schematic diagram of the tracking part of the circuit. The burst amplitude-dependent delay-producing RC element uses a 100 kΩ resistance and a 300 pF capacitor. This capacitor is in series with the parallel combination of the two varactor diodes (BB202). The varactor diodes are biased with the storage capacitor voltage using another resistance of 100 kΩ. The capacitance of a single varactor diode varies from 20 pF to 5 pF, hence the parallel combination's capacitance varies from 40 pF to 10pF when the bias voltage varies from 1 V to 4 V (Fig 3.32). Since the capacitance of the varactor diode is much less than 300 pF which is in series with the diode, the capacitance of the series combination depends on the capacitance of the varactor diode. This implies the time delay τ produced varies from 4 µs ((100 * 10^3 Ω) * (40 * 10^{-12} F)) to 1 µs ((100 * 10^3 Ω) * (10 * 10^{-12} F)).

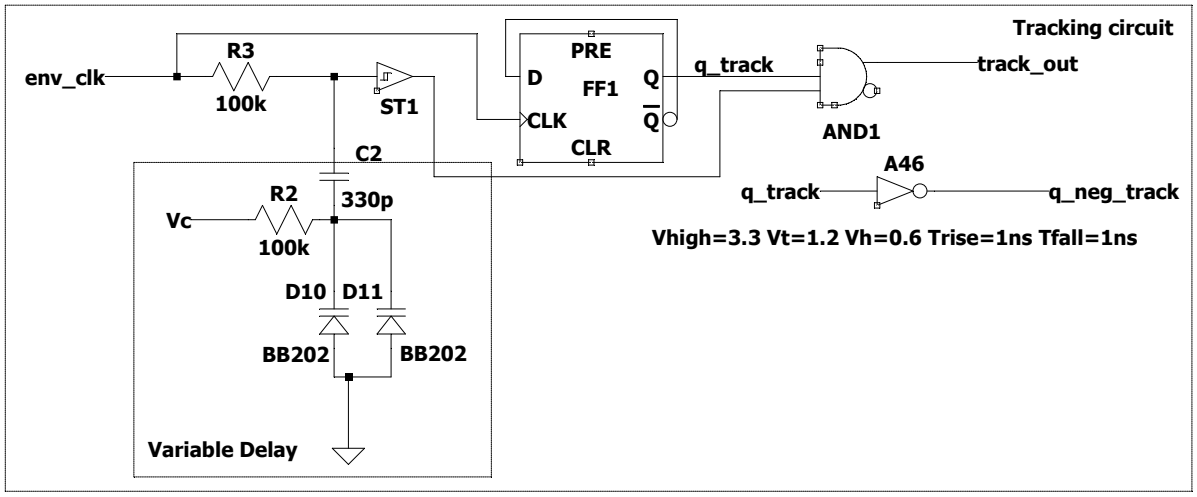

Figure 3.31: Schematic of the tracking part of the circuit.

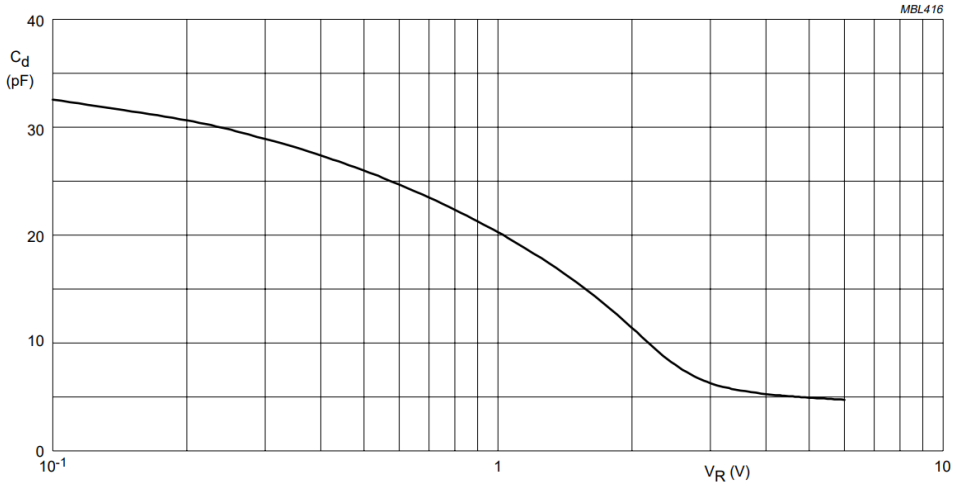

Figure 3.32: Variation of the varactor diode capacitance with respect to its bias voltage [81].

Figure 3.33 shows waveforms of two simulated bursts that are used in the tracking of the CMUTs. The two bursts are separated by a time interval of 200 µs and the amplitude of the second burst is modulated. Figure 3.34 shows this modulated burst and the clock signal extracted from the burst. The clock signal is extracted even when the amplitude of the burst is modulated.

Figure 3.33: Two consecutive bursts implementing Tracking State.

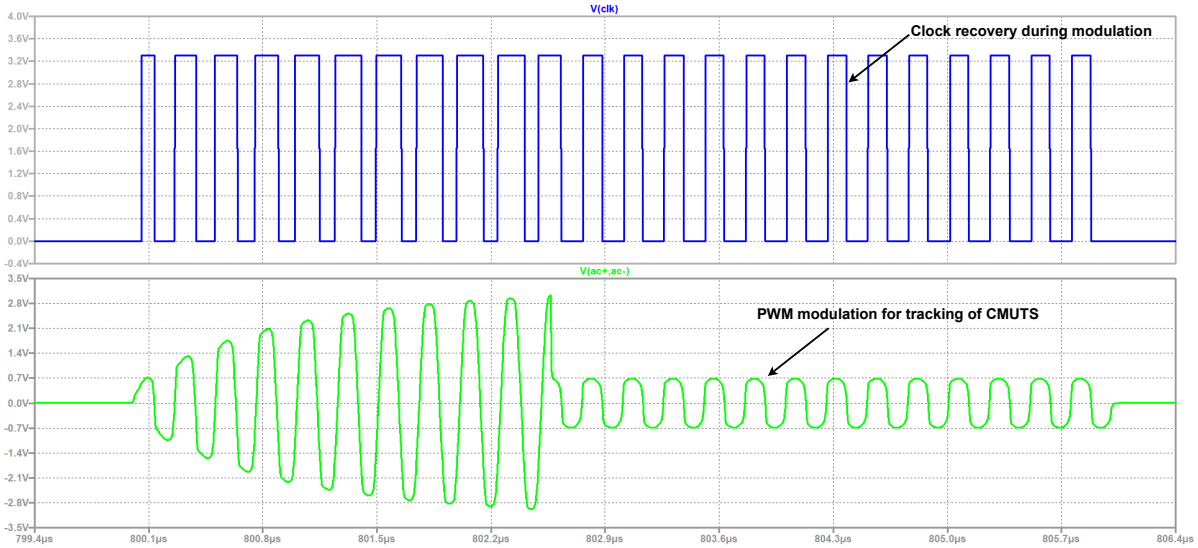

Figure 3.34: Waveform of the modulated burst used in the tracking of CMUTs.

Back Telemetry:
As seen in Fig 3.19, each data bit (Bn) is transmitted for 16 cycles or 4 µs of the ultrasound burst. Each data bit is transmitted at a different instant of time in the total burst period, in other words, the bits are transmitted serially. To achieve this a time-division multiplexer is used in this work. Since a counter is present in the circuit, this time division multiplexing can be implemented using a multiplexer (MUX) with the outputs of the counter connecting directly to its select inputs. Figure 3.36 shows the block diagram of this MUX. The output of the counter (*q6*, *q5*, *q4*, *q3*) is connected to the select inputs. Table 3.2 shows the truth table of the multiplexer that outputs each bit of the data stream (B0, B1, ..., B7) at different instants of the burst period as seen in Figure 3.19. This MUX is implemented using AND gates to produce an output signal *comm_out* (Fig 3.35). This signal *comm_out* is the digital form of the serial 8-bit stream that is transmitted in the Back Telemetry. It is assumed that data is already available as an 8-bit word.

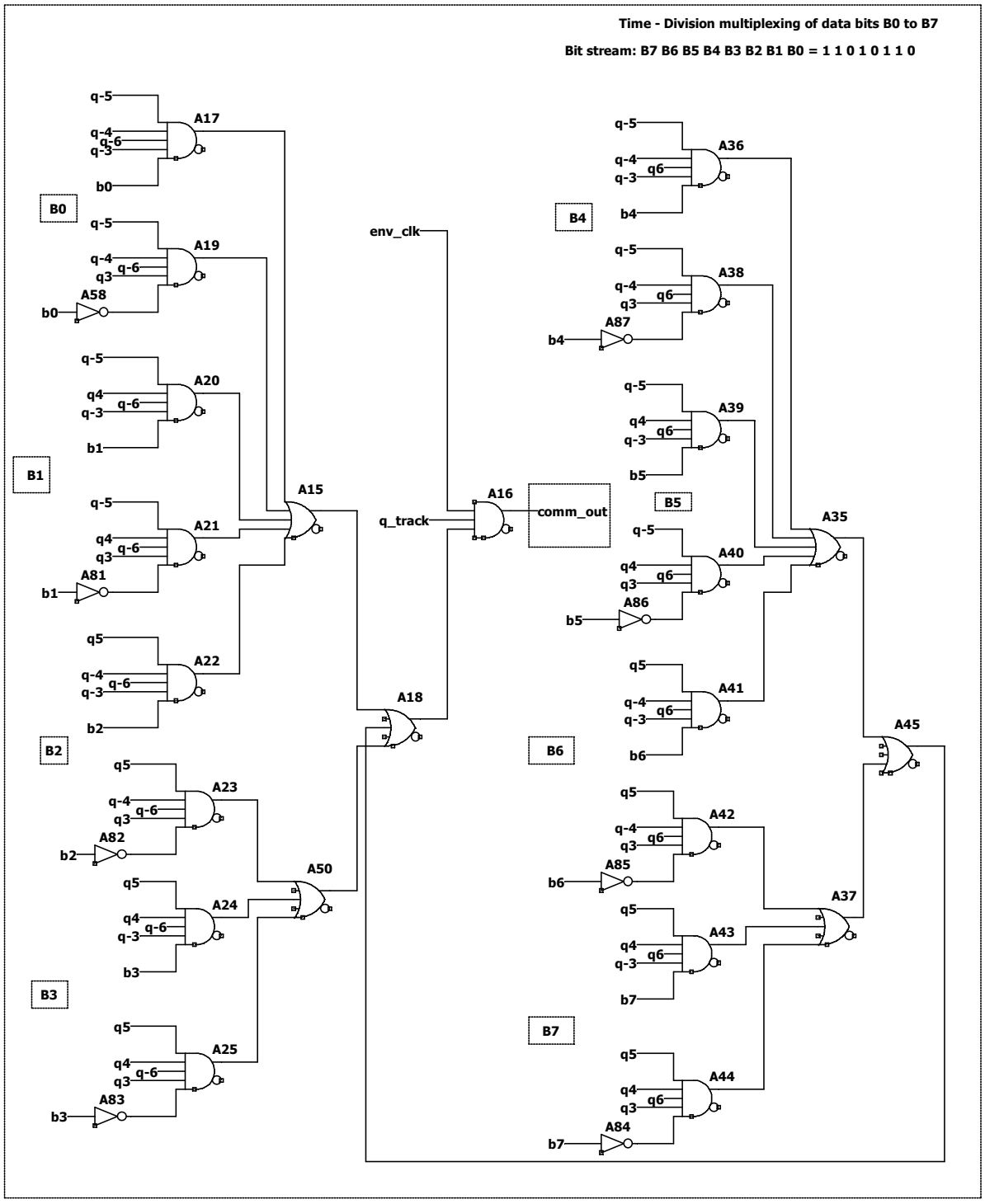

Figure 3.35: Schematic of time multiplexing circuit that multiplexes individual bits as shown in Table 3.2.

Go to ToC

Cycles	MUX Input				MUX Output
	Q6(n)	Q5(n)	Q4(n)	Q3(n)	Comm_out (Bn)
0-7	0	0	0	0	$\overline{B0}$
8-15	0	0	0	1	B0
16-23	0	0	1	0	$\overline{B1}$
24-31	0	0	1	1	B1
32-39	0	1	0	0	$\overline{B2}$
40-47	0	1	0	1	B2
48-55	0	1	1	0	$\overline{B3}$
56-63	0	1	1	1	B3
64-71	1	0	0	0	$\overline{B4}$
72-79	1	0	0	1	B4
80-87	1	0	1	0	$\overline{B5}$
88-95	1	0	1	1	B5
96-103	1	1	0	0	$\overline{B6}$
104-111	1	1	0	1	B6
112-119	1	1	1	0	$\overline{B7}$
120-127	1	1	1	1	B7

Table 3.2: Truth table of the time division multiplexer.

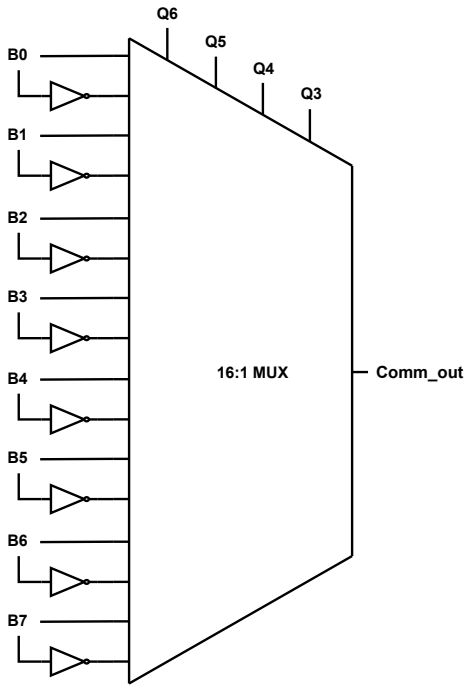

Figure 3.36: MUX implemented by the schematic diagram shown in Fig 3.35.

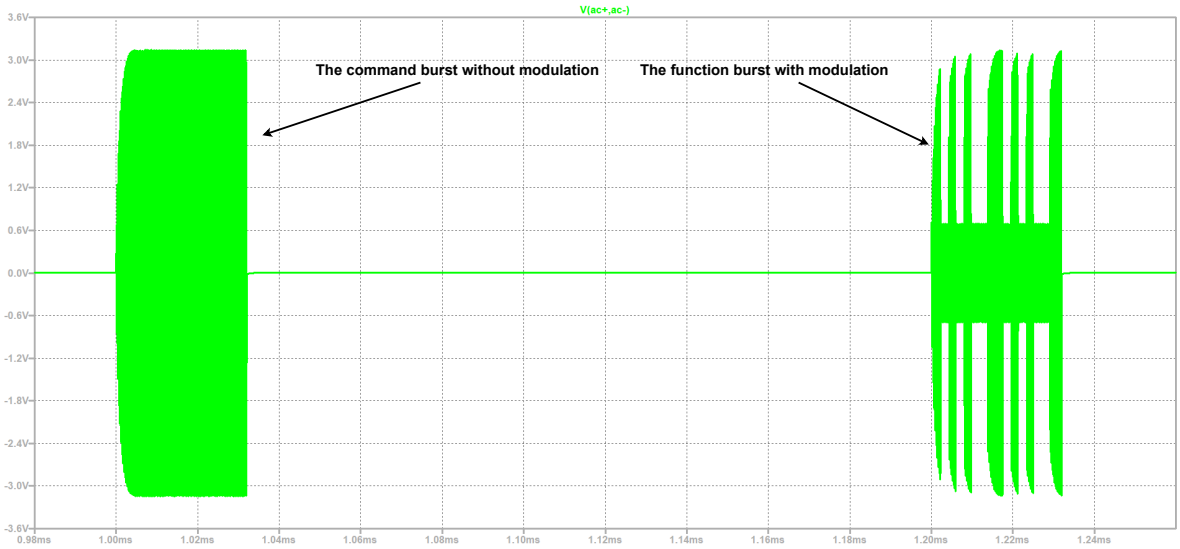

Figure 3.37: Two consecutive bursts implementing Back Telemetry.

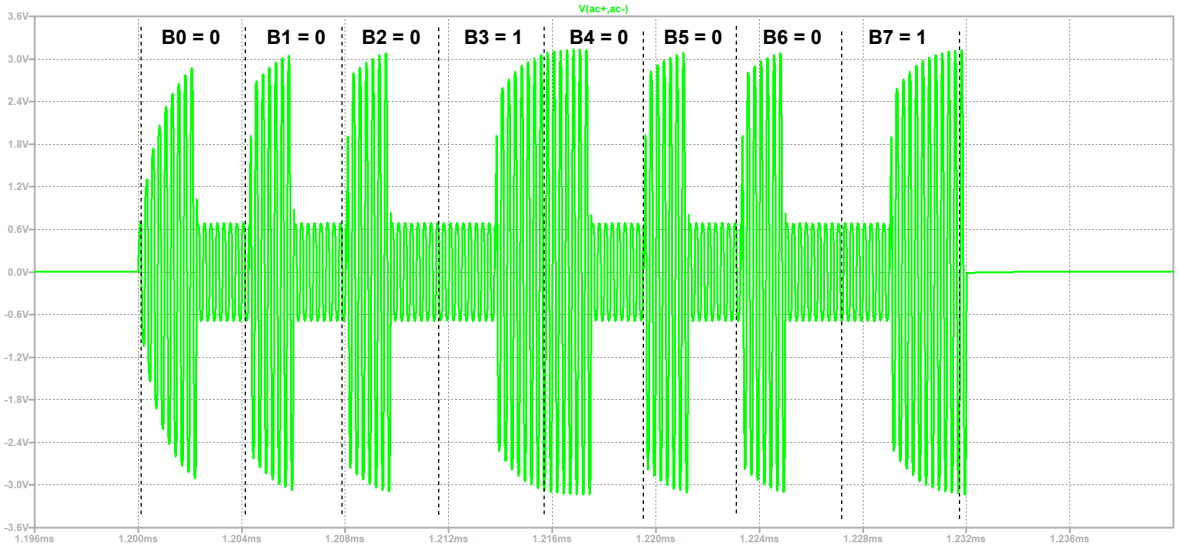

Figure 3.38: Waveform of the function burst transmitting bit stream of'10001000' in Back Telemetry.

Figure 3.37 shows the two bursts that implement Back Telemetry. The first burst is not modulated and the second burst is modulated as discussed in Section 3.4.1. Figure 3.38 shows modulation US burst that is used to transmit a bit stream of '10001000' (similar to Fig 3.19). The figure also demonstrates how each data bit (B0, B1, ..., B7) is transmitted serially (time multiplexed).

State Selection (Forward Telemetry):
Figure 3.39 shows the logic circuit that initiates the Forward Telemetry state. This logic circuit implements the detection of a second rising edge. When CMUTs receive an un-modulated US burst, the *demod* signal has only a single rising edge at the end of the burst as shown in Figure 3.40. However, when the CMUTs receive a modulated US burst, which contains the Forward Telemetry data bits, the *demod* signal contains more than one rising edge i.e. a train of pulses as shown in Figure 3.42. This logic is used to change the state of the MC to Forward Telemetry State. The first D Flip-Flop in Figure 3.39 detects the first rising edge and the second D Flip-Flop detects the second rising edge. These Flip-Flops are cleared when the burst ends using the *env_clk* signal. The node *q_demod* goes high after the burst ends when the *demod* signal contains more than one rising edge i.e. when the CMUTs receive a PPM modulated US burst used for Forward Telemetry.

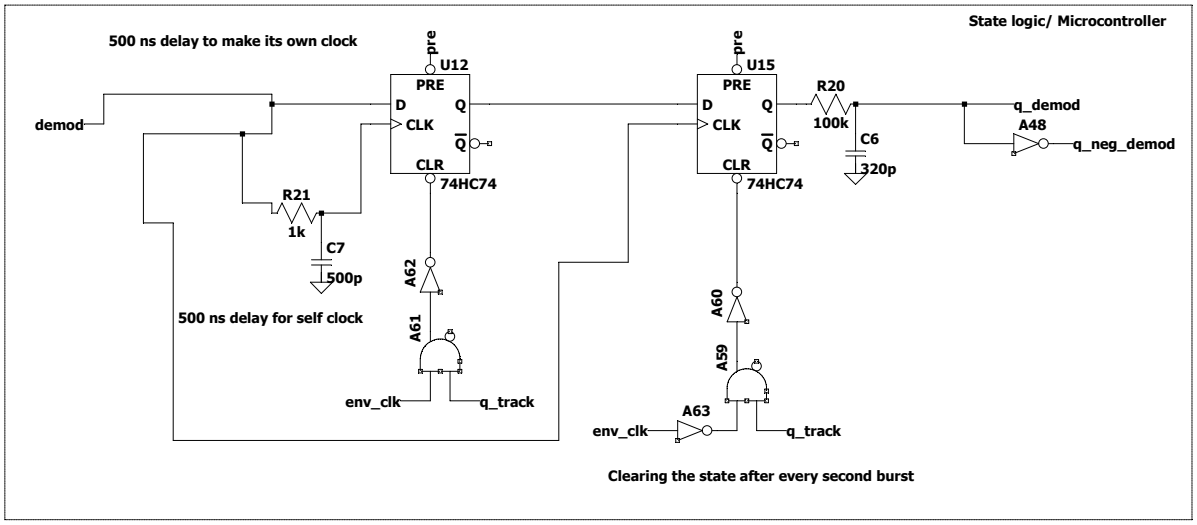

Figure 3.39: Logic circuit that initiates the Forward Telemetry state.

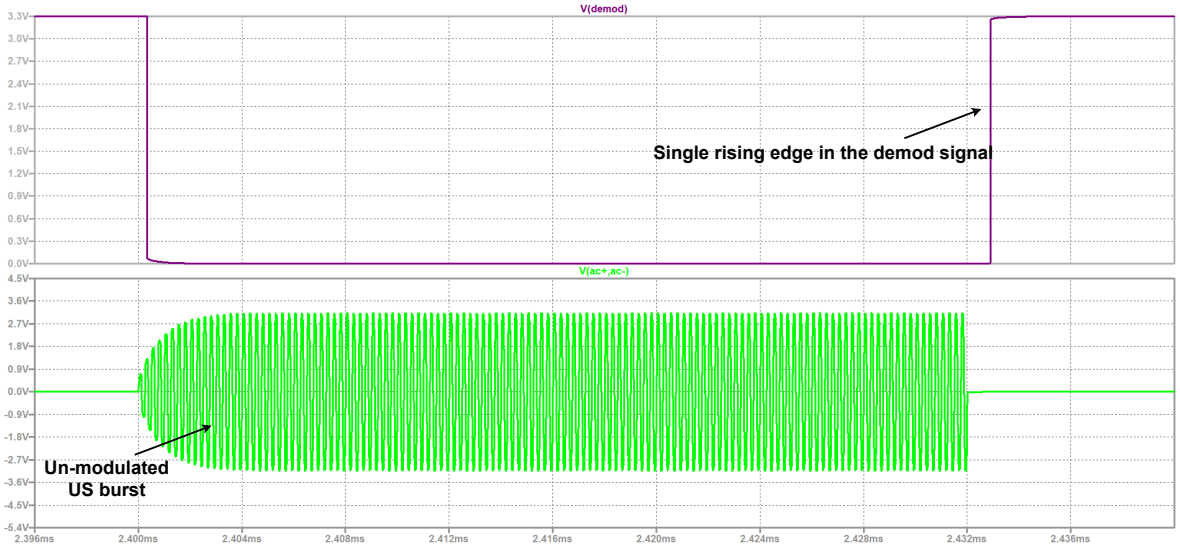

Figure 3.40: Waveform depicting a single rise edge in the demod signal when CMUTs receive an un-modulated US burst signal.

Forward Telemetry:

Figure 3.41 shows the amplitude demodulation circuit used to decode the Forward Telemetry data bit stream. As mentioned in Section 3.4.1, data bit '1' is represented with a 4 MHz sinusoidal burst of length 8 µs with an intermission of 4 µs (16 cycles). Data bit '0' is represented by a sinusoidal burst of 4 µs (16 cycles). The output of the demodulator circuit (signal *demod*) is shown in Figure 3.42. The pulses with an amplitude of 3.3V represent this decoded bit '1'. It can be seen in the figure that when a bit '1' is transmitted, there is an intermission in the US burst. During this intermission, no clock can be recovered and the counter stops counting the number of cycles. During this intermission, the output of the counter is equal to the position of the pulse in the demod signal. This position of the pulse determines its place value as shown in Table 3.3. Building up on this, an 8-bit register stack is simulated using 8 D Flip-Flops along with a DEMUX that implements the above mentioned truth table as shown in Figure 3.43. The DEMUX implemented using AND gates assign the place value for the decoded bits '1' present in the demod signal. The Flip-Flops remember these values until the end of the next burst as shown in Figure 3.44. This is how Forward Telemetry is implemented.

This section has presented various simulation results of the circuit developed to implement tracking, back telemetry and forward telemetry using CMUTs. The State Selection (Tracking, Back Telemetry & Forward Telemetry, Sec 3.5 & Sec 3.5) circuit, the Time MUX circuit (Fig 3.36) and the register stack (Fig3.43) circuit simulated using LT Spice can be practically implemented using a Microcontroller since these parts of the circuit implementing digital logic. In the next section, this protocol is implemented using Teensy Microcontroller as discussed in Section 3.3.

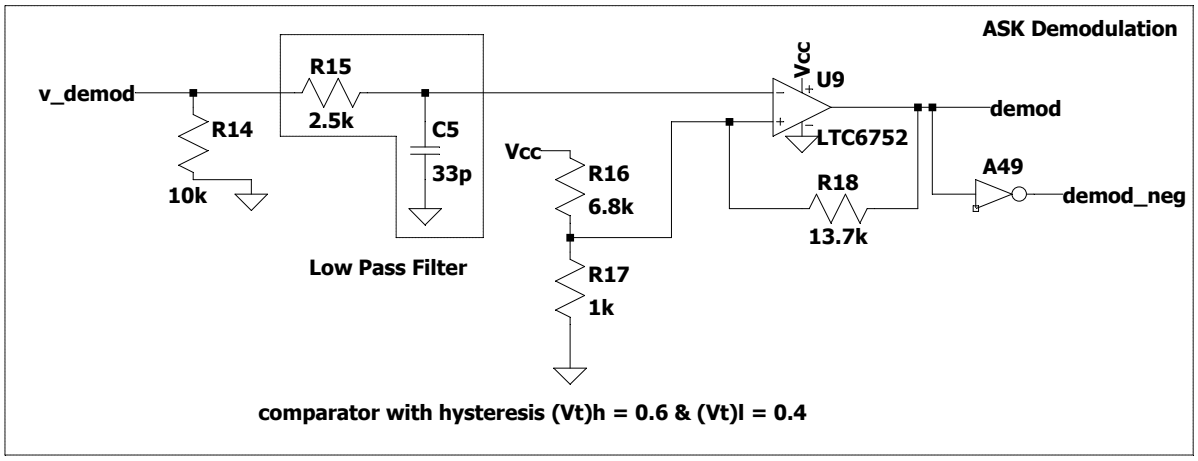

Figure 3.41: Amplitude demodulation circuit used to decode Forward Telemetry data bit stream.

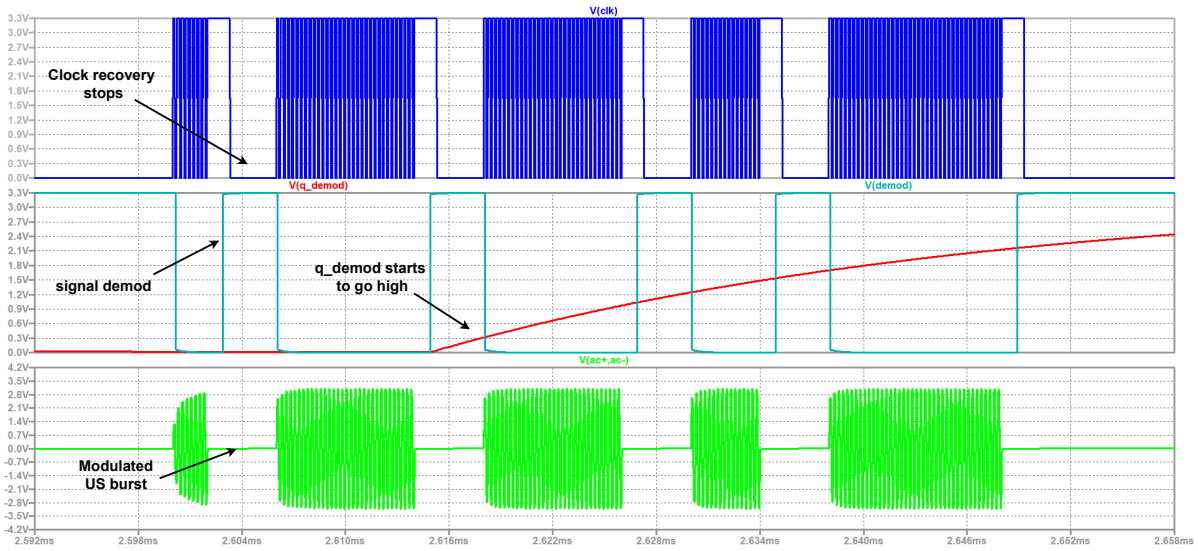

Figure 3.42: Waveform depicting the modulated US burst that carries a bit stream of '10101100' along with signal demod, q_demod and clk. The q_demod signal can be seen to go high after encountering a second rising edge in the demod signal.

Table 3.3: Truth table of DEMUX decoding the PPM modulated Forward Telemetry US burst

Counter Output				Place Value of '1'
Nr. Cycles	Q6	Q5	Q4	Bn
0 - 15	0	0	0	B0
16 - 31	0	0	1	B1
32 - 47	0	1	0	B2
48 - 63	0	1	1	B3
64 - 79	1	0	0	B4
80 - 95	1	0	1	B5
96 - 111	1	1	0	B6
112 - 127	1	1	1	B7

Go to ToC

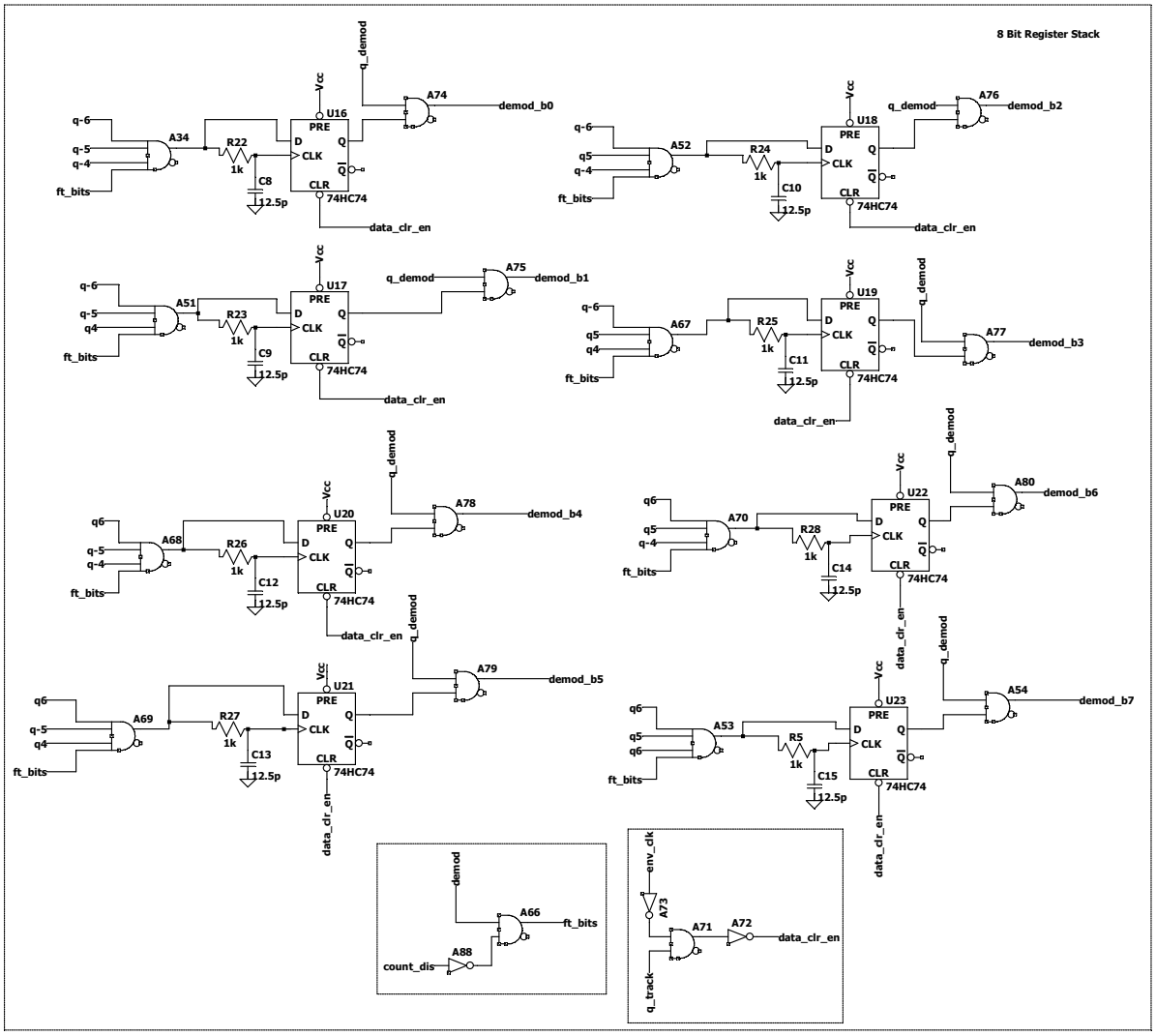

Figure 3.43: 8-bit register stack storing Forward Telemetry Data bits.

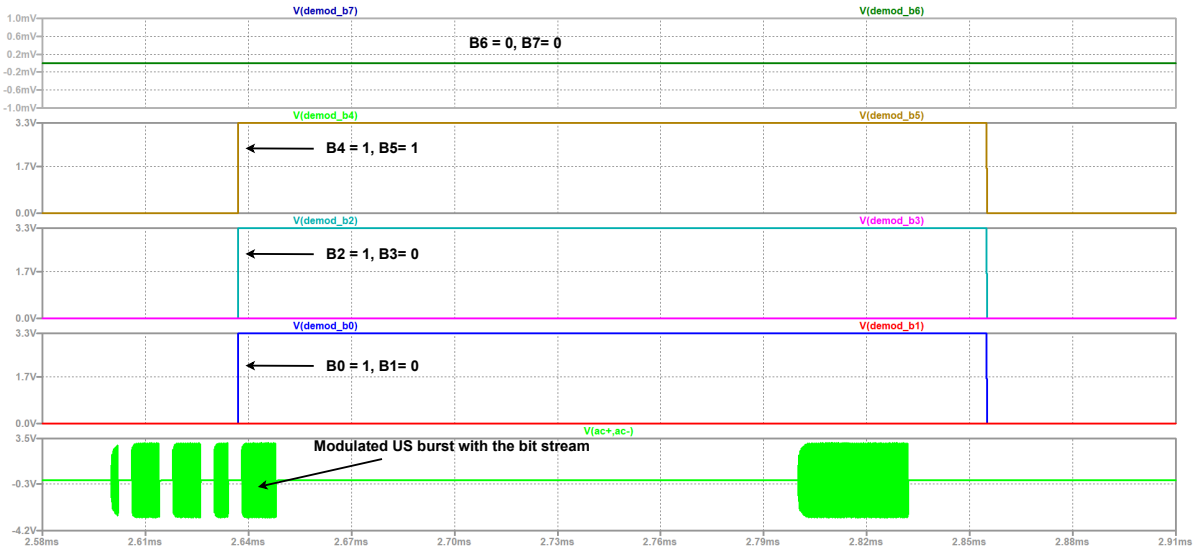

Figure 3.44: Waveform depicting the output of the 8-bit register stack and the decoded Forward Telemetry bitstream '10101100'.

Go to ToC

3.6. Experimental Results & Discussion

Figure 3.45 shows the pcb developed that implements tracking and data telemetry using CMUTs. An SMB connector connects the CMUTs to the PCB and as mentioned in the previous section, a Teensy Microcontroller is used to implement the logic represented by Table 3.1. The Microcontroller is connected to a Personal Computer (PC) and is programmed using Arduino IDE. This section presents the experimental results of data telemetry using CMUTs when a bit stream of '10001000' is transmitted from the CMUTs to the verasonics (Back Telemetry) and a bit stream of '10101100' is transmitted from verasonics to the CMUTs. The 2-D CMUT array is fixed on the rotary setup of the experimental setup (Fig 2.4). The probe is fixed on the linear stage of the setup. The CMUT array is placed about 130 mm away from the probe with a phantom in between the two identical to the setup discussed in Section 2.4. In both cases, 8 bits of data are transmitted every 4 ms of time. This implies a data rate of 2 kb/s (kilobits per second). By reducing the Pulse Repetition Time (increasing the Pulse Repetition Frequency (PRF)) to a few hundred µs and by transmitting 16 bits of data for every second burst, the data rate can be considerably increased up to an 80 kb/s. The MATLAB scripting used in the verasonics system (Sec 1.2.4) typically takes around 0.3 seconds to execute once i.e. the time taken by MATLAB processing in Figure 3.17. It was observed that when the Pulse Repetition Frequency is increased to more than 1 kHz, the Software sequencer fails to keep up with the Hardware sequencer of the Verasonics system (refer Appendix A). Therefore this data rate of 80 kb/s is not demonstrated in this work. Refer to Appendix A regarding increasing PRF.

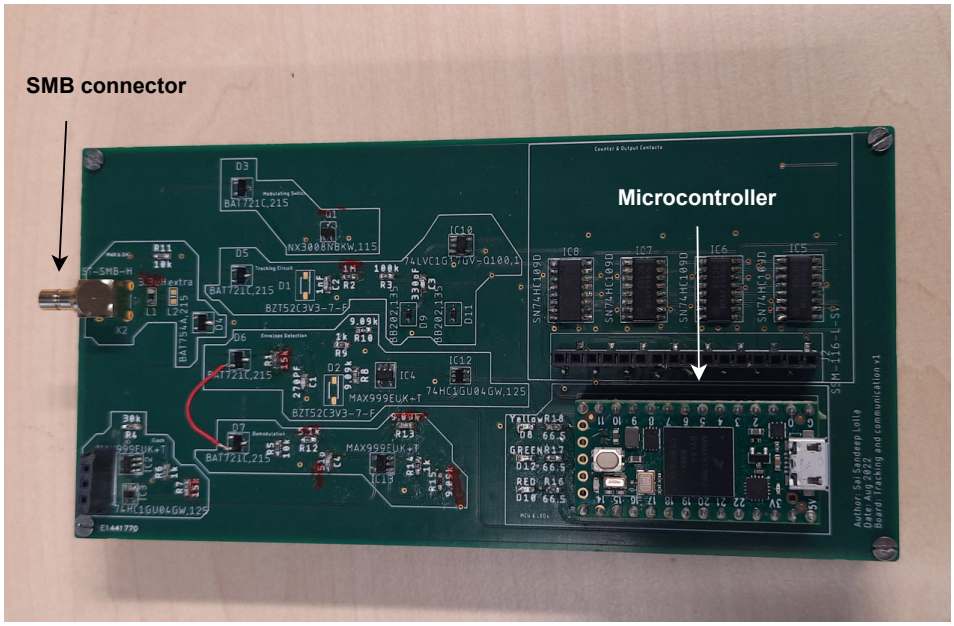

Figure 3.45: PCB developed using the circuit discussed in Section 3.3.

3.6.1. Back Telemetry Experiment

The communication protocol uses two US bursts for Back Telemetry (Sec 3.4.1). These two bursts are subtracted from each other and an envelope of this difference is extracted to decode the serially transmitted data bit stream as shown in Figure 3.17. For a bit stream of '10001000' Figure 3.20 shows a depiction of how this envelope and difference would look like.

Figure 3.46 shows the modulated waveform of the second US burst that incidents on the CMUTs and demonstrates the serial transmission of the data bits (B0, B1, ..., B7). It can be seen that the modulated waveform matches the simulated waveform (Fig 3.38) and also the conceptual waveform (Fig 3.19) when a bit stream of '10001000' is being transmitted from the CMUTs to the Verasonics. Figure 3.47 shows how this modulated waveform appears on the Verasonics (MATLAB) screen. As mentioned previously, in MATLAB, two consecutive bursts are subtracted from each other to extract the Back Telemetry Data. This graph represents the envelope of this difference that is transmitting the bit stream of '10001000'. The x-axis of the graph represents time in terms of the number of wavelengths.

Go to ToC

The US wave seen by the US probe (connected to the Verasonics) is digitized (as mentioned in Section 1.2.4). The Verasonics samples this wave with a frequency that is equal to four times the US burst. This implies this graph contains four samples for a single wavelength. The graphs contain six peaks with widths equal to 31, 36, 50, 34, 33 & 64. Therefore in terms of wavelengths, these widths are approximately equal to 8, 9, 13, 9, 8 & 16.

Recollecting the points mentioned in Section 3.4.1:

1. For the data bit pairs of '00' & '11', an envelope dip of width less than or equal to 8 cycles (or wavelengths) is present between two envelopes of width less than or equal to 8 cycles (or wavelengths).
2. For a data bit pair of '01', the envelope width will be greater than 8 wavelengths and less than 16 wavelengths.
3. For a data bit pair of '10', a dip in the envelope can be seen. The width of this dip will be greater than 8 wavelengths and less than 16 wavelengths.
4. In Back Telemetry, the starting bit is '0'.

Based on the above mentioned points, the envelope is decoded to extract the bit stream from the backscattered US burst as shown in Figure 3.47.

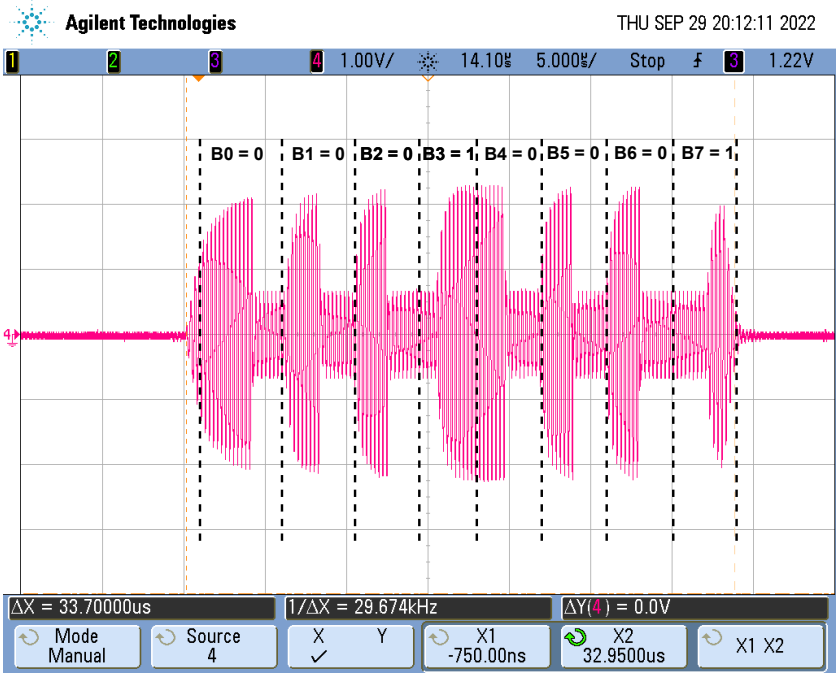

Figure 3.46: Modulated burst of Back Telemetry transmitting bit stream of '10001000'

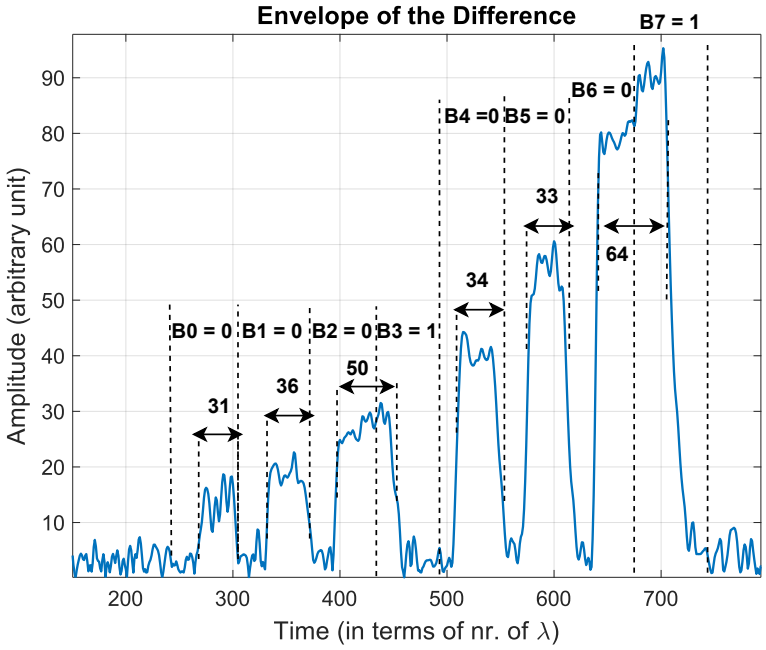

Figure 3.47: The envelope of the difference signal that is processed in MATLAB. The double-sided arrows represent the widths of the peaks.

3.6.2. Forward Telemetry Experiment

In Forward Telemetry, a PPM modulated US burst is transmitted toward the CMUTs. This modulated US burst is generated on the Verasonics using the Envelope structure discussed in Section 1.2.4. The amplitude demodulation (Sec 3.3) converts this modulated sinusoidal burst into a train of pulses representing data bit '1'. The DEMUX (Fig 3.43)/ Microcontroller (Fig 3.13) assign the bit place value for these pulses, hence decoding the bit stream transmitted in Forward Telemetry. This decoded bit stream is displayed on the Arduino IDE's Serial Monitor. Figure 3.48a shows the modulated US burst received by the CMUTs when the probe is transmitting a bit stream of '00110101'. Figure 3.48b shows the corresponding amplitude demodulated US burst which contains pulses of 3.3 V (height) representing data bit '1'. Figure 3.48c shows the screenshot of the Arduino IDE's serial monitor that is used to display the decoded Forward Telemetry bit stream. It can be seen in the figure that the transmitted bit stream '00110101' is decoded and each data bit along with its place value is displayed using the 'bit_data_ft'.

Figure 3.48a also shows a ringing of a US burst during the intermission and at the end of the burst. This ringing can be seen to be a few hundred mV in magnitude that is damped out eventually. This ringing occurs due to the resonance operation of CMUTs, performed using an external inductor as discussed in Section 3.3. This ringing is not accounted for in the simulation (Sec 3.5) or the conceptual diagrams (Fig 3.22). Since the initial cycles of the ringing have an amplitude of a few hundred mV, each such cycle will also produce a clock that is undesired. It was seen that with these additional clock cycles, the decoded bit stream contains '1' data bits with wrong place values. For example, the transmitted modulated US burst contained a bit stream of '00110101' and the decoded bit stream on the CMUTs side turned out to be '01100101'. An additional '0' bit is added before the '11' pair. This happens because the counter counts additional cycles and hence the place assignment becomes incorrect. It should be noted here that this ringing would not be a problem in the Back Telemetry because the data bits '1' and '0' in the bit stream and the number of cycles do not alter this sequence of rising and falling edges.

Since this ringing is prevalent at the start of the intermission and at the end of the US burst, a slight change in the Forward Telemetry protocol can be introduced to mitigate the ringing problem. As shown in Figure 3.22, a data bit '1' is represented by a modulated wave of 8 µs width with an intermission of 4 µs. The first 2 µs contains 8 cycles of 4 MHz sinusoidal waves and the last 2 µs contains another 8 cycles of 4 MHz sinusoidal waves. The data bit '0' is transmitted using 16 cycles of 4 MHz sinusoidal cycles. Hence in total 128 cycles of 4 MHz sinusoidal waves are transmitted toward the CMUTs. However,

the ringing causes additional cycles to appear. The 8 cycles of sinusoidal waves before and after intermission are changed to 6 cycles. The additional ringing will then compensate for the reduction in the number of cycles transmitted from the probe. By introducing this slight change, the decoding of the transmitted bitstream appeared to be successful for various bitstream combinations, hence achieving Forward Telemetry.

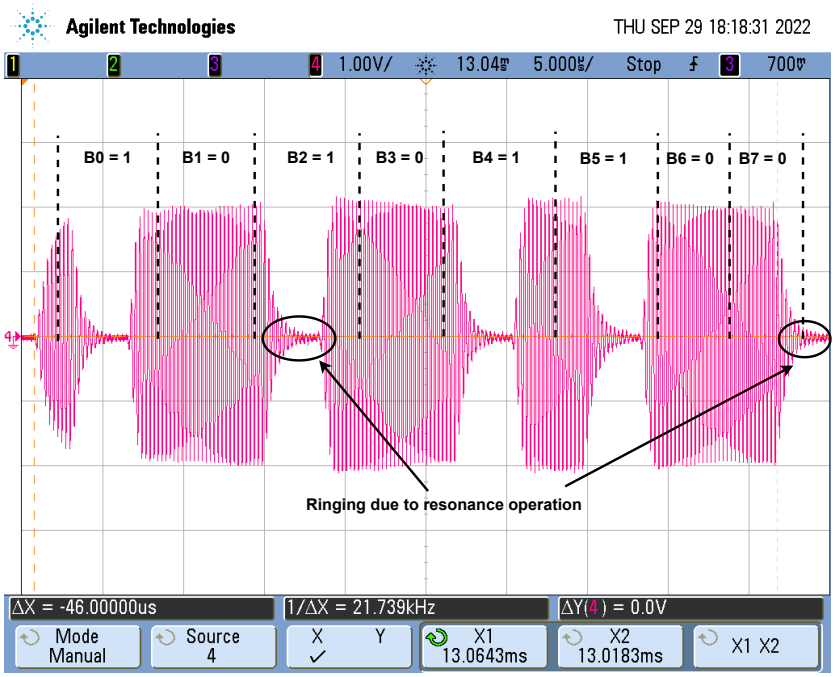

(a)

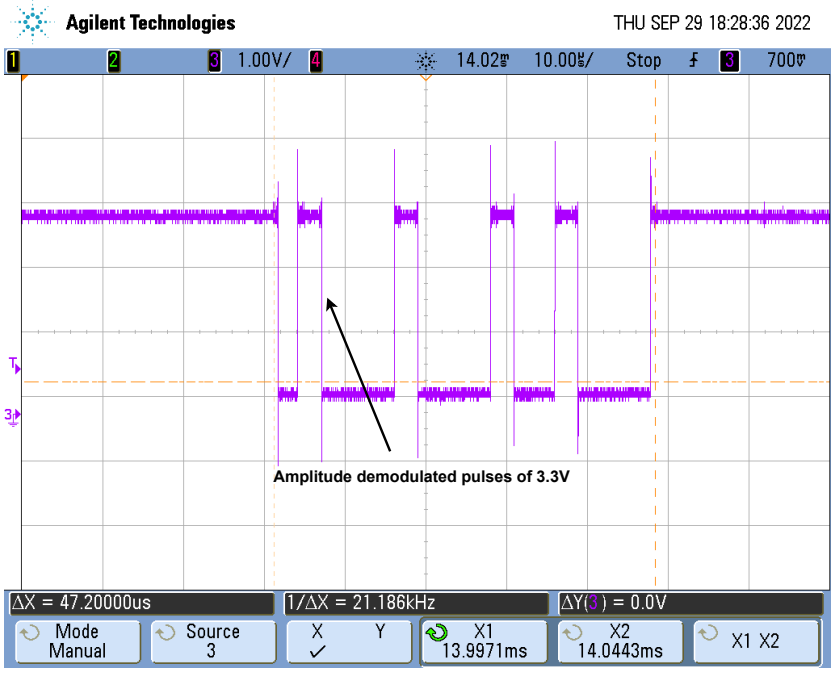

(b)

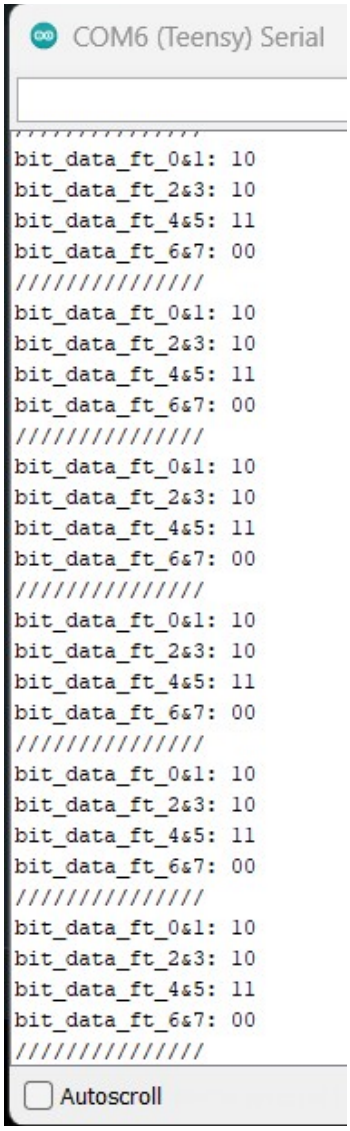

(c)

Figure 3.48: (a) US burst received by the CMUTs containing Forward Telemetry bitstream '00110101'. (b) Amplitude demodulated US burst indicating the data bit '1'. (c) Screen shot of Arduino IDE Serial Monitor displaying the received bit stream during Forward Telemetry of bitstream '00110101'.

Go to ToC

3.7. Conclusion

Ultrasound based communication needs a reliable US link between the implant's transducer and the external world. In order to perform data communication at low power using ultrasound, it is optimal to use non-coherent demodulation for Forward Telemetry and passive modulation for Back Telemetry. In order to achieve this, a communication protocol is developed in this work. The protocol performs three functions, namely: Tracking, Back Telemetry and Forward Telemetry. Performing tracking of CMUTs for every 5 words of data communication helps in maintaining the above mentioned strong US link. Back Telemetry is implemented using ASK of the backscattered US burst and Forward Telemetry is implemented using PPM of the US burst transmitted towards the CMUTs. ASK is implemented with a simple switch connected across the two terminals of the CMUTs and the PPM signal is demodulated using a typical amplitude demodulator. A data rate of 2 kb/s is achieved using this protocol when the US probe of the CMUT array is separated by a phantom of a thickness of about 130mm. By reducing the Pulse Repetition Time to a few hundred µs and by transmitting 16 bits of data for every second burst, the data rate can be considerably increased up to an 80 kb/s hence serving as one of the prospects for applications such as EEG, ECG, audio signal acquisitions, etc in bio-medical implants.

4

Conclusion

Interacting with miniaturized IMDs of a few mm^2 in size that is deeply implanted inside the human body is challenging. This interaction includes efficient power transfer and low power data communication. For US based implants efficient power transfer includes focusing of ultrasound beam on the US transducers that convert the ultrasound energy into electrical energy to power the IMD. Focusing of these ultrasound beams, therefore, requires accurate localization of these IMDs. Chapter 2 addresses this issue where a tracking algorithm based on Time Reversal beamforming is developed to locate CMUTs occupying an area of about 6.3 mm^2. The algorithm is able to track the CMUTs even when they move at a constant speed less than or equal to 1.25 mm/s. For speeds greater than 1.25 mm/s, the response time of 0.3 seconds falls short and the algorithm can be seen to in accurately locate the CMUTs. Furthermore, a 2^{nd} order curve fitting of the delay pattern measured to implement the Time Reversal method is used to reduce the errors in the measured delays. This however deprives the algorithm of its robustness against the inhomogeneous propagating medium.

Addressing the issue of low power data communication, a communication protocol is developed in this work (discussed in Chapter 3). Using this protocol data communication was established between a 2-D CMUT array (RX) and a US probe (TX) that are separated by a distance of 130 mm. A data rate of 2 kb/s was achieved using this protocol and a prospect of up to 80 kb/s also seems viable. The protocol also makes sure that the focused ultrasound link is always maintained between the TX and RX by performing tracking and data communication alternatively. The circuit implementing this protocol uses an NMOS switch for Back Telemetry and an amplitude demodulator for Forward Telemetry, hence a low power solution. However, for higher data rates, complex modulation strategies would be required that would also consume high power.

With this, the report comes to an end. This work has demonstrated the Tracking of CMUTs and Data Telemetry using Ultrasound. Building upon this work various topics can be researched or developed further in the future. These topics are further discussed in the next section.

4.1. Future Work

1. In this work, the face of 2-D CMUT array is always placed in parallel with the face of the US probe i.e. the CMUT array is oriented at 0° with respect to the probe. This is also maintained while the CMUT is moved at a constant speed. This, however, is not practically true. A two dimensional device can always change orientation in any direction when implanted inside the human body. In one of the previous works [21] the power received by the CMUT can decrease by about 50 % for a 10° change in orientation. Moreover, with this change in orientation, the backscattered US burst may not travel back to the probe, thus failing both the Time Reversal Tracking and Backscattered Data (Back) Telemetry. Therefore detection of the orientation of the CMUT array with respect to the probe is necessary. As discussed in Section 2.2.2, beamforming along with ultrasound imaging can be used to detect the orientation of the implant. The PWM protocol used in the tracking algorithm can be utilized to test this prospect. This might, however, require ultrasound transmission and acquisition electronics other than Verasonics system.

2. As discussed in Section 3.2, multi-path effects caused by bones, muscles and organs can introduce errors in data communication when using ultrasound. This multipath effect can be experimentally incorporated by introducing a reflector between the TX and RX. This can be used to evaluate how the multi-path effect comes into the picture during data communication. Building up on that a new protocol can be formulated to mitigate this effect.
3. Time Reversal Beamforming implemented in [51] involves a 2-D ultrasound transducer array instead of a linear US transducer as used in this work. When using a linear probe, the echo, the incident burst, the TX and RX needs to be present in the same plane for the linear probe to receive the backscattered echo. A 2-D probe can be used to alleviate this restriction to a certain degree. A 2-D probe can thus be used to test the angular acceptance of the out-of-plane reflected echos and hence improve the Time Reversal Algorithm to implement tracking in three dimensions (x, y and z).
4. MATLAB scripting is used for implementing the tracking algorithm. The verasonics use an in-built FPGA to drive the transmitters. The received data is however transferred to the host PC using DMA access. As mentioned in Section 2.9, the curve fitting performed on the host PC to reduce the influence of the measurement errors deprives the tracking algorithm of its robustness. This DMA transfer is one of the major error sources in the delay measurement as mentioned in Section 2.9. To avoid this DMA transfer, an external driver circuit connected to an FPGA can be used to directly drive a US transducer as the TX. The receiver circuit would receive the echo and the delays can be calculated using the FPGA. This FPGA can be programmed to implement Time Reversal beamforming hence avoiding the DMA transfer. This can hence retain the robustness of the algorithm while also increasing the response time.
5. An ASIC can be designed to implement the formulated communication protocol that also implements the tracking algorithm. This ASIC can also use variable gain stages instead of matching inductors for amplifying the harvested electrical signal from the ultrasound waves to save space as performed in [72]. This variable gain stage can also be used to recover the clock from a low amplitude signal when the CMUTs are modulated hence also avoiding power hungry blocks such as PLL.
6. The ultrasound raw data is available in the local memory of the PC. Using this same data, B-mode image reconstruction is performed in verasonics using Delay and Sum Beamforming (as discussed in Section 2.2.2). This B-mode imaging provides a live feed of the inside of the human body. The B-mode depends on the contrast provided by the amplitude of reflected echos. Something similar can also be performed by using the modulated pulse widths of the reflected echos instead of the amplitude. This can be used to produce another similar contrast image made out of the modulated widths used in the Tracking algorithm. This image would hence provide a live feed of the inside of the body while highlighting only the implant since only the implant can modulate the pulse widths.

Go to ToC

References

[1] A. B. Amar, A. B. Kouki, and H. Cao, "Power approaches for implantable medical devices," *sensors*, vol. 15, no. 11, pp. 28 889–28 914, 2015.

[2] R. Muller, M. M. Ghanbari, and A. Zhou, "Miniaturized wireless neural interfaces: A tutorial," *IEEE Solid-State Circuits Magazine*, vol. 13, no. 4, pp. 88–97, 2021.

[3] H. Dinis and P. Mendes, "A comprehensive review of powering methods used in state-of-the-art miniaturized implantable electronic devices," *Biosensors and Bioelectronics*, vol. 172, p. 112 781, 2021.

[4] A. Denisov and E. Yeatman, "Ultrasonic vs. inductive power delivery for miniature biomedical implants," in *2010 International Conference on Body Sensor Networks*, IEEE, 2010, pp. 84–89.

[5] M. Nazari, M. Sencan, *et al.*, "A novel needle-injectable millimeter scale wireless electrochemical glucose sensing platform for artificial pancreas applications," *Scientific reports*, vol. 9, no. 1, pp. 1–11, 2019.

[6] A. Khalifa, Y. Liu, Y. Karimi, *et al.*, "The microbead: A 0.009 mm 3 implantable wireless neural stimulator," *IEEE transactions on biomedical circuits and systems*, vol. 13, no. 5, pp. 971–985, 2019.

[7] R. Jegadeesan, K. Agarwal, Y.-X. Guo, S.-C. Yen, and N. V. Thakor, "Wireless power delivery to flexible subcutaneous implants using capacitive coupling," *IEEE Transactions on Microwave Theory and Techniques*, vol. 65, no. 1, pp. 280–292, 2016.

[8] R. Erfani, F. Marefat, A. M. Sodagar, and P. Mohseni, "Modeling and experimental validation of a capacitive link for wireless power transfer to biomedical implants," *IEEE Transactions on Circuits and Systems II: Express Briefs*, vol. 65, no. 7, pp. 923–927, 2017.

[9] J. S. Ho, A. J. Yeh, E. Neofytou, *et al.*, "Wireless power transfer to deep-tissue microimplants," *Proceedings of the National Academy of Sciences*, vol. 111, no. 22, pp. 7974–7979, 2014.

[10] A. Abid, J. M. O'Brien, T. Bensel, *et al.*, "Wireless power transfer to millimeter-sized gastrointestinal electronics validated in a swine model," *Scientific reports*, vol. 7, no. 1, pp. 1–6, 2017.

[11] A. Saha, S. Iqbal, M. Karmaker, S. F. Zinnat, and M. T. Ali, "A wireless optical power system for medical implants using low power near-ir laser," in *2017 39th Annual International Conference of the IEEE Engineering in Medicine and Biology Society (EMBC)*, IEEE, 2017, pp. 1978–1981.

[12] M. M. Ghanbari, D. K. Piech, K. Shen, *et al.*, "A sub-mm 3 ultrasonic free-floating implant for multi-mote neural recording," *IEEE Journal of Solid-State Circuits*, vol. 54, no. 11, pp. 3017–3030, 2019.

[13] M. Saccher, "Mems ultrasound for active implantable devices," 2019. [Online]. Available: `http://resolver.tudelft.nl/uuid:dcd6bbdb-668c-440c-ba9a-dc315e675a28`.

[14] H. Cao, V. Landge, U. Tata, *et al.*, "An implantable, batteryless, and wireless capsule with integrated impedance and ph sensors for gastroesophageal reflux monitoring," *IEEE Transactions on Biomedical Engineering*, vol. 59, no. 11, pp. 3131–3139, 2012.

[15] J. Charthad, M. J. Weber, T. C. Chang, and A. Arbabian, "A mm-sized implantable medical device (imd) with ultrasonic power transfer and a hybrid bi-directional data link," *IEEE Journal of solid-state circuits*, vol. 50, no. 8, pp. 1741–1753, 2015.

[16] M. G. Roes, J. L. Duarte, M. A. Hendrix, and E. A. Lomonova, "Acoustic energy transfer: A review," *IEEE Transactions on Industrial Electronics*, vol. 60, no. 1, pp. 242–248, 2012.

[17] D. Laqua, T. Just, and P. Husar, "Measuring the attenuation characteristics of biological tissues enabling for low power in vivo rf transmission," in *2010 Annual International Conference of the IEEE Engineering in Medicine and Biology*, IEEE, 2010, pp. 1437–1440.

[18] M. J. Weber, Y. Yoshihara, A. Sawaby, J. Charthad, T. C. Chang, and A. Arbabian, "A miniaturized single-transducer implantable pressure sensor with time-multiplexed ultrasonic data and power links," *IEEE Journal of Solid-State Circuits*, vol. 53, no. 4, pp. 1089–1101, 2018.

[19] M. Peisino, "Deeply implanted medical device based on a novel ultrasonic telemetry technology," EPFL, Tech. Rep., 2013.

[20] 2. IEEE Standards Coordinating Committee *et al.*, "Ieee standard for safety levels with respect to human exposure to radio frequency electromagnetic fields, 3khz to 300ghz," *IEEE C95. 1-1991*, 1992.

[21] Y. Westhoek, "Ultrasound energy transfer using charged cmuts," 2020. [Online]. Available: http://resolver.tudelft.nl/uuid:74a07486-73c2-4457-8261-7161acb46c60.

[22] VisualSonics, "B-mode imaging," Accessed 16-02-2022. [Online]. Available: https://www.visualsonics.com/product/software/b-mode-imaging.

[23] I. Subramaniam, "Deep implant localization and uplink data telemetry using ultrasound," 2021.

[24] Philips Engineering Solutions, "Capacitive micromachined ultrasonic transducers," Accessed 16-12-2021. [Online]. Available: https://www.engineeringsolutions.philips.com/looking-expertise/mems-micro-devices/mems-micro-devices-applications/capacitive-micromachined-ultrasonic-transducers-cmut/.

[25] O. Oralkan, B. Bayram, G. G. Yaralioglu, *et al.*, "Experimental characterization of collapse-mode cmut operation," *ieee transactions on ultrasonics, ferroelectrics, and frequency control*, vol. 53, no. 8, pp. 1513–1523, 2006.

[26] K. K. Park, O. Oralkan, and B. Khuri-Yakub, "Comparison of conventional and collapse-mode cmut in 1-d array configuration," in *2011 IEEE International Ultrasonics Symposium*, IEEE, 2011, pp. 1000–1003.

[27] G. Puzzilli, B. Govoreanu, F. Irrera, M. Rosmeulen, and J. Van Houdt, "Characterization of charge trapping in sio2/al2o3 dielectric stacks by pulsed c–v technique," *Microelectronics Reliability*, vol. 47, no. 4-5, pp. 508–512, 2007.

[28] G. Sessler, "Electric fields and forces due to charged dielectrics," *Journal of Applied Physics*, vol. 43, no. 2, pp. 405–408, 1972.

[29] M. Klemm, A. Unamuno, L. Elsä□er, and W. Jeroch, "Performance assessment of cmut arrays based on electrical impedance test results," *Journal of Microelectromechanical Systems*, vol. 24, no. 6, pp. 1848–1855, 2015.

[30] Verasonics, "Artificial intelligence for advanced ultrasound research," Accessed 28-12-2021. [Online]. Available: https://verasonics.com/artificial-intelligence-the-1-vantage-platform/.

[31] K. Kratkiewicz, R. Manwar, Y. Zhou, M. Mozaffarzadeh, and K. Avanaki, "Technical considerations in the verasonics research ultrasound platform for developing a photoacoustic imaging system," *Biomedical Optics Express*, vol. 12, no. 2, pp. 1050–1084, 2021.

[32] P. M. Lee, Z. Xiong, and J. Ho, "Methods for powering bioelectronic microdevices," *Bioelectronics in Medicine*, vol. 1, no. 3, pp. 201–217, 2018.

[33] W. K. Ward, E. P. Slobodzian, K. L. Tiekotter, and M. D. Wood, "The effect of microgeometry, implant thickness and polyurethane chemistry on the foreign body response to subcutaneous implants," *Biomaterials*, vol. 23, no. 21, pp. 4185–4192, 2002.

[34] J. L. Toennies, G. Tortora, M. Simi, P. Valdastri, and R. Webster, "Swallowable medical devices for diagnosis and surgery: The state of the art," *Proceedings of the Institution of Mechanical Engineers, Part C: Journal of Mechanical Engineering Science*, vol. 224, no. 7, pp. 1397–1414, 2010.

[35] D. A. Kuban, L. Dong, R. Cheung, E. Strom, and R. De Crevoisier, "Ultrasound-based localization," in *Seminars in radiation oncology*, Elsevier, vol. 15, 2005, pp. 180–191.

[36] I. Umay, B. Fidan, and B. Barshan, "Localization and tracking of implantable biomedical sensors," *Sensors*, vol. 17, no. 3, p. 583, 2017.

Go to ToC

[37] M.-G. Kim, Y.-S. Hong, and E.-J. Lim, “Position and orientation detection of capsule endoscopes in spiral motion,” *International Journal of Precision Engineering and Manufacturing*, vol. 11, no. 1, pp. 31–37, 2010.

[38] F. Bianchi, A. Masaracchia, E. Shojaei Barjuei, *et al.*, “Localization strategies for robotic endoscopic capsules: A review,” *Expert review of medical devices*, vol. 16, no. 5, pp. 381–403, 2019.

[39] T. D. Than, G. Alici, H. Zhou, and W. Li, “A review of localization systems for robotic endoscopic capsules,” *IEEE transactions on biomedical engineering*, vol. 59, no. 9, pp. 2387–2399, 2012.

[40] H. Mateen, R. Basar, A. U. Ahmed, and M. Y. Ahmad, “Localization of wireless capsule endoscope: A systematic review,” *IEEE Sensors Journal*, vol. 17, no. 5, pp. 1197–1206, 2017.

[41] T. C. Chang, M. L. Wang, J. Charthad, M. J. Weber, and A. Arbabian, “27.7 a 30.5 mm 3 fully packaged implantable device with duplex ultrasonic data and power links achieving 95kb/s with< 10- 4 ber at 8.5 cm depth,” in *2017 IEEE International Solid-State Circuits Conference (ISSCC)*, IEEE, 2017, pp. 460–461.

[42] H. Wymeersch, J. Lien, and M. Z. Win, “Cooperative localization in wireless networks,” *Proceedings of the IEEE*, vol. 97, no. 2, pp. 427–450, 2009.

[43] H. C. So, “Source localization: Algorithms and analysis,” *Handbook of Position Location: Theory, Practice, and Advances*, pp. 25–66, 2011.

[44] M. L. Wang, T. C. Chang, and A. Arbabian, “Ultrasonic implant localization for wireless power transfer: Active uplink and harmonic backscatter,” in *2019 IEEE International Ultrasonics Symposium (IUS)*, IEEE, 2019, pp. 818–821.

[45] Z. Nagy, M. Fluckiger, O. Ergeneman, S. Pané, M. Probst, and B. J. Nelson, “A wireless acoustic emitter for passive localization in liquids,” in *2009 IEEE International Conference on Robotics and Automation*, IEEE, 2009, pp. 2593–2598.

[46] M. Fluckiger and B. J. Nelson, “Ultrasound emitter localization in heterogeneous media,” in *2007 29th Annual International Conference of the IEEE Engineering in Medicine and Biology Society*, IEEE, 2007, pp. 2867–2870.

[47] R. S. Bandaru, A. Sørnes, J. D’hooge, and E. Samset, “2d localization of specular reflections using ultrasound,” in *2014 IEEE International Ultrasonics Symposium*, IEEE, 2014, pp. 2209–2212.

[48] K. Arshak and F. Adepoju, “Capsule tracking in the gi tract: A novel microcontroller based solution,” in *Proceedings of the 2006 IEEE Sensors Applications Symposium, 2006.*, IEEE, 2006, pp. 186–191.

[49] J. D. Gumprecht, T. C. Lueth, and M. B. Khamesee, “Navigation of a robotic capsule endoscope with a novel ultrasound tracking system,” *Microsystem technologies*, vol. 19, no. 9, pp. 1415–1423, 2013.

[50] B. C. Benedict, M. M. Ghanbari, and R. Muller, “Phased array beamforming methods for powering biomedical ultrasonic implants,” *arXiv preprint arXiv:2203.01493*, 2022.

[51] B. C. Benedict, M. M. Ghanbari, S. F. Alarnouti, N. T. Ersumo, and R. Muller, “Time reversal beamforming for powering ultrasonic implants,” in *2021 10th International IEEE/EMBS Conference on Neural Engineering (NER)*, IEEE, 2021, pp. 647–650.

[52] W. Kees, S. Evert, and F. Jacob, “What is acoustic reciprocity?,” 2019. [Online]. Available: `http://homepage.tudelft.nl/t4n4v/Reciprocity2/index2.htm`.

[53] J. Grythe, “Beamforming algorithms - beamformers,” *Norsonic TECHNICAL NOTE*, pp. 1–5, 2015. [Online]. Available: `https://web2.norsonic.com/wp-content/uploads/2016/10/TN-beamformers.pdf`.

[54] V. Perrot, M. Polichetti, F. Varray, and D. Garcia, “So you think you can das? a viewpoint on delay-and-sum beamforming,” *Ultrasonics*, vol. 111, p. 106 309, 2021.

[55] K. P. E. Mercado, *Developing high-frequency quantitative ultrasound techniques to characterize three-dimensional engineered tissues*. University of Rochester, 2015.

[56] *Tdbf - delay-and-sum beamforming in the time domain*. [Online]. Available: https://www.gfaitech.com/knowledge/faq/delay-and-sum-beamforming-in-the-time-domain.

[57] O. T. Von Ramm and S. W. Smith, "Beam steering with linear arrays," *IEEE transactions on biomedical engineering*, no. 8, pp. 438–452, 1983.

[58] S. Kawasaki, Y. Westhoek, I. Subramaniam, M. Saccher, and R. Dekker, "Pre-charged collapse-mode capacitive micromachined ultrasonic transducer (cmut) for broadband ultrasound power transfer," in *2021 IEEE Wireless Power Transfer Conference (WPTC)*, IEEE, 2021, pp. 1–4.

[59] G. Shafiq and K. C. Veluvolu, "Surface chest motion decomposition for cardiovascular monitoring," *Scientific reports*, vol. 4, no. 1, pp. 1–9, 2014.

[60] G. Ramachandran and M. Singh, "Three-dimensional reconstruction of cardiac displacement patterns on the chest wall during the p, qrs and t-segments of the ecg by laser speckle inteferometry," *Medical and Biological Engineering and Computing*, vol. 27, no. 5, pp. 525–530, 1989.

[61] MathWorks, "Find delay between correlated signals," Accessed 11-01-2022. [Online]. Available: https://uk.mathworks.com/help/signal/ug/find-delay-between-correlated-signals.html.

[62] M. Saccher, S. S. Lolla, S. Kawasaki, and R. Dekker, "Video recording associated with the publication: Time-efficient low power time/phase-reversal beamforming for the tracking of ultrasound implantable devices," in *4TU.ResearchData, 13-Sep-2022 [Online]*. [Online]. Available: https://data.4tu.nl/articles/dataset/Video_recording_associated_with_the_publication_Time-efficient_low_power_time_phase-reversal_beamforming_for_the_tracking_of_ultrasound_implantable_devices/21081937/1.

[63] T. Bos, W. Jiang, J. D'hooge, M. Verhelst, and W. Dehaene, "Enabling ultrasound in-body communication: Fir channel models and qam experiments," *IEEE transactions on biomedical circuits and systems*, vol. 13, no. 1, pp. 135–144, 2018.

[64] G. E. Santagati and T. Melodia, "Experimental evaluation of impulsive ultrasonic intra-body communications for implantable biomedical devices," *IEEE Transactions on Mobile Computing*, vol. 16, no. 2, pp. 367–380, 2016.

[65] M. Meng and M. Kiani, "Gastric seed: Toward distributed ultrasonically interrogated millimeter-sized implants for large-scale gastric electrical-wave recording," *IEEE Transactions on Circuits and Systems II: Express Briefs*, vol. 66, no. 5, pp. 783–787, 2019.

[66] G. P. Thomas and B. C. Jobst, "Critical review of the responsive neurostimulator system for epilepsy," *Medical Devices (Auckland, NZ)*, vol. 8, p. 405, 2015.

[67] J.-Y. Tsai, K.-H. Huang, J.-R. Wang, S.-I. Liu, and P.-C. Li, "Ultrasonic wireless power and data communication for neural stimulation," in *2011 IEEE International Ultrasonics Symposium*, IEEE, 2011, pp. 1052–1055.

[68] B. Jaafar, J. A. Neasham, and P. Degenaar, "What is ultrasound can and cannot do in the communication of biomedical implanted medical devices," *IEEE Reviews in Biomedical Engineering*, 2021.

[69] A. Carovac, F. Smajlovic, and D. Junuzovic, "Application of ultrasound in medicine," *Acta Informatica Medica*, vol. 19, no. 3, p. 168, 2011.

[70] M. A. Hannan, S. M. Abbas, S. A. Samad, and A. Hussain, "Modulation techniques for biomedical implanted devices and their challenges," *Sensors*, vol. 12, no. 1, pp. 297–319, 2011.

[71] U. Bihr, T. Liu, and M. Ortmanns, "Telemetry for implantable medical devices: Part 3-data telemetry," *IEEE Solid-State Circuits Magazine*, vol. 6, no. 4, pp. 56–62, 2014.

[72] F. Mazzilli and C. Dehollain, "184 μw ultrasonic on–off keying/amplitude-shift keying demodulator for downlink communication in deep implanted medical devices," *Electronics Letters*, vol. 52, no. 7, pp. 502–504, 2016.

[73] R. Moghimi, *Curing comparator instability with hysteresis | analog devices*, 2000. [Online]. Available: https://www.analog.com/en/analog-dialogue/articles/curing-comparator-instability-with-hysteresis.html.

[74] J. Guedey, Y. Deval, H. Lapuyade, and F. Rivet, “Binary phase-shift keying for ultrasonic intrabody area networks,” in *2020 IEEE MTT-S International Microwave Biomedical Conference (IMBioC)*, IEEE, 2020, pp. 1–3.

[75] G. E. Santagati, T. Melodia, L. Galluccio, and S. Palazzo, “Medium access control and rate adaptation for ultrasonic intrabody sensor networks,” *IEEE/ACM Transactions on Networking*, vol. 23, no. 4, pp. 1121–1134, 2014.

[76] D. T. Blackstock, *Fundamentals of physical acoustics*, 2001.

[77] R. Cavallari, F. Martelli, R. Rosini, C. Buratti, and R. Verdone, “A survey on wireless body area networks: Technologies and design challenges,” *IEEE Communications Surveys & Tutorials*, vol. 16, no. 3, pp. 1635–1657, 2014.

[78] I. Subramaniam, “Deep implant localization and uplink data telemetry using ultrasound,”

[79] *Teensy® 4.0*. [Online]. Available: `https://www.pjrc.com/store/teensy40.html`.

[80] *Manchester data encoding for radio communications*. [Online]. Available: `https://www.maximintegrated.com/en/design/technical-documents/app-notes/3/3435.html`.

[81] *Low-voltage variable capacitance diode*, BB202, Rev. 02, NXP, 2008. [Online]. Available: `https://www.nxp.com/docs/en/data-sheet/BB202_N.pdf`.

A

Error in Delay Measurement

As mentioned in Section 1.2.4, the US raw data received by the US probe is first stored in the local buffer of the acquisition modules of the vantage unit and then transferred to the local memory of the host PC by Direct Memory Access (DMA). This sequence of events is performed by the Hardware (HW) Sequencer (Fig 1.7). The envelope detection, curve fitting and other processing of US data on MATLAB are performed by the Software (SW) Sequencer. To maintain a constant Pulse Repetition Frequency (PRF), the Hardware Sequencer is programmed to run to transmit and receive the US bursts at a particular frequency. Additionally, the HW sequencer also replaces the US raw data from the local memory of the host PC as soon as a new acquisition is performed. Since the Pulse Repetition Time is in the order of one or two milliseconds, the HW sequencer performs the transmit, receive and DMA transfer much faster than the processing of the software sequencer that performs which previously was seen to have a response time of 0.3 seconds combined for command and function echo processing (Sec 2.9).

Revisiting the software processing in MATLAB (Fig 3.16 & Fig 3.17), the verasonics script computes the difference between the command echo and function echo and the envelope of this difference for all the 128 channels of the US probe. This computation is performed on the US data present in the local memory of the host PC. Cross-correlation is now used to find the delays for these 128 envelopes. Figure A.1 shows these 128 delays and the 2^{nd} order curve fit used to reduce the influence of the measurement errors in the delay measurements (Sec 2.8). The x-axis shows the channel number of the US probe and the y-axis shows the measured delay for the corresponding channels in terms of the number of wavelengths. Three channels: 1,4 and 5 are highlighted in the figure. Channel 1 is delayed by zero wavelengths since this channel is used to measure the delays of the rest of the channels using cross-correlation. Channel 4 can be seen to exhibit a delay equal to a quarter of a wavelength. However, channel 5 can be seen to exhibit a delay equal to ten times of the wavelength. The individual PZT elements on the probe are separated by 283 µm and the wavelength of a US wave is about 363 µm. For a delay that is equal to ten times this wavelength, the probe elements must be separated by about 3000 µ, hence making it physically impossible to have a delay equal to ten times the wavelength. Furthermore, the delay of 10 (λs) is set at the upper limit of delay computation in the verasonics script.

Figure A.2 shows the difference signal and the envelope signal of channels 1, 4, and 5. In the figure, it can be seen that the channel envelope signal of channels 1 and 4 have a slight delay between them and the envelope signal of channel 5 is negligible. Since the channel 5 envelope signal is negligible, the delay pertaining to the channel is computed to be 10 (λs). This negligible difference can only occur if the command echo and the function echo received by the probe are practically identical [1]. This happens due to the fast transmit, receive, and DMA transfer performed by the HW sequencer. The following set of events describes how this fast acting HW sequencer can cause this error in the delay measurement. The HW sequencer acquires command echo data and transfers it to the PC local memory pertaining to location (x_1,y_1) in the ROI -> SW sequencer processing this data -> HW sequencer acquires the

[1] On the contrary, since the function echo seen by channels 1 and 5 have a modulation due to the PWM protocol, a difference signal and hence an envelope can be seen.

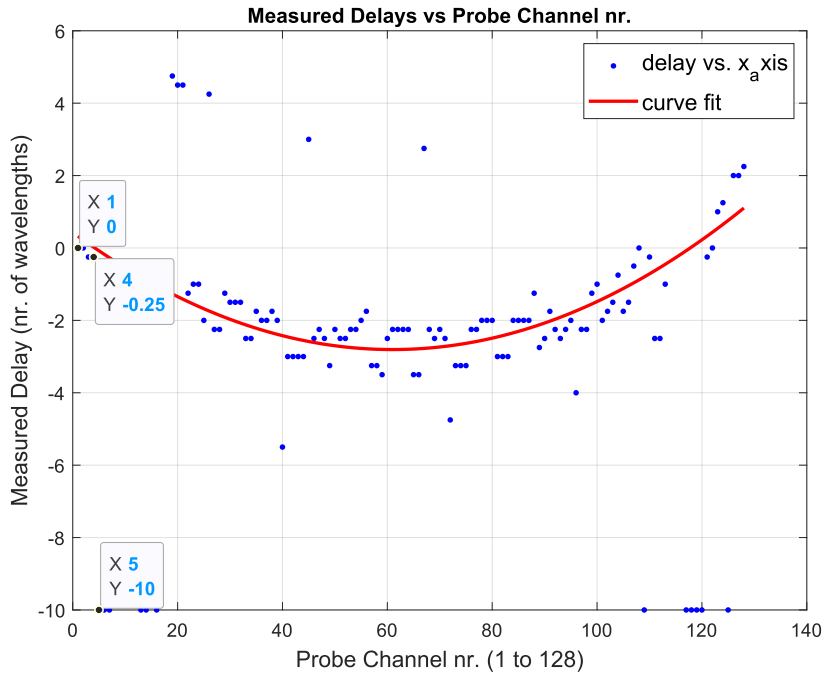

Figure A.1: Measured delays and 2nd order curve fit highlighting channels: 1,4 and 5.

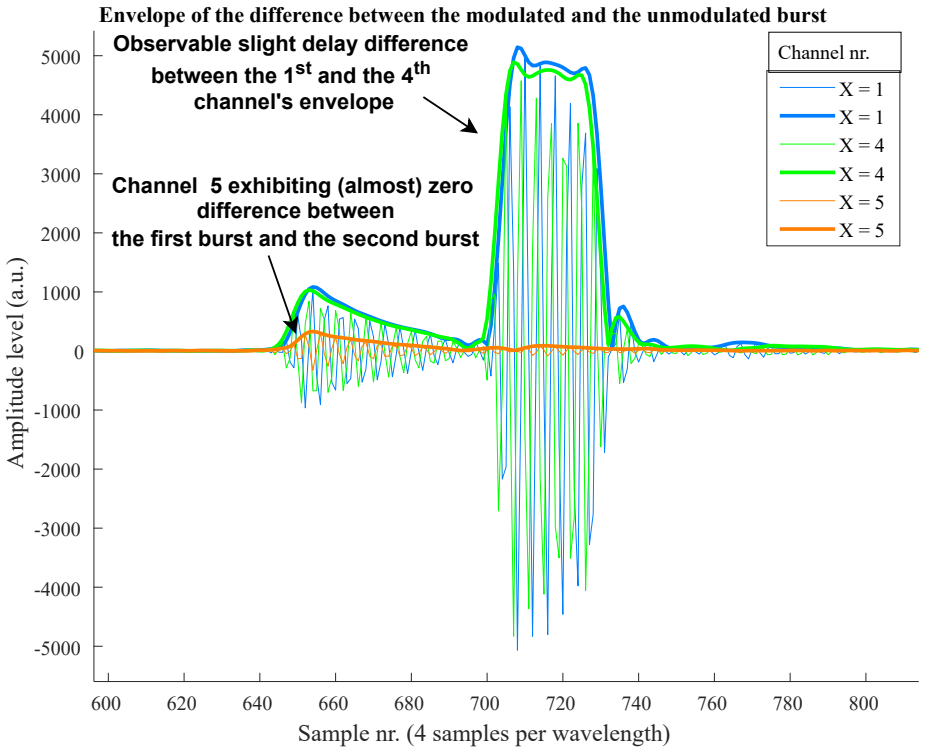

Figure A.2: Difference and envelope signals of channels: 1,4 and 5.

function echo data -> SW sequencer is still processing the previous data for the command echo -> HW sequencer acquires command echo data from location (x_2,y_2) -> SW sequencer finishes the processing of command echo from location (x_1,y_1) and starts processing for its corresponding function echo. Since

the data in the local memory of the PC belongs to the command echo from the next location, it does not contain any modulation which results in the negligible difference signal mentioned above.

In order to avoid this problem, sufficient time must be given for the SW sequencer to complete all the computations in the script. A PRF of 500 kHz is used in this work which is seen to provide sufficient time for the SW sequencer and avoid the errors caused by the fast acting HW sequencer.

B

PCB Layout and Schematic

Figures B.1 shows the schematic diagram of the circuit designed in this work. Figure B.2 shows the PCB layout of the circuit designed in this work. Figure

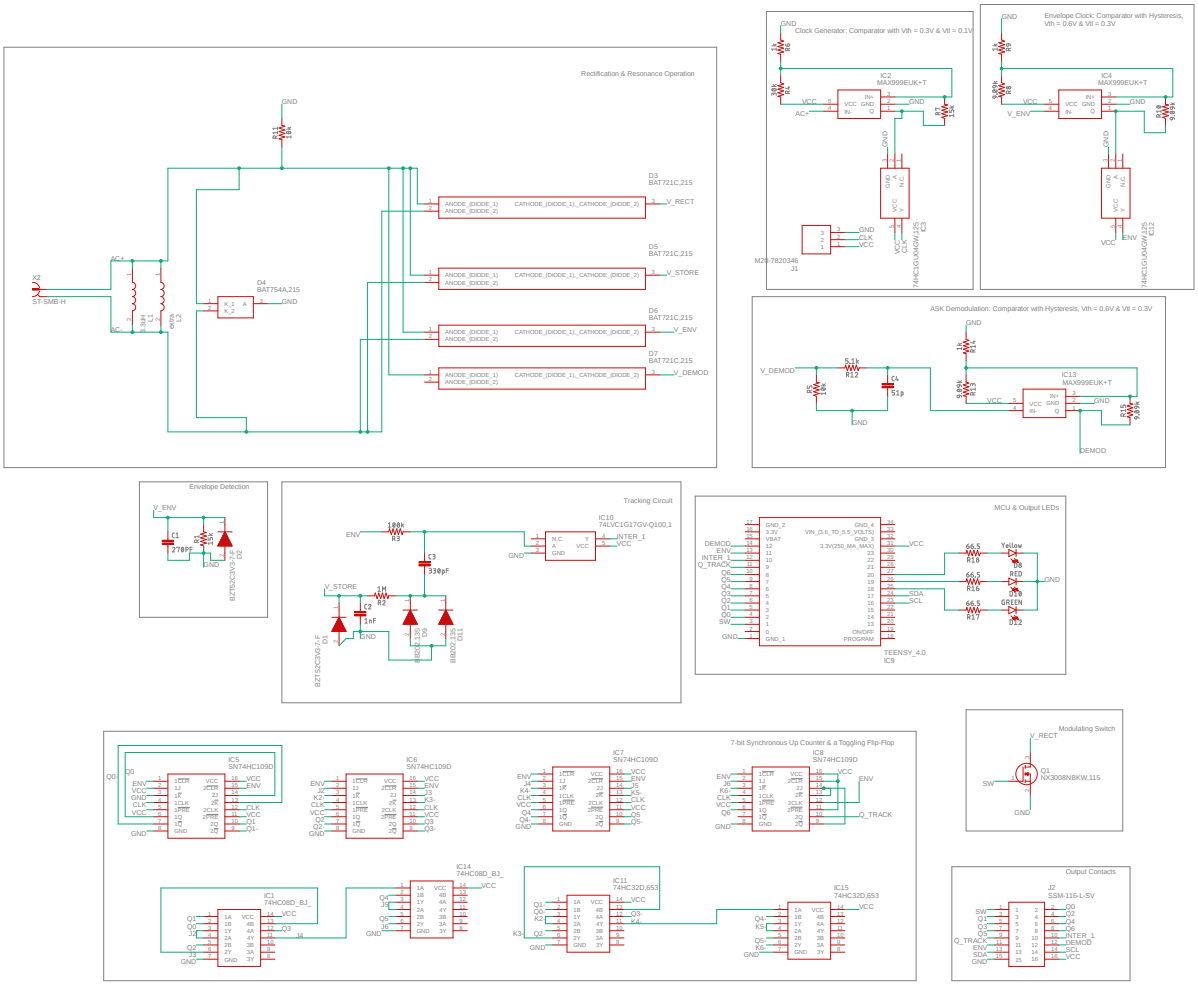

Figure B.1: Schematic diagram of the circuit designed in this work.

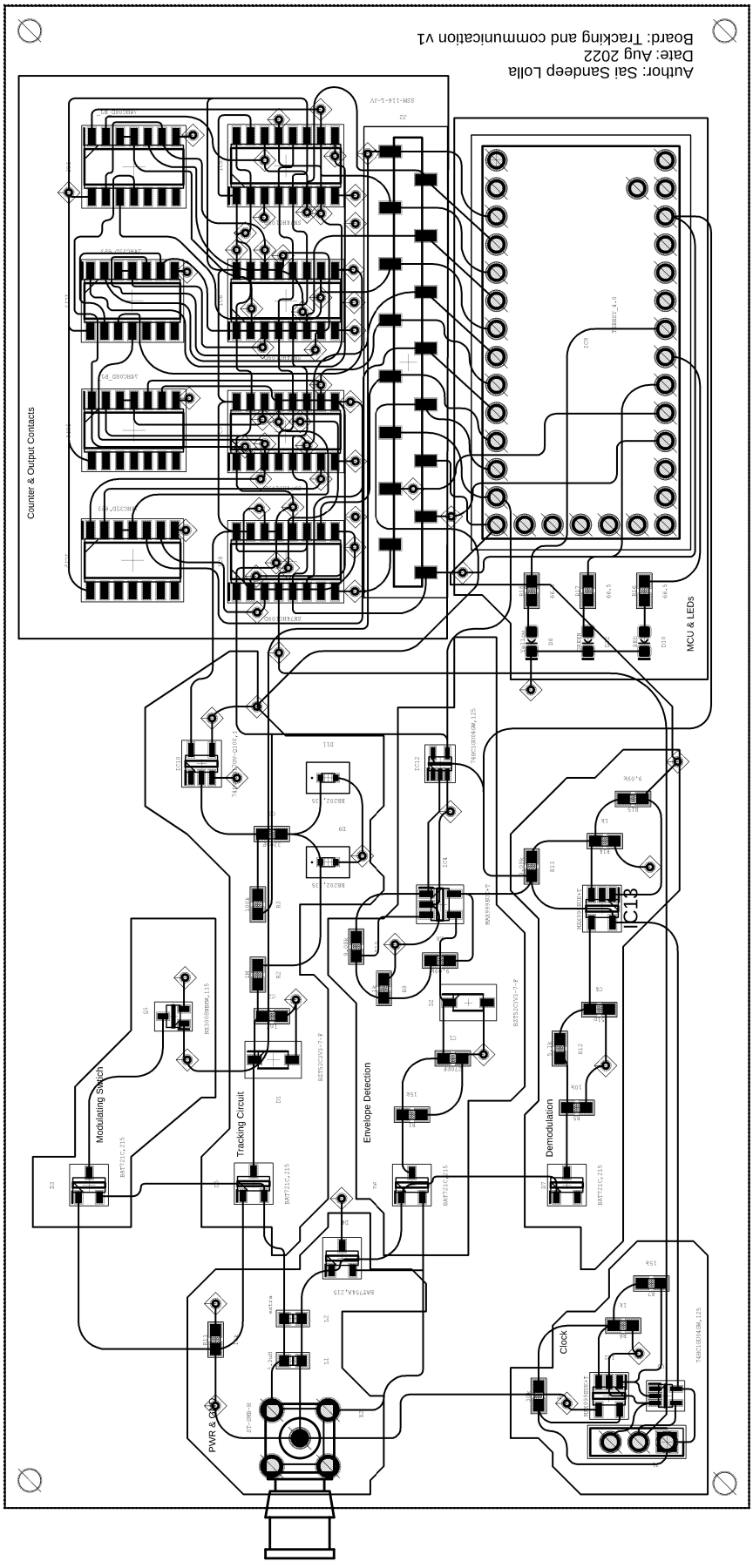

Figure B.2: PCB Layout of the circuit designed in this work.

Go to ToC